Preparation of nanocrystals and nanocomposites of nanocrystal–conjugated polymer, and their photophysical properties in confined geometries

By

Jun Xu

A dissertation submitted to the graduate faculty

in partial fulfillment of the requirements for the degree of

DOCTOR OF PHILOSOPHY

Major: Materials Science and Engineering

Program of Study Committee:
Zhiqun Lin, Major Professor
Michael Kessler
Mufit Akinc
Balaji Narasimhan
Klaus Schmidt-Rohr

Iowa State University

Ames, Iowa

2007

UMI Number: 3289370

UMI®

DEDICATIONS

I would like to dedicate this work to my wife, Guoqin Yu, and my parents.

TABLE OF CONTENTS

LIST OF FIGURES

ABSTRACT

Semiconductors nanocrystals (NCs), also called quantum dots (QDs), have attracted tremendous interest over the past decade in the fields of physics, chemistry, and engineering. Due to the quantum-confined nature of QDs, the variation of particle size provides continuous and predictable changes in fluorescence emission. On the other hand, conjugated polymers (CPs) have been extensively studied for two decades due to their semiconductor-like optical and electronic properties. The electron and energy transfer between NCs and CPs occur in solar cells and light emitting diodes (LEDs), respectively. Placing CPs in direct contact with a NC (i.e., preparing NC-CP nanocomposites) carries advantage over cases where NC aggregation dominates. Such NC-CP nanocomposites possess a well-defined interface that significantly promotes the charge or energy transfer between these two components. However, very few studies have centered on such direct integration.

We prepared NCs and NC−CP nanocomposites based on heck coupling and investigated the energy and charge transfer between semiconductor NCs (i.e., CdSe QDs), CPs (i.e., poly(3-hexyl thiophene) (P3HT)) in the nanocomposites in confined geometries. Two novel strategies were used to confine NC and/or NC−CP nanocomposites: (a) directly immobilizing nanohybrids, QDs and nanorods in nanoscopic porous alumina membrane (PAM) , and (b) confining the QDs and CPs in sphere-on-flat geometry to induce self-assembly.

While investigating the confinement effect, gradient concentric ring patterns of high regularity form spontaneously simply by allowing a droplet of solution containing either conjugated polymer or semiconductor nanocrystal in a consecutive stick-slip mothion in a confined geometry. Such constrained evaporation can be utilized as a simple, cheap, and robust strategy for self-assembling various materials with easily tailored optical and electronic properties into spatially ordered, two-dimensional patterns. These self-organized patterns of functional nanoscale materials over large areas offer a tremendous potential for

applications in optoelectronic devices, LEDs, solar cells, and biosensors. Meanwhile, spherical nanocrystals (i.e. CdSe/ZnS core/shell QDs) were placed in a hexagonal array of highly ordered cylindrical nanopores of PAMs by a simple dip-coating method and vacuum suction process, respectively. The fluorescence of CdSe/ZnS QD was retained after being filled inside PAMs and the filling contents were obtained via transmission UV-vis measurements.

CHAPTER 1. GENERAL INTRODUCTION

Organization of thesis format

This dissertation is the combination of journal articles which have been published or submitted. Chapter 1 is general introduction for the thesis. Chapter 2 is an article published in Physical Review Letters. The title is "Self-assembly of gradient concentric rings via solvent evaporation from a capillary bridge". Chapter 3 is an article published in Angwandte Chemie International Edition. The title is "Evaporation-induced self-assembly of nanoparticles from a sphere-on-flat geometry". Chapter 4 is an article published in Applied Physics Letters. The title is "Quantum dots confined in nanoporous alumina membranes". Chapter is an article published in Journal of the American Chemical Society. The title is "Organic-inorganic nanocomposites via directly grafting connjugated polymers onto quantum dots". Chapter 6 is the general conclusions for the dissertation.

Nanocrystals and conjugated polymers

Nanocrystals

Semiconductors nanocrystals (NCs) prepared as colloids in the 1-10 nm size range have generated tremendous interest over the past decade in the fields of physics, chemistry, and engineering.[1] These NCs are also called quantum dots (QDs); their optical properties can be predicted by quantum mechanics. The good photostability, high photoluminescence (PL) efficiency, and wide emission tunability make QDs excellent choice as novel chromophores. In comparison with organic dyes, this class of luminescent labels have high quantum yield, high molar extinction coefficients (~10–100 times that of organic dyes)[2, 3] and narrow, symmetric PL bands (full-width at half-maximum ~25–40 nm), spanning the UV to near-infrared range and resistance to photobleaching.[4] They provide a functional platform for a class of materials for use in light emitting diodes (LEDs),[5] photovoltaic cells,[6] and bio-

sensors.[7] Due to the quantum-confined nature of QDs such as cadmium selenide (CdSe), the variation of particle size provides continuous and predictable changes in fluorescence emission. Significant number of NCs have been synthesized, including II-VI group NCs such as CdSe and CdTe, III-V group NCs such as InP and InAs, and IV-VI group NCs such as PbSe and PbS.[8] By selecting the appropriate NC composition and fine-tuning their sizes, it is possible to obtain emission spanning wavelength from UV to far-infrared.[2]

The most intrinsic property of NCs that attracts research efforts is their size dependent emission upon illumination due to quantum confinement effect, which occurs when one or more of the dimensions of a NC approach the size of an exciton in bulk crystal, called the Bohr exciton radius, leading to energy levels called "energy subbands", i.e., the carriers can only have discrete energy values (see Figure 1-1).[8] The band gap of a specific NC, E_g^{NC}, can be mathematically described as below:

$$E_g^{NC} = E_g^{B} + (h^2\pi^2 / 2R^2)(1/m_e^* + 1/m_h^*) - 1.8e^2 / \varepsilon R \tag{1-1}$$

where E_g^{B} is the band gap of bulk materials, R is the radius of the NC, m_e^* is the reduced mass of the electron, m_e^* is the reduced mass of the hole, and ε is the dielectric constant of the bulk form of the NC. Based on eq. (1), it is clear that smaller NC diameter leads to bigger band gap, which in turn translates into shorter wavelength emission.
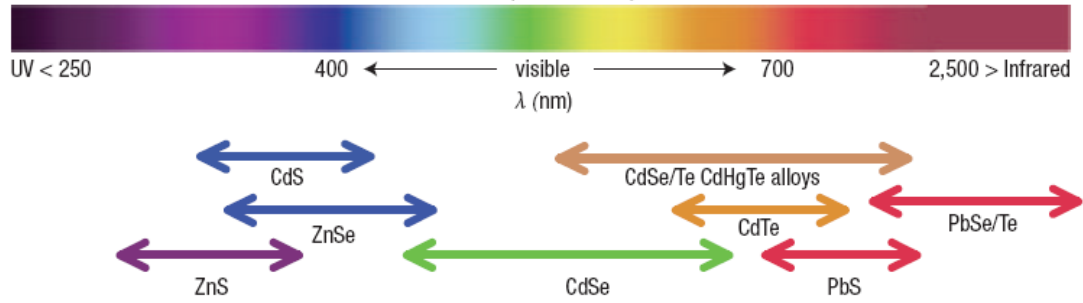
Figure 1-1. Representative semiconductor NCs emission over the spectrum. [2]

The breakthrough on the synthesis of high quality NCs was accomplished by Bawendi in 1993 with the introduction of a phosphine oxide surfactant as both the capping ligand and the reaction medium at high temperature.[9] These NCs are of high quantum yield and resistant to photo bleaching. They have broad absorption, while their emission peaks are sharp and symmetric. In the following years, Bawendi, Alivisatos, and Peng systematically investigated the growth mechanism of II-VI semiconductor NCs, by exploring different kinds of precursors, ligands, and their mixing ratios.[10-12] The temporal growth of the NCs was studied as well. These works eventually led to the successful controlled-growth of both 1D and 3D nanocrystals (nano rod and tetrapod, respectively).[13] The shape control was achieved by adjusting the amount of strongly coordinating capping ligand, such as hexylphosphonic acid (HPA), to promote the preferential growth along one direction of the wurtzite structure CdSe nanocrystal.[14-17] Multiple injections of the precursor solution were needed to maintain high monomer concentration, thereby facilitating the growth of long wires.[14] Recently, CdSe nanowires have been synthesized by microwave instead of at high temperature.[18] One interesting method for growing nanowires is to self-assemble spherical nanoparticles into nanowires. Water soluble CdTe nanoparticles can self-assemble and grow into nanowires when the surface passivating ligands are partially removed and the nanoparticles concentration is relatively high.[19]

Study on the charge transfer behaviors of NCs (i.e., quantum dots (QDs)), is of great importance for improving the device performance of LEDs and solar cells utilizing QDs. The charge transfer behavior of QDs supperlattice produced by molecular beam epitaxy was reported in 1998.[20] However, semiconductor NCs are more obvious choices for the QD conductance investigation. Many publications have been concentrated on the experimental measurements of conductance of individual QDs[21-26] and QD films.[27-32] The assemblies of QDs in polymeric electrolytes were also studied to provide insight into the charge transfer behavior of QDs in organic solar cells.[33-36] A large amount of theoretical calculations were

performed simultaneously.[37, 38] From 2003 to 2005, several review articles were published discussing the electron conducting behavior of quantum dots both theoretically and mathematically.[39-41]

The electron transfer in semiconductor nanowires has been studied mostly by Leiber (CdS nanowires)[42, 43], Kotov (CdTe nanowires)[44], and Yang (ZnO nanowires)[45]. A rectifying I-V curve was observed on a core-shell nanowire and a LED device was made accordingly.[46] Recently, the electron and hole mobility-lifetime were quantitatively measured by Lauhon et al by using scanning photocurrent microscopy with ohmic contacts.[47]

By passivating the NC surface (e.g.,CdSe) with higher band gap materials, such as zinc sulfide (ZnS), the resulting CdSe/ZnS core/shell NCs possess a strong photoluminescence,[48] which is particularly important for use in biological applications[49, 50]. The surface quenching of excitons in the emissive CdSe core is prevented by passivating most of the vacancies and trap sites on the CdSe surface, thereby increasing the quantum yield and photostability of NCs.

Conjugated polymers

Due to their semiconductor-like optical and electronic properties, conjugated polymers (CPs) have been extensively researched for two decades. They offer the possibility for use in photovoltaic cells,[51-54] light emitting diodes (LED),[55, 56] thin-film field effect transistors (FET),[57-59] and bio-sensors.[60, 61] For example, polyanilines have been used for electromagnetic shielding of electronic circuits;[62] poly(phenylene vinylene) was fabricated into LEDs for electroluminescent displays;[63] poly(thiophene) has been intensively explored as a material for FET and a key component in organic solar cells;[64] and poly(pyrrole) has even been investigated as a microwave absorbing coating to be used on stealth aircrafts.[65] The optoelectronic properties of CPs depend heavily on the physical conformation of the polymer chains.[66, 67] The main chain of a CP is made up with alternating double bonds and single bonds (see Figure 1-2). The first kind of CP, polyacetylene, was made by Shirakawa

and his co-workers in 1974.[68] Unlike most other polymers, polyacetylene was found to be a semiconductor; the conductivity increases dramatically upon oxidative or reductive "doping".[69] The breakthrough in the field of CP did not come till 1990 when the electroluminescent properties of a CP, poly(para-phenylene vinylene) were discovered.[70] This discovery opened up the field of organic electronics.
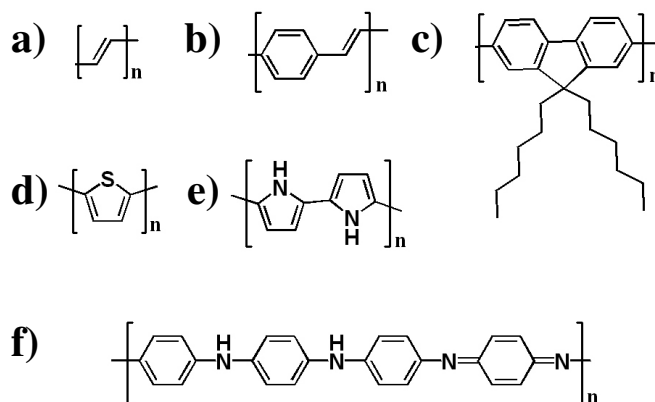
Figure 1-2. Structures of conjugated polymers. (a) polyacetylene, (b) poly(*p*-phenylene vinylene), (c) polyfluorene, (d) polythiophene, (e) polypyrrole, and (f) polyaniline.

The conductivity mechanism of CP is different from the "free electrons" mechanism of metallic materials. The electrical conductivity of CP is dependant on both the intra-chain charge diffusion and inter-chain charge hopping.[71] Therefore, the conductivities of amorphous CPs are relatively low due to the lack of inter-chain hopping.[72] For example, the amporphous poly(3-alkylthiophene) (PATs) has a hole mobility in the range of 10^{-5} cm^2 V^{-1} S^{-1}.[73] It increases to 0.2 cm^2 V^{-1} S^{-1}, a four orders of magnitude increment, when the PAT film is turned into semi-crystalline upon annealing.[74] A significant conductivity improvement can be achieved by "doping", either oxidatively (p-doping)[68] or reductively (n-doping)[75] as shown below

$$\left[\!\!\!\begin{array}{c}\diagup\diagup\end{array}\!\!\!\right]_{n} + \text{3x/2 I}_2 \longrightarrow \left[\!\!\!\begin{array}{c}\diagup\diagup\end{array}\!\!\!\right]_{n}^{\text{x}^+} + \text{x I}_3^- \qquad \text{Oxidative \; doping}$$

$$\left[\!\!\!\begin{array}{c}\diagup\diagup\end{array}\!\!\!\right]_{n} + \text{x Na} \longrightarrow \left[\!\!\!\begin{array}{c}\diagup\diagup\end{array}\!\!\!\right]_{n}^{\text{x}^-} + \text{x Na}^+ \qquad \text{Reductive \; doping}$$
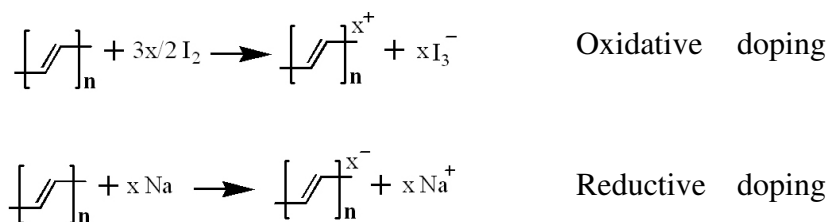
In the case of oxidative doping, a positive charge was injected on to the CP chain, which can hop between the delocalized energy bands. Reductive doping is much rarer due to the fact that the oxygen in the air will readily oxidize the reductive doped CP to the neutral state.[76]

The processability of CP is another major research issue. The conjugated backbone of a CP acts like a rigid rod, which becomes less and less soluble in common organic solvents. Alkyl side chains can be added to improve the solubility of CP.[77] The addition of appropriate side chains with different alkyl chain lengths is also a method for controlling the molecular weight. In addition to organic soluble CPs, water soluble CPs can be made by the addition of polar groups to the side chains, such as sulfonate groups for positively charged CP[78] and amine groups for negatively charged CP[79].

It is worth noting that CPs are unstable in air. They will slowly oxidize in the air and form carbonyl groups.[76] This process is irreversible and the resultant carbonyl groups will break the conjugation of the polymer backbone, causing the CP to lose the semiconductor properties. In this regard, CPs made up of pure aromatic rings, such as polyfluorene, are more stable.[80]

Charge and energy transfer in nanocrystals and conjugated polymers

Energy flow between the two semiconductor components, namely, NC and CP, can be described by two possible mechanisms. They are Dexter electron transfer mechanism and Föster energy transfer mechanism.[81] The wave functions of the two semiconductor

components have to overlap in the case of Dexter electron transfer mechanism. Therefore, NC and CP need to be near to each other with a spacing no more than 2 nm.[81] Generally, the surface passivating ligands on the NCs need to be removed or replaced with much shorter ligands to reduce the spacing and provide intimate contact between NCs and CPs. On the other hand, the Förster energy transfer mechanism, which is a weak Coulomb dipole-dipole interaction, can be present with much larger spacing (as large as 10 nm). This process is dependent upon the spectral overlap between the donor photoluminescence and acceptor absorption. Therefore, it is not necessary to strip off surface passivating ligands.[82]

The electron and energy transfer between NCs and CPs occur in solar cells and light emitting diodes, respectively. In solar cells, the CP serves as a hole transporter and the NC serves as electron transporter. Photo induced charge separation between NC, CdSe and CP, poly[2- methoxy, 5-(2'-ethyl-hexyloxy)-1,4-phenylene vinylene] (MEH-PPV) was first observed by Alivisatos et al in 1996; the first organic solar cell was thus fabricated.[83, 84] Subsequently, Alivisatos and his collaborators focused on the improvement of the power conversion efficiency by using CPs with high hole mobility and the NCs with different shapes.[6, 85-89] The photo-induced charge separation and the electron injection from CP to NC have been explored extensively.[90-92] In 2003, Alivisatos et al illustrated the charge transport in the hybrid NC/CP solar cells mathematically.[89] They employed the Schottky equation modified to include series and shunt resistance at low current levels. At high current, an improved model was used to include both the Schottky equation and the presence of a space-charge limited region. The Föster energy transfer from CP or conjugated oligomer toward NC can be evidenced by the quenching of the PL signal of CP or conjugated oligomer.[93-96]

Nanocrystal–conjugated polymer nanocomposites

Placing CPs in direct contact with a NC (i.e., preparing NC-CP nanocomposites) carries advantage over cases where NC aggregation dominates. Such NC-CP nanocomposites

possess a well-defined interface that significantly promotes the charge or energy transfer between these two components. However, very few studies have centered on such direct integration. Milliron et al. synthesized the first phosphoric acid terminated P3HT oligomers and grafted them onto a CdSe surface via ligand exchange.[97] By a similar ligand exchange route, Advincula chemically anchored a dendritic thiophene compound with a phosphoric acid root onto a CdSe surface.[98] In conjunction with direct ligand exchange method, amine terminated polythiophene was mixed with NCs to help improve the nanoscale phase separation, thereby enhancing the resulting photovoltaic properties.[99] Recently, oligomeric MEH-PPV was grafted directly from a CdSe surface.[100] The efficient energy transfer from conjugated oligomeric MEH-PPV to CdSe was observed. The length of these conjugated oligomers, however, was shorter than the conjugation length of the corresponding CPs, making it impossible to further manipulate the photophysics of the nanohybrids by controlling the chain conformation of CPs. The molecular nature of NC−CP nanocomposites is critical to understanding their optoelectronic properties. Moreover, further improvement in the performance of NC−CP nanocomposite-based solar cells and LEDs will rely on new ways of tailoring the polymer chain conformation (e.g., confining NC−CP nanocomposite in nanoscopic geometries), and thus electronic interactions between NC and CP. However, this has not been explored yet.

Nanocrystals and conjugated polymers in confined geometries

Nanoporous membranes

Nanoporous membranes are the first confinement geometry that will be employed in the studies. Nanoporous alumina membrane (PAM) [101]is made by anodization in electrolyte solutions, such as oxalic acid, sulfuric acid, or hydrofluoric acid.

Nanoporous alumina membrane (PAM) PAM has been widely studied in the past decade. The dimension of the membrane in terms of pore size, pore separation, film

thickness, and the order of the pore array can be well-controlled by manipulating the anodization conditions.[103] The distance between two adjacent nanopores, λ and the diameter of the pore, D are determined by the anodization voltage.[104] Higher voltage yields larger λ and bigger D. It is noteworthy that the acidity of the electrolyte solution needs to be balanced with the anodization voltage. In general, small, medium-sized, and large pores, can be fabricated in sulfuric acid, oxalic acid, and phosphoric acid, respectively.

It was found that the highly regular PAM with $\lambda \sim 110$ nm and $D \sim 60$ nm can be readily obtained by anodizing aluminum foil in 0.3 M oxalic acid at 42 V under 0 °C ice/water bath.[105] To obtain a membrane with bigger or smaller pores in hexagonal arrays, it is necessary to delicately control the ramping of the anodization voltage at the early stage of the fabrication.[106] The thickness of the PAM is determined solely by anodization time.

PAM has been used extensively as a template to synthesize one-dimensional nanostructures with functional electronic characteristics, e.g. nanowires.[107] Only recently has it been employed to control optical properties of colloid particles[108] and conjugated polymers[109] and to detect biomolecular binding[110] by monitoring the absorption, emission, and reflectivity spectra. The large surface area of the PAM associated with the nanoporous structure facilitates a substantial change in refractive index upon the deposition of the molecules. The placement of either NCs or CPs can be achieved by dipcoating[111] or melt filling.[112-114] The emission maximum of MEH-PPV were found to blueshift upon being filled inside PAM.[115] This indicates that the polymer chains were isolated from each other. The greatest blueshift was observed for the PAM with the smallest pore size (18 nm). It was also suggested that the surface of the alumina might interact with CPs via Lewis acid-base interaction (between Al centers on alumina surface and Lewis acid aromatic rings on CPs), which might help to align the CP chains in the nanopores.[109] Several kinds of NPs have been filled inside PAMs, such as Au NPs,[108, 116] ZnO NPs[117, 118]. The surface plasmon resonance of Au NPs was found to redshift when the concentration of the Au NPs in the PAMs

increased.[116] The fluorescence emission of the ZnO NPs increased by 20 times after they were deposited inside the PAMs.[117, 118]

PAM is also a unique tool to exert confinement effect on block copolymer and liquid crystals. It has been shown that, self-assembly of block copolymer lead to well ordered microphase separation.[119] The polybutadiene (PBD) block preferentially wets the PAM walls and the polystyrene (PS) block forms microdomains parallel to the PAM walls. Several unique hierarchical structures formed as a result. PS cylinder can be aligned parallel to the PAM walls when cylinder forming PS-PBD copolymer is used. Alternating concentric rings form when lamellar forming PS-PBD copolymer is used.[120]

Recently, it was reported that the liquid crystalline nanowires[114] and conjugated polymer[121] exhibit intrinsic anisotropy inside the nanopores. Their anisotropies were studied by X-ray diffraction and light transmission. The enhanced anisotropy of conjugated polymer crystallization inside PAM led to increased charge mobility of the film, which is extremely important for photovoltaic devices.[121]

Sphere-on-flat geometries

The second type of confinement geometry is a sphere-on-flat geometry as illustrated in Figure 3 in which a droplet of solution containing nonvolatile solutes is constrained between a spherical lens and a flat substrate (i.e., sphere-on-flat geometry).

Dynamic self-assembly of nonvolatile solutes through irreversible solvent evaporation of a droplet (unbound liquid) is widely recognized as a non-lithography route to produce intriguing patterns.[124-134] Two main characteristic patterns are known. The best studied is produced by temperature-gradient-induced Marangoni-Bénard convection,[130, 131, 133] which results in irregular polygonal network structures from an upward flow of the warmer lower liquid. The second is the "coffee ring" pattern,[126-128] which forms when the contact line of an evaporating droplet becomes pinned, ensuring that liquid evaporating from the edge is

replenished by liquid from the interior, so that outward flow carries the nonvolatile element to the edge. A subset of coffee ring phenomena is the concentric ring formed by repeated pinning and depinning events (i.e., stick-slip motion) of the contact line.[124, 135, 136] However, stochastic concentric rings (i.e., irregular rings) are generally formed.[124] Moreover, the bulk of theoretical work within lubrication approximation has centered on understanding a single ring formation.[128, 137, 138] Only very few elegant theoretical studies have focused on periodic multi-rings (i.e., concentric rings) formation during droplet evaporation on a single surface.[124, 135] By employing the sphere-on-Si technique, concentric rings consisting of CPs and organometalic polymers have been reported[95, 139] (Figure 1-3).
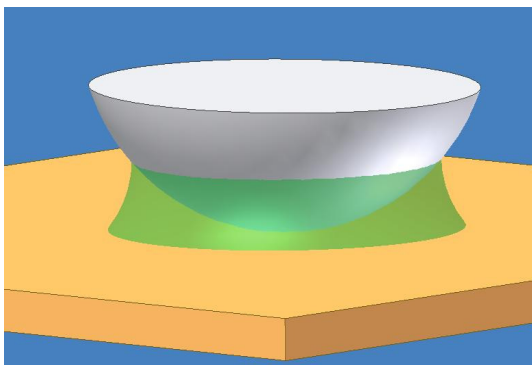
Figure 1-3. Schematic illustration of the sphere-on-flat geometry in which a drop of solution (in green) is constrained, bridging the gap between a spherical lens (in white) and a flat substrate (in yellow).

Organic-inorganic hybrid solar cells

Solar energy has been considered as a promising alternative energy source to traditional fossil fuels. It is a clean energy with minimum amount of environmental impact. The past decade witnessed the significant increase of both production and consumption of solar energy.[140] However, solar energy still suffers from high cost which prevents it from being widely used. According to the U.S. Department of Energy (DOE), the cost for

producing electricity from photovoltaic modules needs to be lower than $0.33/W, which is much lower than the current module price ($4/W in the year 2000).[141]

The current market for solar cell module production is still dominated by the single crystal and polycrystalline silicon modules. The power conversion efficiency (PCE) of these modules has approached 31% in the lab, which is the theoretical thermodynamic maximum (Figure 1-4).[142] The PCE of current commercial available module also exceeds 15%, which is the minimum requirement for a module to be integrated into a device for practical usage. And most importantly, such modules can utilize reject materials from the semiconductor industry, which further reduces the manufacturing cost for these modules. However, there are also significant disadvantages for those single crystals or polycrystalline silicon modules.[140, 143] First of all, they are intrinsically not ideal as photovoltaic materials due to their low absorption, especially in the infrared region. Secondly, there has been less room for PCE improvement. Thirdly, the supply is often affected by the semiconductor industry.
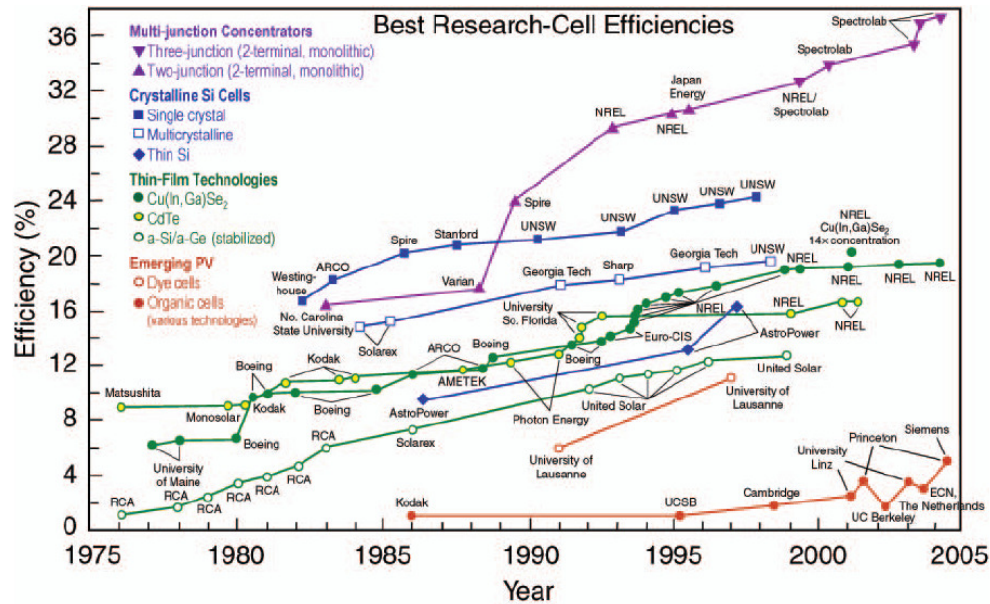
Figure 1-4. Progress of research-scale photovoltaic device efficiencies for a variety of technologies.[141]

To further reduce the module price below \$1/W and make solar energy cost competitive with fossil fuel, new technology or new materials will be needed. The traditional fabrication method of single crystal (first generation) or multicrystalline silicon (second generation) modules will not be able to further reduce the cost (Figure 5).[144] The third generation modules are expected to deliver the ultimate cost reduction. The first kind of approach is to improve the fabrication method on traditional silicon modules (IIIa in Figure 1-4), such as multi-junction concentrators. At relatively low fabrication price, these techniques can produce PCE exceeding the theoretical thermodynamic limit of 31%. As shown in Figure 3, PCE as high as 38% has been achieved in research labs. And the second kind of approach is to fabricate organic solar cells which can produce modest PCE at low cost (IIIb in Figure 1-5).[145]
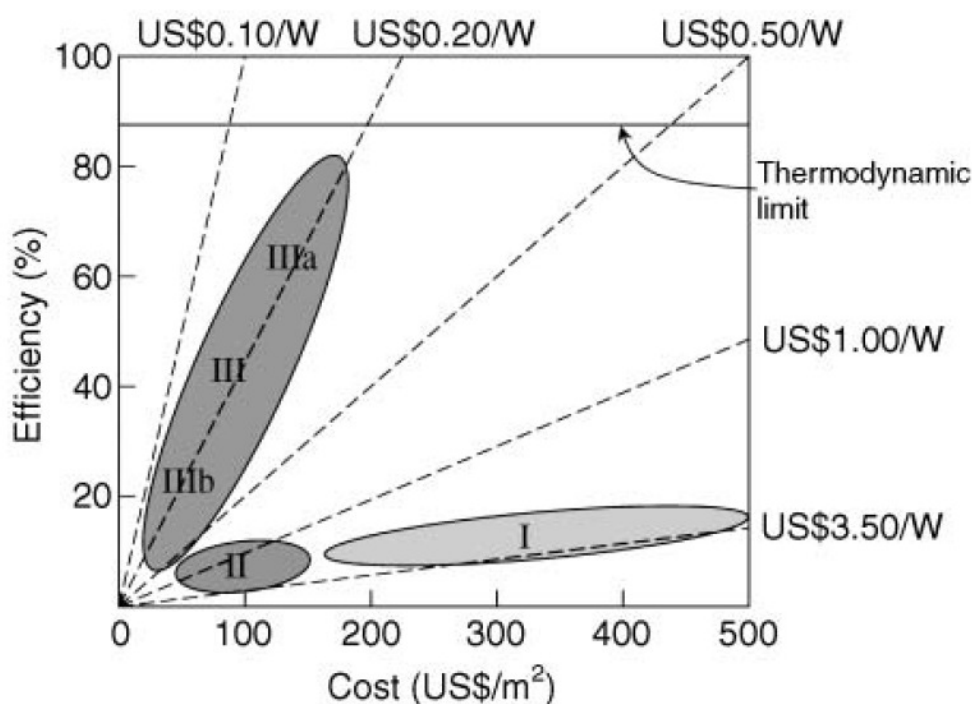
Figure 1-5. Cost efficiency analysis for first, second and third generation photovoltaic technologies (labeled I, II, and III, respectively). [141, 144]

The generation of electrical current under light is illustrated in Figure 1-6. In principle, an organic solar cell is made up of a p-n junction.[146] Upon absorption of light, a mobile excited state, called exciton, instead of a free electron-hole pair was generated. The exciton diffused toward the boundary of the p-n junction and was dissociated. The free electrons and holes were transported toward the electrodes. The efficiency of the process was limited by several factors, the absorption of the light, the charge transport toward the electrodes and the diffusion of the excitons toward the donor/acceptor boundary. Therefore, the research efforts has been concentrated on manipulating these factors.
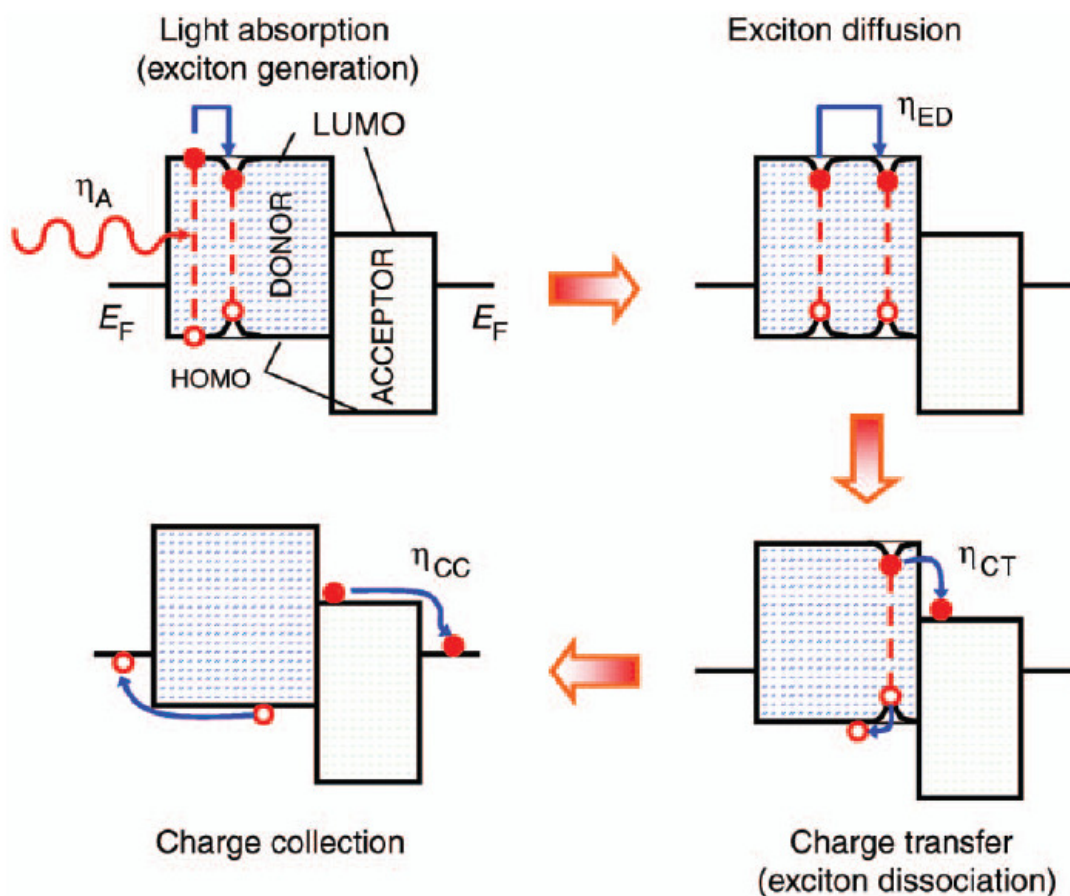
Figure 1-6. Photovoltaic mechanism for an organic solar cell. [146]

The enhanced absorption can be achieved by fabricating thicker devices.[147] However, it also results into longer electrical path and greater charge recombination. The components of organic solar cells are semiconductors, whose electric conductances are relatively low. Therefore, there is an optimal device thickness for organic photovoltaic devices.[148] In other words, the extra amount of power gained by absorbing more sunlight will be lost during the charge transport process due to longer electric path. Another method to improve light absorption is to utilize materials that absorb light at all wavelengths, and most importantly at the IR region of the sun light spectrum, which requires the utilization of low band gap materials.[149] The diffusion of excitons is the most important step in affecting the performance of an organic solar cell device. The exciton can only diffuse over a distance less than 10 nm.[146, 147] If an exciton cannot reach a donor/acceptor interface within a distance of 10 nm, the electron and hole recombines. This indicates that the phase separation of the donor and the acceptor should be in the range of 10 nm.

Several kinds of organic solar cells have been explored, including hybrid bulk heterojunction cells,[150] dye sensitized solar cells,[151] and electrochemical cells[152]. In our research, we focus on the fabrication and characterizations of hybrid bulk heterojunction cells and dye sensitized solar cells only as will be detailed in the Section 3.

Hybrid bulk heterojunction cells The bulk heterojunction cells typically consist of CPs and inorganic compounds, such as NCs,[87] fullerenes,[153] or carbon nanofibers[90, 154] (i.e., organic-inorganic solar cells). A typical solar cell fabricated by sandwiching a spin-coated film of NC/CP mixture (i.e., the blend of CdSe/polythiophene) between a transparent electrode (indium–tin–oxide (ITO) glass or fluorine-doped tin oxide (FTO) glass) and a reflective electrode (Al in most cases) as shown in Figure 1-7.[87]
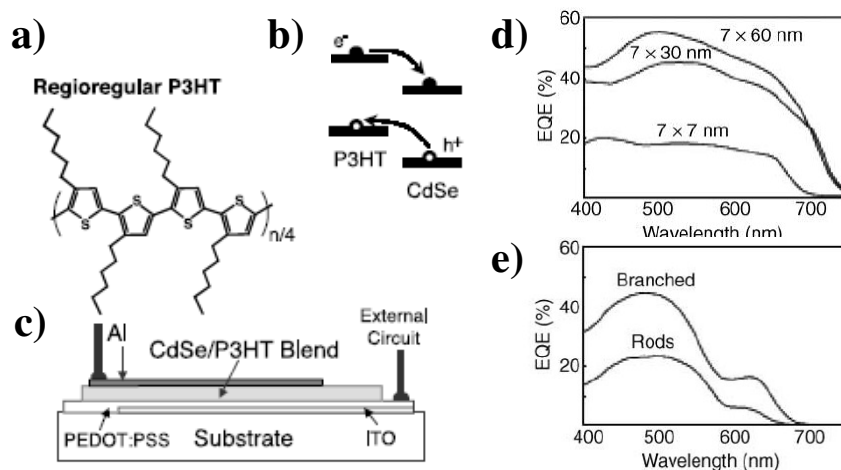
Figure 1-7. (a) The structure of regioregular P3HT (b) The schematic energy level diagram for CdSe nanorods and P3HT showing the charge transfer of electrons to CdSe and holes to P3HT. (c) The device structure consists of a film ~200 nm in thickness sandwiched between an aluminum electrode and a transparent conducting electrode of PEDOT:PSS, which was deposited on an indium tin oxide glass substrate. (d) Dependence of external quantum efficiency (EQE) on nanorod length for CdSe-P3HT hybrid solar cells. (e) Comparison of EQE for CdSe rods and branched nanocrystals hybrid solar cells. [87, 151]

Poly(*p*-phenylene vinylene) and polythiophene derivatives are the common CPs for organic-inorganic solar cells.[155-157] Polythiophene derivatives are especially important for solar cells and they have attracted tremendous research interest due to their high charge mobility at the crystalline state. It was found out that the shape of the NCs exerts a profound influence on the performance of the solar cells.[87, 157] In general, NCs with higher aspect ratio (high length to diameter ratio, i.e., preparing nanorods) and higher degree of branching (e.g., tetrapods) can produce cells with greater external quantum efficiency and higher power conversion efficiency (PCE) (Figure 1-7). The processing conditions, such as solvent casting[158], film preparation methods[159], and post thermal treatments[156, 160] also play important

roles in affecting the solar cell performance. It was found that trichlorobenzene and chlorobenzene help improve the smoothness of the as-spun film, which led into finer phase separation and higher PCE.[158] The most intensively used fabrication method is spin-coating.[87, 88] However, other methods have also been investigated, such as screen-printing[159, 161] and ink-jet printing[78, 162, 163]. Recently, it was demonstrated that doctor blading, which is favorable in industrial fabrication of large area devices, can produce solar cells with decent performance as well.[164]

Dye-sensitized solar cells The study of dye sensitized solar cell (DSSC) can be dated back to 1960s, when it was found out that the electrons from organic dye can be excited under light and be injected into the conductive band of the semiconductor substrate.[165] TiO_2 has served as the semiconductor substrate since then, even though other substrates such as ZnO, SnO_2, and Nb_2O_5 have also been studied.[166-168] Grätzel has been the main investigator in the field of DSSC since 1980s. In 1984, Grätzel reported a high sensitizing efficiency using the combination of TiO_2 colloid and tris(2,2-bipyridyl, 4,4'-carboxylate)ruthenium(II).[169] He made a dye-sensitized TiO_2 NC based solar cell with 7.1% PCE in 1991.[170] A further increase in PCE (up to 10.4%) was realized in 1996, which is by far the most efficient organic solar cell.[171]

A DSSC consists of three major components: dye, hole-conducting electrolyte, and semiconductor substrate.[150] The research efforts have been concentrated on these three fields to optimize the performance of DSSC. The first group of research efforts was the exploration and development of new dyes. The ideal sensitizer (i.e., dye) is expected to have a broad absorption band.[150] Its redox potential needs to be high enough for rapid regeneration by charge donation from the electrolyte. Organometallic compounds have been the only choice, until recently when CdSe QDs were attempted as an alternative.[172] The hole-conducting electrolyte is second factor affecting the performance of DSSC. The commonly used electrolytes include ionic liquid spiro-MeOTAD,[173] CuI,[174] p-type semiconductor CuSCN,[175]

and amorphous organic arylamine (hole transmitting solid).[176] Another new option is to use polymer electrolyte instead of the abovementioned liquid electrolytes.[177, 178] Furthermore, CPs have recently been employed to replace both electrolyte and dye for use in DSSC.[179-184] Finally, the TiO_2 morphology should be optimized. Even though the electron mobility of TiO_2 is surprisingly high,[185] the randomly dispersed TiO_2 nanoparticle layer still elongates the actual traveling distance of electrons toward the electrode, which leads to enhanced scattering of free electrons. Therefore, an ordered TiO_2 structure should yield better DSSC with enhanced PCE. There have been several methods to prepare ordered TiO_2 structures. Eptiaxial TiO_2 has been grown on electrode to investigate its photovoltaic response.[186] In 2005, Grätzel et al reported that the PCE can be improved from 2.21% to 4.04% by simply fabricating an ordered mesoporous TiO_2 layer.[187] Toyoda et al used of TiO_2 nanowire and nanotubes for fabricating DSSC.[172] However, the most striking advance has been reported by Grimes et al. They successfully prepared highly-ordered TiO_2 nanotube arrays by anodization.[123] A 2.9% PCE was achieved from a 360nm thick nanostructured film.[122] It was suggested that an even higher PCE could be obtained simply by increasing the length of the nanotube arrays to several micrometers.

References

1. Cordero, S.R., Carson, P.J., Estabrook, R.A., Strouse, G.F. & Buratto, S.K. Photo-activated luminescence of CdSe quantum dot monolayers. *Journal of Physical Chemistry B* **104**, 12137-12142 (2000).

2. Medintz, I.L., Uyeda, H.T., Goldman, E.R. & Mattoussi, H. Quantum dot bioconjugates for imaging, labelling and sensing. *Nature Materials* **4**, 435-446 (2005).

3. Leatherdale, C.A., Woo, W.K., Mikulec, F.V. & Bawendi, M.G. On the absorption cross section of CdSe nanocrystal quantum dots. *Journal of Physical Chemistry B* **106**, 7619-7622 (2002).

4. Chan, W.C.W. & Nie, S.M. Quantum dot bioconjugates for ultrasensitive nonisotopic detection. *Science* **281**, 2016-2018 (1998).

5. Coe, S., Woo, W.K., Bawendi, M. & Bulovic, V. Electroluminescence from single monolayers of nanocrystals in molecular organic devices. *Nature* **420**, 800-803 (2002).

6. Huynh, W.U., Peng, X.G. & Alivisatos, A.P. CdSe nanocrystal rods/poly(3-hexylthiophene) composite photovoltaic devices. *Advanced Materials* **11**, 923-+ (1999).

7. Medintz, I.L. et al. Self-assembled TNT biosensor based on modular multifunctional surface-tethered components. *Analytical Chemistry* **77**, 365-372 (2005).

8. Ozin, G.A. & Arsenault, A.C. Nanochemistry: A Chemical Approach to Nanomaterials. (Thomas Graham House, Cambridge, U.K; 2005).

9. Murray, C.B., Norris, D.J. & Bawendi, M.G. Synthesis and Characterization of Nearly Monodisperse Cde (E = S, Se, Te) Semiconductor Nanocrystallites. *Journal of the American Chemical Society* **115**, 8706-8715 (1993).

10. Empedocles, S.A. & Bawendi, M.G. Quantum-confined stark effect in single CdSe nanocrystallite quantum dots. *Science* **278**, 2114-2117 (1997).

11. Alivisatos, A.P. Semiconductor clusters, nanocrystals, and quantum dots. *Science* **271**, 933-937 (1996).

12. Peng, X.G. et al. Shape control of CdSe nanocrystals. *Nature* **404**, 59-61 (2000).

13. Peng, Z.A. & Peng, X.G. Formation of high-quality CdTe, CdSe, and CdS nanocrystals using CdO as precursor. *Journal of the American Chemical Society* **123**, 183-184 (2001).

14. Manna, L., Scher, E.C. & Alivisatos, A.P. Synthesis of soluble and processable rod-, arrow-, teardrop-, and tetrapod-shaped CdSe nanocrystals. *Journal of the American Chemical Society* **122**, 12700-12706 (2000).

15. Li, L.S., Hu, J.T., Yang, W.D. & Alivisatos, A.P. Band gap variation of size- and shape-controlled colloidal CdSe quantum rods. *Nano Letters* **1**, 349-351 (2001).

16. Pradhan, N., Xu, H.F. & Peng, X.G. Colloidal CdSe quantum wires by oriented attachment. *Nano Letters* **6**, 720-724 (2006).

17. Milliron, D.J. et al. Colloidal nanocrystal heterostructures with linear and branched topology. *Nature* **430**, 190-195 (2004).

18. Panda, A.B., Glaspell, G. & El-Shall, M.S. Microwave synthesis of highly aligned ultra narrow semiconductor rods and wires. *Journal of the American Chemical Society* **128**, 2790-2791 (2006).

19. Tang, Z.Y., Kotov, N.A. & Giersig, M. Spontaneous organization of single CdTe nanoparticles into luminescent nanowires. *Science* **297**, 237-240 (2002).

20. Shubina, T.V. et al. Optical studies of carrier transport phenomena in CdSe/ZnSe fractional monolayer superlattices. *Thin Solid Films* **336**, 377-380 (1998).

21. Klein, D.L., McEuen, P.L., Katari, J.E.B., Roth, R. & Alivisatos, A.P. An approach to electrical studies of single nanocrystals. *Applied Physics Letters* **68**, 2574-2576 (1996).

22. Millo, O., Katz, D., Cao, Y.W. & Banin, U. Imaging and spectroscopy of artificial-atom states in core/shell nanocrystal quantum dots. *Physical Review Letters* **86**, 5751-5754 (2001).

23. Bakkers, E. & Vanmaekelbergh, D. Resonant electron tunneling through semiconducting nanocrystals in a symmetrical and an asymmetrical junction. *Physical Review B* **62**, R7743-R7746 (2000).

24. Steiner, D. et al. Zero-dimensional and quasi one-dimensional effects in semiconductor nanorods. *Nano Letters* **4**, 1073-1077 (2004).

25. Nahum, E. et al. Transport and charging in single semiconductor nanocrystals studied by conductance atomic force microscopy. *Nano Letters* **4**, 103-108 (2004).

26. Drndic, M., Jarosz, M.V., Morgan, N.Y., Kastner, M.A. & Bawendi, M.G. Transport properties of annealed CdSe colloidal nanocrystal solids. *Journal of Applied Physics* **92**, 7498-7503 (2002).

27. Ginger, D.S. & Greenham, N.C. Charge injection and transport in films of CdSe nanocrystals. *Journal of Applied Physics* **87**, 1361-1368 (2000).

28. Morgan, N.Y. et al. Electronic transport in films of colloidal CdSe nanocrystals. *Physical Review B* **66** (2002).

29. Yu, D., Wang, C.J. & Guyot-Sionnest, P. n-type conducting CdSe nanocrystal solids. *Science* **300**, 1277-1280 (2003).

30. Oertel, D.C., Bawendi, M.G., Arango, A.C. & Bulovic, V. Photodetectors based on treated CdSe quantum-dot films. *Applied Physics Letters* **87** (2005).

31. Romero, H.E., Calusine, G. & Drndic, M. Current oscillations, switching, and hysteresis in CdSe nanorod superlattices. *Physical Review B* **72** (2005).

32. Pradhan, S. et al. Photo-gated charge transfer of organized assemblies of CdSe quantum dots. *Langmuir* **22**, 787-793 (2006).

33. Choudhury, K.R., Samoc, M., Patra, A. & Prasad, P.N. Charge carrier transport in poly(N-vinylcarbazodle): CdS quantum dot hybrid nanocomposite. *Journal of Physical Chemistry B* **108**, 1556-1562 (2004).

34. Choudhury, K.R., Winiarz, J.G., Samoc, M. & Prasad, P.N. Charge carrier mobility in an organic-inorganic hybrid nanocomposite. *Applied Physics Letters* **82**, 406-408 (2003).

35. Houtepen, A.J. & Vanmaekelbergh, D. Orbital occupation in electron-charged CdSe quantum-dot solids. *Journal of Physical Chemistry B* **109**, 19634-19642 (2005).

36. Li, C.P., Wei, K.H. & Huang, J.Y. Enhanced collective electron transport by CdSe quantum dots confined in the poly(4vinylpyridine) nanodomains of a poly(styrene-b-4-vinylpyridine) diblock copolymer thin film. *Angewandte Chemie-International Edition* **45**, 1449-1453 (2006).

37. Franceschetti, A. & Zunger, A. Exciton dissociation and interdot transport in CdSe quantum-dot molecules. *Physical Review B* **63**, 15 (2001).

38. van de Lagemaat, J. Einstein relation for electron diffusion on arrays of weakly coupled quantum dots. *Physical Review B* **72** (2005).

39. Fujisawa, T., Austing, D.G., Hirayama, Y. & Tarucha, S. Electrical pump and probe measurements of a quantum dot in the coulomb blockade regime. *Japanese Journal of Applied Physics Part 1-Regular Papers Short Notes & Review Papers* **42**, 4804-4808 (2003).

40. Tew, M. *Annalytical Physics (Leipzig)* **13**, 249-304 (2004).

41. Vanmaekelbergh, D. & Liljeroth, P. Electron-conducting quantum dot solids: novel materials based on colloidal semiconductor nanocrystals. *Chemical Society Reviews* **34**, 299-312 (2005).

42. Duan, X.F., Huang, Y., Agarwal, R. & Lieber, C.M. Single-nanowire electrically driven lasers. *Nature* **421**, 241-245 (2003).

43. Greytak, A.B., Barrelet, C.J., Li, Y. & Lieber, C.M. Semiconductor nanowire laser and nanowire waveguide electro-optic modulators. *Applied Physics Letters* **87** (2005).

44. Tang, Z.Y., Wang, Y., Sun, K. & Kotov, N.A. Spontaneous transformation of stabilizer-depleted binary semiconductor nanoparticles into selenium and tellurium nanowires. *Advanced Materials* **17**, 358 (2005).

45. Law, M. et al. Nanoribbon waveguides for subwavelength photonics integration. *Science* **305**, 1269-1273 (2004).

46. Hayden, O., Greytak, A.B. & Bell, D.C. Core-shell nanowire light-emitting diodes. *Advanced Materials* **17**, 701 (2005).

47. Gu, Y., Romankiewicz, J.P., David, J.K., Lensch, J.L. & Lauhon, L.J. Quantitative measurement of the electron and hole mobility-lifetime products in semiconductor nanowires. *Nano Letters* **6**, 948-952 (2006).

48. Xie, Y., Xu, J.J., Yu, J.S. & Chen, H.Y. Synthesis and characterization of water-soluble CdSe/ZnS core-shell nanoparticles. *Chinese Journal of Inorganic Chemistry* **20**, 663-667 (2004).

49. Smith, A.M., Gao, X.H. & Nie, S.M. Quantum dot nanocrystals for in vivo molecular and cellular imaging. *Photochemistry and Photobiology* **80**, 377-385 (2004).

50. Hoshino, A. et al. Quantum dots targeted to the assigned organelle in living cells. *Microbiology and Immunology* **48**, 985-994 (2004).

51.   Nguyen, L.H. et al. Precursor route poly(thienylene vinylene) for organic solar cells: Photophysics and photovoltaic performance. *Solar Energy Materials and Solar Cells* **90**, 2815-2828 (2006).

52.   Van De Wetering, K., Brochon, C., Ngov, C. & Hadziioannou, G. Design and synthesis of a low band gap conjugated macroinitiator: Toward rod-coil donor-acceptor block copolymers. *Macromolecules* **39**, 4289-4297 (2006).

53.   Mozer, A.J. & Sariciftci, N.S. Conjugated polymer photovoltaic devices and materials. *Comptes Rendus Chimie* **9**, 568-577 (2006).

54.   Duprez, V., Biancardo, M., Spanggaard, H. & Krebs, F.C. Synthesis of conjugated polymers containing terpyridine-ruthenium complexes: Photovoltaic applications. *Macromolecules* **38**, 10436-10448 (2005).

55.   Sirringhaus, H., Tessler, N. & Friend, R.H. Integrated optoelectronic devices based on conjugated polymers. *Science* **280**, 1741-1744 (1998).

56.   Ho, P.K.H. et al. Molecular-scale interface engineering for polymer light-emitting diodes. *Nature* **404**, 481-484 (2000).

57.   Dhoot, A.S. et al. Beyond the metal-insulator transition in polymer electrolyte gated polymer field-effect transistors. *Proceedings of the National Academy of Sciences of the United States of America* **103**, 11834-11837 (2006).

58.   Yamamoto, T., Sakai, Y. & Aramaki, S. pi-conjugated poly(1,10-phenanthroline)-Ru-II(bpy)(2) complex as an n-type active material for FET. *Bulletin of the Chemical Society of Japan* **79**, 959-961 (2006).

59.   Matsui, J., Yoshida, S., Mikayama, T., Aoki, A. & Miyashita, T. Fabrication of polymer Langmuir-Blodgett films containing regioregular poly(3-hexylthiophene) for application to field-effect transistor. *Langmuir* **21**, 5343-5348 (2005).

60.   Cheng, F. et al. A cationic water-soluble, poly(p-phenylenevinylene) derivative: Highly sensitive biosensor for iron-sulfur protein detection a. *Macromolecular Rapid Communications* **27**, 799-803 (2006).

61.   Yokoyarna, K. & Taira, S. in Immobilisation of DNA on Chips Ii, Vol. **261** 91-112 (2005).

62. Lefenfeld, M., Blanchet, G. & Rogers, J.A. High-performance contacts in plastic transistors and logic gates that use printed electrodes of DNNSA-PANI doped with single-walled carbon nanotubes. *Advanced Materials* **15**, 1188 (2003).

63. Hoofman, R., de Haas, M.P., Siebbeles, L.D.A. & Warman, J.M. Highly mobile electrons and holes on isolated chains of the semiconducting polymer poly(phenylenevinylene). *Nature* **392**, 54-56 (1998).

64. Horowitz, G., Garnier, F., Yassar, A., Hajlaoui, R. & Kouki, F. Field-effect transistor made with a sexithiophene single crystal. *Advanced Materials* **8**, 52-& (1996).

65. Kaynak, A., Polat, A. & Yilmazer, U. Some microwave and mechanical properties of carbon fiber-polypropylene and carbon black-polypropylene composites. *Materials Research Bulletin* **31**, 1195-1206 (1996).

66. Horowitz, G. et al. Structure-dependent fluorescence in sexithiophene single crystals. *Advanced Materials* **11**, 234 (1999).

67. Schwartz, B.J. Conjugated polymers as molecular materials : How chain conformation and film morphology influence energy transfer and interchain interactions. *Annual Review of Physical Chemistry* **54**, 141-172 (2003).

68. Ito, T., Shirakaw.H & Ikeda, S. Simultaneous Polymerization and Formation of Polyacetylene Film on Surface of Concentrated Soluble Ziegler-Type Catalyst Solution. *Journal of Polymer Science Part a-Polymer Chemistry* **12**, 11-20 (1974).

69. Shirakawa, H., Louis, E.J., Macdiarmid, A.G., Chiang, C.K. & Heeger, A.J. Synthesis of Electrically Conducting Organic Polymers - Halogen Derivatives of Polyacetylene, (Ch)X. *Journal of the Chemical Society-Chemical Communications*, 578-580 (1977).

70. Burroughes, J.H. et al. Light-Emitting-Diodes Based on Conjugated Polymers. *Nature* **347**, 539-541 (1990).

71. Weder, C. Synthesis, processing and properties of conjugated polymer networks. *Chemical Communications*, 5378-5389 (2005).

72. Wang, Z.H., Li, C., Scherr, E.M., Macdiarmid, A.G. & Epstein, A.J. 3 Dimensionality of Metallic States in Conducting Polymers - Polyaniline. *Physical Review Letters* **66**, 1745-1748 (1991).

73. Bao, Z., Dodabalapur, A. & Lovinger, A.J. Soluble and processable regioregular poly(3-hexylthiophene) for thin film field-effect transistor applications with high mobility. *Applied Physics Letters* **69**, 4108-4110 (1996).

74. Chang, J.F. et al. Enhanced mobility of poly(3-hexylthiophene) transistors by spin-coating from high-boiling-point solvents. *Chemistry of Materials* **16**, 4772-4776 (2004).

75. Yamamoto, T. et al. Pi-Conjugated Soluble Poly(Aryleneethynylene) Type Polymers - Preparation by Palladium-Catalyzed Coupling Reaction, Nonlinear-Optical Properties, Doping, and Chemical-Reactivity. *Macromolecules* **27**, 6620-6626 (1994).

76. Dale, S.M., Glidle, A. & Hillman, A.R. Spectroelectrochemical Observation of Poly(Benzo[C]Thiophene) N-Doping and P-Doping. *Journal of Materials Chemistry* **2**, 99-104 (1992).

77. Pron, A. & Rannou, P. Processible conjugated polymers: from organic semiconductors to organic metals and superconductors. *Progress in Polymer Science* **27**, 135-190 (2002).

78. Chang, S.C. et al. Dual-color polymer light-emitting pixels processed by hybrid inkjet printing. *Applied Physics Letters* **73**, 2561-2563 (1998).

79. Liu, B., Yu, W.L., Lai, Y.H. & Huang, W. Blue-light-emitting cationic water-soluble polyfluorene derivatives with tunable quaternization degree. *Macromolecules* **35**, 4975-4982 (2002).

80. Rost, H., Ficker, J., Alonso, J.S., Leenders, L. & McCulloch, L. Air-stable all-polymer field-effect transistors with organic electrodes. *Synthetic Metals* **145**, 83-85 (2004).

81. Willard, D.M., Mutschler, T., Yu, M., Jung, J. & Van Orden, A. Directing energy flow through quantum dots: towards nanoscale sensing. *Analytical and Bioanalytical Chemistry* **384**, 564-571 (2006).

82. Clapp, A.R., Medintz, I.L. & Mattoussi, H. Forster resonance energy transfer investigations using quantum-dot fluorophores. *Chemphyschem* **7**, 47-57 (2006).

83. Greenham, N.C., Peng, X.G. & Alivisatos, A.P. Charge separation and transport in conjugated-polymer/semiconductor-nanocrystal composites studied by

photoluminescence quenching and photoconductivity. *Physical Review B* **54**, 17628-17637 (1996).

84. Greenham, N.C., Peng, X.G. & Alivisatos, A.P. Charge separation and transport in conjugated polymer cadmium selenide nanocrystal composites studied by photoluminescence quenching and photoconductivity. *Synthetic Metals* **84**, 545-546 (1997).

85. Ginger, D.S. & Greenham, N.C. Charge separation in conjugated-polymer/nanocrystal blends. *Synthetic Metals* **101**, 425-428 (1999).

86. Ginger, D.S. & Greenham, N.C. Photoinduced electron transfer from conjugated polymers to CdSe nanocrystals. *Physical Review B* **59**, 10622-10629 (1999).

87. Huynh, W.U., Dittmer, J.J. & Alivisatos, A.P. Hybrid nanorod-polymer solar cells. *Science* **295**, 2425-2427 (2002).

88. Huynh, W.U., Dittmer, J.J., Libby, W.C., Whiting, G.L. & Alivisatos, A.P. Controlling the morphology of nanocrystal-polymer composites for solar cells. *Advanced Functional Materials* **13**, 73-79 (2003).

89. Huynh, W.U. et al. Charge transport in hybrid nanorod-polymer composite photovoltaic cells. *Physical Review B* **67** (2003).

90. Landi, B.J. et al. CdSe quantum dot-single wall carbon nanotube complexes for polymeric solar cells. *Solar Energy Materials and Solar Cells* **87**, 733-746 (2005).

91. McDonald, S.A. et al. Solution-processed PbS quantum dot infrared photodetectors and photovoltaics. *Nature Materials* **4**, 138 (2005).

92. Talapin, D.V., Poznyak, S.K., Gaponik, N.P., Rogach, A.L. & Eychmuller, A. Synthesis of surface-modified colloidal semiconductor nanocrystals and study of photoinduced charge separation and transport in nanocrystal-polymer composites. *Physica E-Low-Dimensional Systems & Nanostructures* **14**, 237-241 (2002).

93. Bakueva, L., Konstantatos, G., Levina, L., Musikhin, S. & Sargent, E.H. Luminescence from processible quantum dot-polymer light emitters 1100-1600 nm: Tailoring spectral width and shape. *Applied Physics Letters* **84**, 3459-3461 (2004).

94. Chang, T.W.F. et al. Efficient excitation transfer from polymer to nanocrystals. *Applied Physics Letters* **84**, 4295-4297 (2004).

95. Hong, S.K. Energy transfer by resonant dipole-dipole interaction from a conjugated polymer to a quantum-dot. *Physica E-Low-Dimensional Systems & Nanostructures* **28**, 66-75 (2005).

96. Warner, J.H. et al. Energy transfer dynamics of nanocrystal-polymer composites. *Journal of Physical Chemistry B* **109**, 9001-9005 (2005).

97. Milliron, D.J., Alivisatos, A.P., Pitois, C., Edder, C. & Frechet, J.M.J. Electroactive surfactant designed to mediate electron transfer between CdSe nanocrystals and organic semiconductors. *Advanced Materials* **15**, 58 (2003).

98. Advincula, R.C. Hybrid organic-inorganic nanomaterials based on polythiophene dendronized nanoparticles. *Dalton Transactions*, 2778-2784 (2006).

99. Liu, J.S., Kadnikova, E.N., Liu, Y.X., McGehee, M.D. & Frechet, J.M.J. Polythiophene containing thermally removable solubilizing groups enhances the interface and the performance of polymer-titania hybrid solar cells. *Journal of the American Chemical Society* **126**, 9486-9487 (2004).

100. Skaff, H., Sill, K. & Emrick, T. Quantum dots tailored with poly(para-phenylene vinylene). *Journal of the American Chemical Society* **126**, 11322-11325 (2004).

101. Jessensky, O., Muller, F. & Gosele, U. Self-organized formation of hexagonal pore arrays in anodic alumina. *Applied Physics Letters* **72**, 1173-1175 (1998).

102. Cai, Q.Y., Paulose, M., Varghese, O.K. & Grimes, C.A. The effect of electrolyte composition on the fabrication of self-organized titanium oxide nanotube arrays by anodic oxidation. *Journal of Materials Research* **20**, 230-236 (2005).

103. Nielsch, K., Choi, J., Schwirn, K., Wehrspohn, R.B. & Gosele, U. Self-ordering regimes of porous alumina: The 10% porosity rule. *Nano Letters* **2**, 677-680 (2002).

104. Li, A.P., Muller, F., Birner, A., Nielsch, K. & Gosele, U. Hexagonal pore arrays with a 50-420 nm interpore distance formed by self-organization in anodic alumina. *Journal of Applied Physics* **84**, 6023-6026 (1998).

105. Zhao, Y., Yang, D.R., Zhou, C.Y., Yang, Q. & Que, D.L. Photoluminescence properties of the composite of porous alumina and poly (2,5-dibutoxy-1,4 phenylenevinylene). *Journal of Luminescence* **105**, 57-60 (2003).

106. Masuda, H. et al. Highly ordered nanochannel-array architecture in anodic alumina. *Applied Physics Letters* **71**, 2770-2772 (1997).

107. Mirkin, C.A., Letsinger, R.L., Mucic, R.C. & Storhoff, J.J. A DNA-based method for rationally assembling nanoparticles into macroscopic materials. *Nature* **382**, 607-609 (1996).

108. Hanaoka, T., Kormann, H.P., Kroll, M., Sawitowski, T. & Schmid, G. Three-dimensional assemblies of gold colloids in nanoporous alumina membranes. *European Journal of Inorganic Chemistry*, 807-812 (1998).

109. Qi, D.F., Kwong, K., Rademacher, K., Wolf, M.O. & Young, J.F. Optical emission of conjugated polymers adsorbed to nanoporous alumina. *Nano Letters* **3**, 1265-1268 (2003).

110. Pan, S.L. & Rothberg, L.J. Interferometric sensing of biomolecular binding using nanoporous aluminum oxide templates. *Nano Letters* **3**, 811-814 (2003).

111. Misner, M.J., Skaff, H., Emrick, T. & Russell, T.P. Directed deposition of nanoparticles using diblock copolymer templates. *Advanced Materials* **15**, 221 (2003).

112. Yamaguchi, A. et al. Self-assembly of a silica-surfactant nanocomposite in a porous alumina membrane. *Nature Materials* **3**, 337-341 (2004).

113. Zhang, M.F. et al. Wetting transition in cylindrical alumina nanopores with polymer melts. *Nano Letters* **6**, 1075-1079 (2006).

114. Steinhart, M. et al. Polymer nanotubes by wetting of ordered porous templates. *Science* **296**, 1997-1997 (2002).

115. Nguyen, T.P., Yang, S.H., Le Rendu, P. & Khan, H. Optical properties of poly(2-methoxy-5-(2'-ethyl-hexyloxy)-phenylene vinylene) deposited on porous alumina substrates. *Composites Part A: Applied Science and Manufacturing* **36**, 515-519 (2005).

116. Wang, J., Lau, W.M. & Li, Q. Effects of particle size and spacing on the optical properties of gold nanocrystals in alumina. *Journal of Applied Physics* **97**, 114303 (2005).

117. Gao, T. et al. Photoluminescence of ZnO nanoparticles loaded into porous anodic alumina hosts. *Journal of Physics-Condensed Matter* **14**, 12651-12656 (2002).

118. Shi, G., Mo, C.M., Cai, W.L. & Zhang, L.D. Photoluminescence of ZnO nanoparticles in alumina membrane with ordered pore arrays. *Solid State Communications* **115**, 253-256 (2000).

119. Xiang, H.Q. et al. Block copolymers under cylindrical confinement. *Macromolecules* **37**, 5660-5664 (2004).

120. Xiang, H.Q. et al. The influence of confinement and curvature on the morphology of block copolymers. *Journal of Polymer Science Part B-Polymer Physics* **43**, 3377-3383 (2005).

121. Coakley, K.M. et al. Enhanced hole mobility in regioregular polythiophene infiltrated in straight nanopores. *Advanced Functional Materials* **15**, 1927-1932 (2005).

122. Mor, G.K., Shankar, K., Paulose, M., Varghese, O.K. & Grimes, C.A. Use of highly-ordered TiO2 nanotube arrays in dye-sensitized solar cells. *Nano Letters* **6**, 215-218 (2006).

123. Mor, G.K., Varghese, O.K., Paulose, M., Shankar, K. & Grimes, C.A. A review on highly ordered, vertically oriented TiO2 nanotube arrays: Fabrication, material properties, and solar energy applications. *Solar Energy Materials and Solar Cells* **90**, 2011-2075 (2006).

124. Adachi, E., Dimitrov, A.S. & Nagayama, K. Stripe Patterns Formed on a Glass-Surface During Droplet Evaporation. *Langmuir* **11**, 1057-1060 (1995).

125. de Gennes, P.G. Solvent evaporation of spin cast films: "crust" effects. *European Physical Journal E* **7**, 31-34 (2002).

126. Deegan, R.D. Pattern formation in drying drops. *Physical Review E* **61**, 475-485 (2000).

127. Deegan, R.D. et al. Capillary flow as the cause of ring stains from dried liquid drops. *Nature* **389**, 827-829 (1997).

128. Deegan, R.D. et al. Contact line deposits in an evaporating drop. *Physical Review E* **62**, 756-765 (2000).

129. Karthaus, O., Grasjo, L., Maruyama, N. & Shimomura, M. Formation of ordered mesoscopic polymer arrays by dewetting. *Chaos* **9**, 308-314 (1999).

130. Mitov, Z. & Kumacheva, E. Convection-induced patterns in phase-separating polymeric fluids. *Physical Review Letters* **81**, 3427-3430 (1998).

131. Nguyen, V.X. & Stebe, K.J. Patterning of small particles by a surfactant-enhanced Marangoni-Benard instability. *Physical Review Letters* **88** (2002).

132. Rabani, E., Reichman, D.R., Geissler, P.L. & Brus, L.E. Drying-mediated self-assembly of nanoparticles. *Nature* **426**, 271-274 (2003).

133. Xu, S.Q. & Kumacheva, E. Ordered morphologies in polymeric films produced by replication of convection patterns. *Journal of the American Chemical Society* **124**, 1142-1143 (2002).

134. Yabu, H. & Shimomura, M. Preparation of self-organized mesoscale polymer patterns on a solid substrate: Continuous pattern formation from a receding meniscus. *Advanced Functional Materials* **15**, 575-581 (2005).

135. Nonomura, M., Kobayashi, R., Nishiura, Y. & Shimomura, M. Periodic precipitation during droplet evaporation on a substrate. *Journal of the Physical Society of Japan* **72**, 2468-2471 (2003).

136. Shmuylovich, L., Shen, A.Q. & Stone, H.A. Surface morphology of drying latex films: Multiple ring formation. *Langmuir* **18**, 3441-3445 (2002).

137. Fischer, B.J. Particle Convection in an Evaporating Colloidal Droplet. *Langmuir* **18**, 60-67 (2002).

138. Popov, Y.O. Evaporative deposition patterns: Spatial dimensions of the deposit. *Physical Review E* **71** (2005).

139. Xu, J. et al. Self-assembly of gradient concentric rings via solvent evaporation from a capillary bridge. *Physical Review Letters* **96** (2006).

140. Goetzberger, A., Hebling, C. & Schock, H.W. Photovoltaic materials, history, status and outlook. *Materials Science & Engineering R-Reports* **40**, 1-46 (2003).

141. Shaheen, S.E., Ginley, D.S. & Jabbour, G.E. Organic-based photovoltaics. toward lowm-cost power generation. *MRS Bulletin* **30**, 10-19 (2005).

142. Chopra, K.L., Paulson, P.D. & Dutta, V. Thin-film solar cells: An overview. *Progress in Photovoltaics* **12**, 69-92 (2004).

143. Goetzberger, A. & Hebling, C. Photovoltaic materials, past, present, future. *Solar Energy Materials and Solar Cells* **62**, 1-19 (2000).

144. Margolis, R.M. in NCPV Solar Program Review Meeting Denver, CO.; 2003).

145. Spanggaard, H. & Krebs, F.C. A brief history of the development of organic and polymeric photovoltaics. *Solar Energy Materials and Solar Cells* **83**, 125-146 (2004).

146. Forrest, S.R. The limits to organic photovoltaic cell efficiency. *MRS Bulletin* **30**, 28-32 (2005).

147. Hoppe, H. & Sariciftci, N.S. Organic solar cells: An overview. *Journal of Materials Research* **19**, 1924-1945 (2004).

148. Gledhill, S.E., Scott, B. & Gregg, B.A. Organic and nano-structured composite photovoltaics: An overview. *Journal of Materials Research* **20**, 3167-3179 (2005).

149. Winder, C. & Sariciftci, N.S. Low bandgap polymers for photon harvesting in bulk heterojunction solar cells. *Journal of Materials Chemistry* **14**, 1077-1086 (2004).

150. Gratzel, M. Dye-sensitized solid-state heterojunction solar cells. *MRS Bulletin* **30**, 23-27 (2005).

151. Milliron, D.J., Gur, I. & Alivisatos, A.P. Hybrid organic - Nanocrystal solar cells. *MRS Bulletin* **30**, 41-44 (2005).

152. Wallace, G.G., Too, C.O., Officer, D.L. & Dastoor, P. Photoelectrochemical cells based on inherently conducting polymers. *MRS Bulletin* **30**, 46-49 (2005).

153. Janssen, R.A.J., Hummelen, J.C. & Saricifti, N.S. Polymer-fullerene bulk heterojunction solar cells. *MRS Bulletin* **30**, 33-36 (2005).

154. Landi, B.J., Raffaelle, R.P., Castro, S.L. & Bailey, S.G. Single-wall carbon nanotube-polymer solar cells. *Progress in Photovoltaics* **13**, 165-172 (2005).

155. Mattoussi, H. et al. Electroluminescence from heterostructures of poly(phenylene vinylene) and inorganic CdSe nanocrystals. *Journal of Applied Physics* **83**, 7965-7974 (1998).

156. Padinger, F., Rittberger, R.S. & Sariciftci, N.S. Effects of postproduction treatment on plastic solar cells. *Advanced Functional Materials* **13**, 85-88 (2003).

157. Sun, B.Q., Snaith, H.J., Dhoot, A.S., Westenhoff, S. & Greenham, N.C. Vertically segregated hybrid blends for photovoltaic devices with improved efficiency. *Journal of Applied Physics* **97** (2005).

158. Wienk, M.M. et al. Efficient methano[70]fullerene/MDMO-PPV bulk heterojunction photovoltaic cells. *Angewandte Chemie-International Edition* **42**, 3371-3375 (2003).

159. Shaheen, S.E., Radspinner, R., Peyghambarian, N. & Jabbour, G.E. Fabrication of bulk heterojunction plastic solar cells by screen printing. *Applied Physics Letters* **79**, 2996-2998 (2001).

160. Kymakis, E., Koudoumas, E., Franghiadakis, I. & Amaratunga, G.A.J. Post-fabrication annealing effects in polymer-nanotube photovoltaic cells. *Journal of Physics D-Applied Physics* **39**, 1058-1062 (2006).

161. Krebs, F.C., Alstrup, J., Spanggaard, H., Larsen, K. & Kold, E. Production of large-area polymer solar cells by industrial silk screen printing, lifetime considerations and lamination with polyethyleneterephthalate. *Solar Energy Materials and Solar Cells* **83**, 293-300 (2004).

162. Tekin, E., Holder, E., Marin, V., de Gans, B.J. & Schubert, U.S. Ink-jet printing of luminescent ruthenium- and iridium-containing polymers for applications in light-emitting devices. *Macromolecular Rapid Communications* **26**, 293-297 (2005).

163. Marin, V. et al. Ink-jet printing of electron donor/acceptor blends: Towards bulk heterojunction solar cells. *Macromolecular Rapid Communications* **26**, 319-324 (2005).

164. Schilinsky, P., Waldauf, C. & Brabec, C.J. Performance analysis of printed bulk heterojunction solar cells. *Advanced Functional Materials* **16**, 1669-1672 (2006).

165. Namba, S. & Hishiki, Y. Color Sensitization of Zinc Oxide with Cyanine Dyes. *Journal of Physical Chemistry* **69**, 774-& (1965).

166. Dareedwards, M.P., Goodenough, J.B., Hamnett, A., Seddon, K.R. & Wright, R.D. Sensitization of Semiconducting Electrodes with Ruthenium-Based Dyes. *Faraday Discussions*, 285-298 (1980).

167. O'Regan, B., Schwartz, D.T., Zakeeruddin, S.M. & Gratzel, M. Electrodeposited nanocomposite n-p heterojunctions for solid-state dye-sensitized photovoltaics. *Advanced Materials* **12**, 1263-+ (2000).

168. Tsubomura, H., Matsumura, M., Nomura, Y. & Amamiya, T. Dye Sensitized Zinc-Oxide - Aqueous-Electrolyte - Platinum Photocell. *Nature* **261**, 402-403 (1976).

169. Dung, D.H., Serpone, N. & Gratzel, M. Integrated Systems for Water Cleavage by Visible-Light - Sensitization of Tio2 Particles by Surface Derivatization with Ruthenium Complexes. *Helvetica Chimica Acta* **67**, 1012-1018 (1984).

170. Oregan, B. & Gratzel, M. A Low-Cost, High-Efficiency Solar-Cell Based on Dye-Sensitized Colloidal Tio2 Films. *Nature* **353**, 737-740 (1991).

171. Nazeeruddin, M.K., Pechy, P. & Gratzel, M. Efficient panchromatic sensitization of nanocrystalline TiO2 films by a black dye based on a trithiocyanato-ruthenium complex. *Chemical Communications*, 1705-1706 (1997).

172. Shen, Q., Sato, T., Hashimoto, M., Chen, C.C. & Toyoda, T. Photoacoustic and photo electrochemical characterization of CdSe-sensitized TiO2 electrodes composed of nanotubes and nanowires. *Thin Solid Films* **499**, 299-305 (2006).

173. Bassler, H. Charge Transport in Disordered Organic Photoconductors - a Monte-Carlo Simulation Study. *Physica Status Solidi B-Basic Research* **175**, 15-56 (1993).

174. Tennakone, K., Kumara, G., Kumarasinghe, A.R., Wijayantha, K.G.U. & Sirimanne, P.M. A Dye-Sensitized Nano-Porous Solid-State Photovoltaic Cell. *Semiconductor Science and Technology* **10**, 1689-1693 (1995).

175. Oregan, B. & Schwartz, D.T. Efficient dye-sensitized charge separation in a wide-band-gap p-n heterojunction. *Journal of Applied Physics* **80**, 4749-4754 (1996).

176. Bach, U. et al. Solid-state dye-sensitized mesoporous TiO2 solar cells with high photon-to-electron conversion efficiencies. *Nature* **395**, 583-585 (1998).

177. Kubo, W. et al. Fabrication of quasi-solid-state dye-sensitized TiO2 solar cells using low molecular weight gelators. *Chemistry Letters*, 1241-1242 (1998).

178. Nogueira, A.F. & De Paoli, M.A. A dye sensitized TiO2 photovoltaic cell constructed with an elastomeric electrolyte. *Solar Energy Materials and Solar Cells* **61**, 135-141 (2000).

179. Arango, A.C. et al. Efficient titanium oxide/conjugated polymer photovoltaics for solar energy conversion. *Advanced Materials* **12**, 1689 (2000).

180. Feng, W., Umeda, T., Fujii, A., Wang, X.G. & Yoshino, K. Enhancement of photoresponse by enlarging the effective interface between conducting polymer and titanium oxide in photovoltaic device. *Japanese Journal of Applied Physics Part 1-Regular Papers Short Notes & Review Papers* **43**, 3473-3478 (2004).

181. Li, L.S., Jia, Q.X. & Li, A.D.Q. Effects of organic self-assembled polymer and metal phthalocyanine multilayers on the surface photovoltaic properties of indium tin oxide and titanium oxide. *Chemistry of Materials* **14**, 1159-1165 (2002).

182. Liu, Y.X. et al. Dependence of band offset and open-circuit voltage on the interfacial interaction between TiO2 and carboxylated polythiophenes. *Journal of Physical Chemistry B* **110**, 3257-3261 (2006).

183. Umeda, T. et al. Ultraviolet light responses in photovoltaic properties of TiO2/conducting polymer heterostructure devices. *Applied Physics Letters* **85**, 3139-3141 (2004).

184. Kim, Y.G., Walker, J., Samuelson, L.A. & Kumar, J. Efficient light harvesting polymers for nanocrystalline TiO2 photovoltaic cells. *Nano Letters* **3**, 523-525 (2003).

185. Burlakov, V.M. et al. Discrete hopping model of exciton transport in disordered media. *Physical Review B* **72** (2005).

186. Park, B.H., Li, L.S., Gibbons, B.J., Huang, J.Y. & Jia, Q.X. Photovoltaic response and dielectric properties of epitaxial anatase-TiO2 films grown on conductive La0.5Sr0.5CoO3 electrodes. *Applied Physics Letters* **79**, 2797-2799 (2001).

187. Zukalova, M. et al. Organized mesoporous TiO2 films exhibiting greatly enhanced performance in dye-sensitized solar cells. *Nano Letters* **5**, 1789-1792 (2005).

CHAPTER 2. SELF-ASSEMBLY OF GRADIENT CONCENTRIC RINGS VIA SOLVENT EVAPORATION FROM A CAPILLARY BRIDGE

Jun Xu, Jianfeng Xia, Suck Won Hong, Zhiqun Lin*, Feng Qiu and Yuliang Yang,

Abstract

A drop of solution containing nonvolatile solute is allowed to evaporate from a sphere-on-flat geometry. Left behind is a striking pattern of *gradient* concentric rings with unprecedented regularity. The center-to-center distance between adjacent rings, λ_{C-C} and the height of the ring, h_d are strongly affected by the concentration of the solution and the surface tension of the solvent. The nature of the formation of regular *gradient* ring patterns during the course of irreversible solvent evaporation is revealed through theoretical calculations based on the mass conservation of the solution.

Introduction

Dynamic self-assembly of nonvolatile solutes through irreversible solvent evaporation of a droplet (*unbound liquid*) is widely recognized as a nonlithography route toroduce intriguing patterns.[1-10] Two main characteristic patterns are known. The best studied is produced by temperature-gradient-induced Marangoni-Be´nard convection,[8-10] which results in irregular polygonal network structures from an upward flow of the warmer lower liquid. The second is the ''coffee ring'' pattern,[1-3] which forms when the contact line of an

evaporating droplet becomes pinned, ensuring that liquid evaporating from the edge is replenished by liquid from the interior, so that outward flow carries the nonvolatile element to the edge. A subset of the coffee ring phenomena is the concentric ring formed by repeated pinning and depinning events (i.e., stick-slip motion) of the contact line.[11-13] However, stochastic concentric rings (i.e., irregular rings) are generally formed.[11] Moreover, the bulk of theoretical work within lubrication approximation has centered on understanding a *single* ring formation.[3, 14, 15] Only very few elegant theoretical studies have focused on periodic multiring (i.e., concentric rings) formation during droplet evaporation on a single surface.[11, 12]

To date, a few attempts have been made to control a droplet evaporation in a confined geometry (*bound liquid*).[6, 16, 17] Recently, a periodic family of concentric ring patterns with unprecedented regularity have been produced by constraining a drop of polymer solution in a confined geometry composed of either two cylindrical mica surfaces placed at right angle to one another[16] or a sphere on a flat surface.[17] However, the nature of the formation of such highly regular patterns remains to be addressed.

In this Letter, we report *gradient* concentric ring patterns formed from a capillary-held polymer solution in a confined geometry consisting of a spherical lens on a silicon surface (sphere-on-Si) as illustrated in Figure 1a and 1b. The concentration of the solution and the surface tension of solvent are found to exert profound influences on the center-to-center distance between adjacent rings (λ_{C-C}) and the height of the ring (h_d). Each ring is nanometers height and microns wide. Both λ_{C-C} and h_d decrease slowly with increasing proximity to the center of the sphere/Si contact (Figure 2-1). In other words, the patterns are *gradient* (Figure 1c). A theoretical calculation based on mass conservation of the solution is conducted for the first time to gain physical insight of the pattern formation and agrees well with the experimental observations.

Experimental

A linear conjugated polymer, poly[2-methoxy-5-(2-ethylhexyloxy)-1,4-phenylenevinylene] (MEH-PPV) (MW=50-300 kg/mole) was selected as nonvolatile solute. The choice of system was motivated by its numerous potential applications in the areas of LED, photovoltaic cells, thin-film transistors, and bio-sensors.[18, 19] An additional advantage of employing MEH-PPV is that it enables fluorescence imaging. Therefore we were able to confirm that no MEH-PPV was deposited between adjacent rings (Figure 2-1c). Two MEH-PPV toluene solutions were prepared at concentrations c 0.075 mg/ml and 0.05 mg/ml, respectively. The MEH-PPV benzene and chlorobenzene solutions were also prepared at the $c = 0.03$ mg/ml. A drop of 12 μL solution was loaded between spherical lens and Si surface. Subsequently, two surfaces were brought into contact with inchworm motor so that a capillary-held MEH-PPV solution (capillary bridge) was formed with evaporation rate highest at the edge of the drop (Figure 2-1a and 2-1b).[16, 17] Experiments were performed at room temperature inside a home-made chamber so that the evaporation rate of the solvent was *controlled* and temperature gradient was eliminated. The pattern formation was monitored *in situ* by optical microscopy (OM).
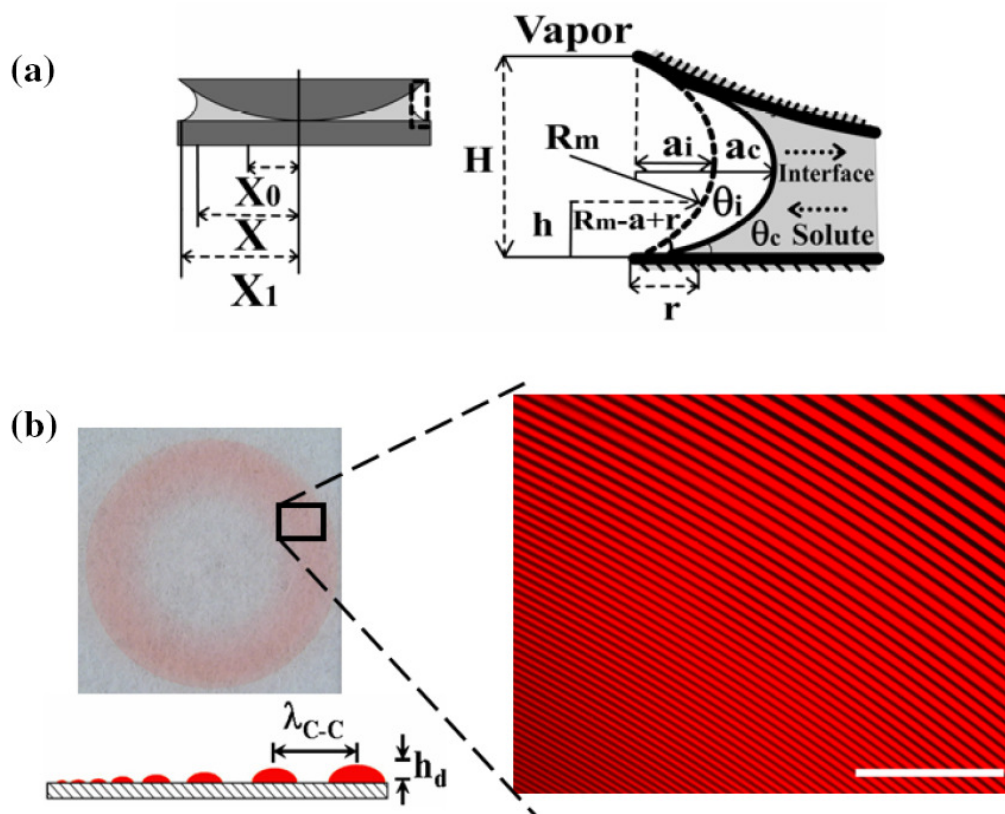
Figure 2-1. (color online). (a): Schematic cross-section of a capillary-held solution containing nonvolatile solute placed in a sphere-on-flat configuration. X_1, X, and X_0 are the radii of outermost, intermediate, and innermost rings from the center of sphere/flat contact, respectively. (b): The close-up of the capillary edge marked in (a). The parameters used in the calculation are illustrated. The solution front (i.e., liquid/vapor interface) moves inward while the transportation of solute is outward to pin the contact line. (c): The digital image of entire gradient concentric ring patterns formed by the deposition of the solute (i.e., MEH-PPV from 0.075 mg/ml toluene solution) in the geometry in (a). The diameter, d of outermost ring is 8500 μm. The image is faint due to small height of the rings (< 20 nm). In the right side a small zone of the fluorescent image of MEH-PPV ring patterns in red is shown. The scale bar is 200 μm. As the solution front moves inward, rings become smaller and height decreases as illustrated in lower left schematic.

Results and Discussion

The *in-situ* OM observation revealed that the contact line of the droplet moved in a controlled, repetitive stick-slip fashion (i.e., a competition between pining force and depinning force (capillary force))[11-13] toward the center of the sphere/Si contact with elapsed time (see the real-time lapse video in Supporting Information). A dark front (i.e., meniscus) was clearly evident at the capillary edge. The solution front (i.e., liquid/vapor interface) was arrested at spherical lens and Si surfaces for a certain period of time during which a MEH-PPV ring was formed. Then it jumped a short distance to next position where it was arrested again and a new ring was thus deposited. The jumping distance (λ_{C-C}) was found to decrease slowly with increasing proximity to the center of sphere/Si contact.

After the evaporation was complete, the two surfaces were separated and examined by OM and atomic force microscope (AFM). Highly ordered gradient concentric rings (both λ_{C-C} and width) were observed that span almost entire surfaces of both spherical lens and Si, except the region where the sphere was in contact with Si, as seen in the digital image (Figure 2-1c). Only the patterns on Si were evaluated. This is because the surface of the sphere is curved (the radius of curvature is 2 cm), which makes it hard to take images due to the curving effect from the sphere. The first AFM image (images are all 100 x 100 μm^2 in the measurements) was taken starting from the outermost ring. Efforts were made to ensure that the ring patterns are perpendicular to the scan direction. Then, the AFM tip was moved toward the sphere/Si contact center by exact 100 μm using the automated translational stage of the AFM. Subsequently, the second image was captured. The scans and movements were repeated until no rings can be imaged. Finally, the tip was moved to pass the contact center and reached the other end of the ring patterns so that the diameter, *d* of outmost ring can be obtained, which is found to be consistent with the value obtained using digital camera (In the present study, $d = 8500$ μm was found for the 0.075 mg/ml toluene solution (Figure 1c)). The data was then processed as follows. Each 100 x 100 μm^2 image was split into two 50 x 50

μm^2 scans from the center of the AFM image. The λ_{C-C} and the height of the ring, h_d were obtained after averaging from 5 cross sections of an AFM image (50 x 50 μm^2). The center-to-center distance of adjacent rings was measured as λ_{C-C}. The absolute position of the ring away from the sphere/Si contact center, i.e., X was also determined.

Figure 2-2 shows λ_{C-C} and h_d, obtained from dynamic self-assembly of two MEH-PPV toluene solutions at the different concentrations, as a function of X. As the c decreased from 0.075 to 0.05 mg/ml, both λ_{C-C} and h_d reduced. This can be qualitatively rationalized as follows. Compared to the case at $c = 0.075$ mg/ml, there were fewer MEH-PPV with which to create local surface roughness to pin the contact line at lower concentration ($c = 0.05$ mg/ml).[10, 20] The pinning time was, therefore, much shorter. In other words, the evaporative loss of toluene ΔV was less, which, in turn, caused the contact line to deposit less (i.e., smaller h_d and width as confirmed by AFM) and to hop less inward to next position (i.e., smaller λ_{C-C}). For example, at $X = 3775$ μm, for 0.05 mg/ml solution λ_{C-C} is 8.9 μm with 7.1 nm in height (Figure 2-2a and 2-2b). However, these values were much larger for $c = 0.075$ mg/ml ($\lambda_{C-C} = 12.8$ μm and $h_d = 11.4$ nm). Two representative 3D AFM height images and corresponding profiles, obtained from 0.075 mg/ml solution, are shown in Figure 2-2b as insets and Figure 2-2c, respectively. Both λ_{C-C} and h_d decreased from 11.5 μm and 9.5 nm at $X = 3725$ μm to 7.6 μm and 5.9 nm at $X = 3375$ μm as the evaporation front moved inward. For 0.075 mg/ml solution concentric rings are formed from 4250 μm (X_1) to 2625 μm (X_0), where X_1 and X_0 are the radii of outermost and innermost ring in the experiment, respectively. The values of $X_1 = 4250$ μm and $X_0 = 2825$ μm are found for 0.05 mg/ml solution. It should be noted that, to exclude the possible hydrodynamic instabilities caused when the sphere is brought in contact with the Si surface, the rings formed in the range from 4000 μm to 4250 μm at the early stage of the evaporation are not analyzed.
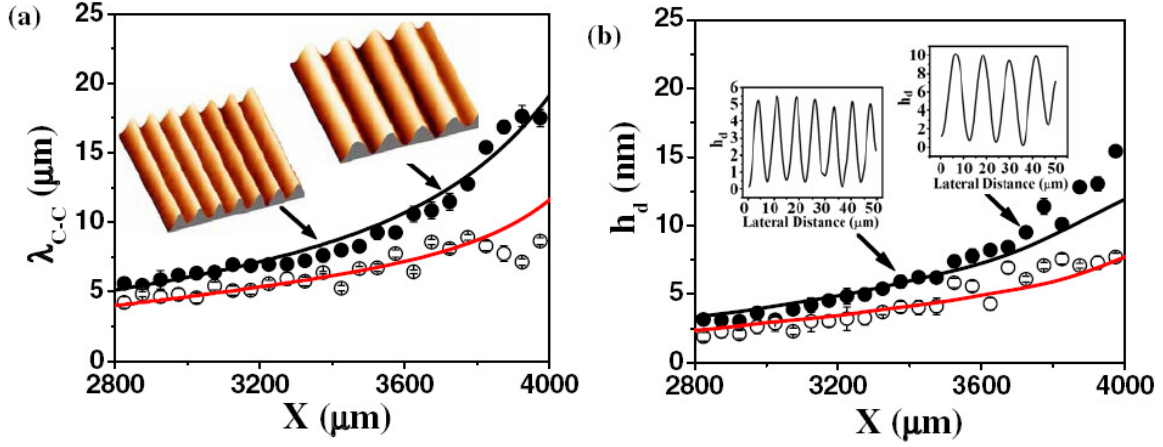
Figure 2-2. Concentration effect. (a) λC-C and (b) hd are plotted as a function of X at different concentrations (solid and open circles corresponding to the data obtained from toluene solutions at c = 0.075 mg/ml and 0.05 mg/ml, respectively). X is the distance away from the center of sphere/Si contact. Theoretical calculations (solid lines) based on mass conservation yield the initial and critical contact angles of θ_i = 180, θ_C = 15.60 for c = 0.075 mg/ml and θ_i = 180 and θ_C = 16.10 for c = 0.05 mg/ml, respectively. Two representative AFM 3D topographical images (50 x 50 µm2) obtained from the 0.075 mg/ml solution are given as insets. (c): The corresponding cross sections of AFM images shown in insets of (b).

The amount of volume loss of the solvent *ΔV* is governed by the competition between pinning force and capillary force. The pinning force is proportional to the total length of the contact line (~$2\pi X$ in Figure 1a),[20] which decreases linear in the course of stick-slip motion of the contact line. The capillary force $F_C = 16\pi\gamma_{lv}X\arctan\left(4aR/X^2\right)$, however, is nonlinear, where γ_{lv} is the surface tension of the solvent; *a* and *R* are the height of meniscus and the radius of curvature of the spherical lens, respectively (Figure 2-1b). The imbalance between linear pinning force and nonlinear capillary force resulted in a nonlinear *ΔV*. Consequently, the patterns were *gradient* rather than strictly repetitive.

To quantitatively uncover the nature of the formation of concentric rings exhibiting gradient in both λ_{C-C} and h_d, we performed a theoretical calculation based on the mass conservation during the course of the solvent evaporation. As toluene evaporates, MEH-PPV jams into the edge of the solution next to the contact line, preventing it from retracting (i.e., "stick"). The chemical property of deposited MEH-PPV is different from sphere and Si. The deposition (jamming) creates local surface roughness at sphere and Si surfaces. Both chemical inhomogeneities and surface roughness contribute the pinning of the contact line.[20] During the deposition of MEH-PPV the initial contact angle θ_i decreases gradually, owing to the evaporative volume loss of toluene ΔV, to a critical angle θ_C (Figure 2-1b) at which the capillary force becomes larger than the pinning force.[2, 3, 14, 15, 21] This leads the contact line to jump to a new position (i.e., "slip"). The ΔV during the formation of MEH-PPV ring (i.e., a changing from a_i to a_c) is given by

$$\Delta V = \pi X H \left\{ H \left[\arctan(\frac{2a_c}{H}) - \arctan(\frac{2a_i}{H}) \right] + (a_c - a_i) \right\} \tag{2-1}$$

where H is the surface separation at the liquid-vapor interface of the solution, a_i and a_c are the height of meniscus at contact angles θ_i and θ_C, respectively. The relation of θ and a can be established from the geometry of capillary edge defined in Figure 1b.

$$(\frac{H}{2} - h)^2 + (R_m - a + r)^2 = R_m^2 \tag{2-2}$$

$$\theta \approx \tan \theta = \frac{\partial h}{\partial r}\bigg|_{x=0} \approx \frac{H - 2a}{H} \tag{2-3}$$

where R_m is the radius of curve of the capillary edge ($H \approx 2R_m$), h is the local thickness of capillary edge at the position r, and $H \approx \frac{X^2}{2R}$. The volume of confined solution V_{Liq} (i.e., light gray area in Figure 2-1a and 2-1b) is

$$V_{Liq} = \pi X^2 H - \pi R H^2 - \pi X H^2 \arctan \frac{2a}{H} + \frac{\pi X H^2}{2} - \pi X a H \tag{2-4}$$

and $\quad V_{Liq}^{new} = V_{Liq} - \Delta V \tag{2-5}$

The initial contact angle θ_i is ~18^0, calculated from eq. (2-3) and (2-4) since the initial loading volume V_{Liq} and initial X (i.e., X_1) are known from the experiment. It agrees well with the value determined experimentally from the side view of the capillary edge using a digital camera.[22] Combining eqs. (2-1) and (2-3)-(2-5), the new position X_{new}, at which a contact line is arrested, can be identified by iterative calculation until a best fit (lines in Figure 2-2a) with experimental data (symbols in Figure 2-2a) is reached.[23] The calculated outermost $\lambda_{C-C} = X_1-X$ and subsequent $\lambda_{C-C} = X - X_{new}$ can thus be obtained.

In the lubrication approximation after considering the evaporation process, the evolution equation of the local thickness of capillary edge is given by[3, 12, 15]

$$\rho\frac{dh}{dt} = -\rho\frac{1}{r}\frac{d}{dr}(rhv) - J \tag{2-6}$$

where ρ is the density of the solvent ($\rho \approx 1$), J is the mass of solvent evaporating per unit area unit time and assumed to be a constant. The average velocity of the solute moving toward the capillary edge to pin the contact line as illustrated in Figure 1b can be obtained by the integration of eq (2-6) [24]

$$v(r,t) = \left[-\frac{r}{2\rho h}J + \frac{1}{h\rho r}\frac{\left(4J\arctan\frac{2a}{H}\right)\left(H^2 + 4a^2\right)}{\left(3H^2 + 4a^2\right)}Q \right] \tag{2-7}$$

When the time $t=r/v$ is smaller than the pinning time t_p, the solute is allowed to transport, deposit, and form a ring at the contact line with a height h_d (assuming that the cross section of the ring is a cylindrical ridge in 1D) can be calculated by,

$$h_d = \left[\frac{V_{deposit}}{2\pi X\left(\alpha - \cos\alpha\sin\alpha\right)} \right]^{\frac{1}{2}} (1 - \cos\alpha) \tag{2-8}$$

where α is the angle between the ring and the Si surface ($\alpha \approx 0.5^0$ estimated based on AFM image). $V_{deposit}$ is the volume of deposits formed during the pinning time and calculated by

$$V_{deposits} = \frac{c}{\rho_d}\int_0^r 2\pi Xh\,dr \tag{2-9}$$

where c is concentration of the solution, ρ_d is the density of the deposited solute ($\rho_d \approx$ 1). The solid lines in Figure 2-2 represent the calculated values of λ_{C-C} and h_d based on the mass conservation discussed above, yielding θ_C of 15.6^0 and 16.1^0 for MEH-PPV solutions at $c = 0.075$ mg/ml and $c = 0.05$ mg/ml, respectively. Good agreements between experimental data and theoretical fits are clearly evident. The pinning force is directly related to the surface roughness.[20] An increase in h_d during MEH-PPV deposition results in a decrease in θ_C.[3, 15, 20, 21] A smaller θ_C implies a longer the pinning time t_p, which, in turn, causes a greater volume loss ΔV during pinning. As a result, it leads to a larger pull-away of the contact line to reach initial contact angle θ_i at a new position. Thus, a larger λ_{C-C} was observed at $c = 0.075$ mg/ml as shown in Figure 2-2a.

Figure 2-3 illustrates quantitative differences on λ_{C-C} and h_d as different solvents, benzene and chlorobezene, were used. The concentration of both MEH-PPV solutions is 0.03 mg/ml. The T_b of benzene and chlorobenzene are 80 °C and 130 °C, respectively, which imply that benzene evaporates faster than chlorobenzene (i.e., faster evaporation rate J for benzene). Thus, larger volume loss ΔV is expected for MEH-PPV benzene solution to reach θ_C and hop to next position inward. Accordingly, a larger λ_{C-C} would result in as is evidenced in Figure 2-3a. For benzene solution ($X_1 = 4125$ µm and $X_0 = 3675$ µm were found in the experiment) the number of concentric rings formed are much fewer than that from chlorobenzene solution ($X_1 = 4275$ µm and $X_0 = 2925$ µm) as a result of faster evaporation of benzene. To render a meaningful comparison, only the data points in the region of 3700 ~ 4100 µm are presented in Figure 3. The ΔV is dominantly dictated by θ_i and θ_C (eqs. (2-1) and (2-3)). The fitting of experimental values of λ_{C-C} yield $\theta_i = 35^0$ and $\theta_C = 32^0$ for MEH-PPV benzene solution; and $\theta_i = 16^0$ and $\theta_C = 14^0$ for MEH-PPV cholobenzene solution. The larger difference between θ_i and θ_C for benzene solution ($\Delta\theta = 3^0$) signifies a greater ΔV, suggesting that more MEH-PPV are deposited, reflected as higher value of h_d observed in the

experiment (Figure 2-3b) and the solution front would retract at a bigger pace subsequently. Thus, larger $\lambda_{C\text{-}C}$ and h_d are obtained in the case of MEH-PPV benzene solution.
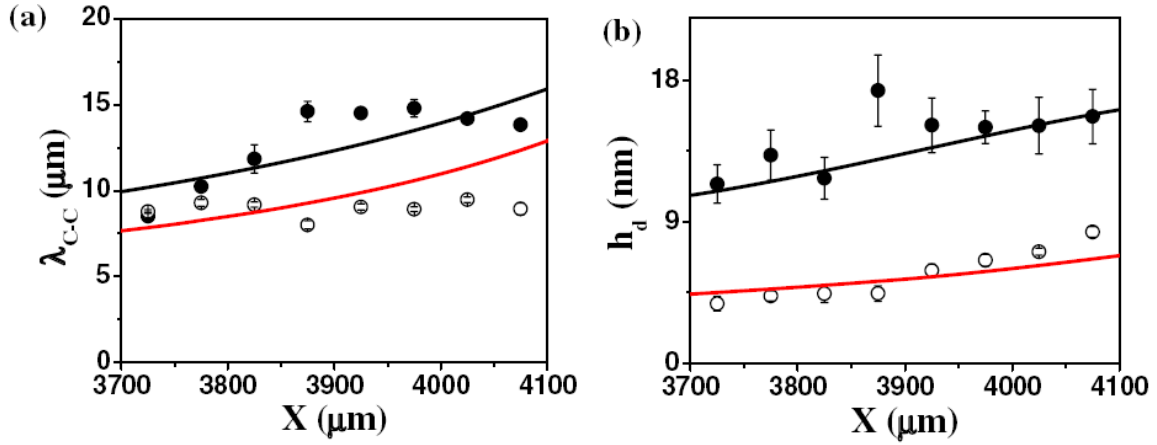
Figure 2-3. Solvent effect. (a) $\lambda_{C\text{-}C}$ and (b) h_d are plotted as a function of X with different solvents employed (solid and open circles are data from 0.03 mg/ml benzene and 0.03 mg/ml chlorobenzene solutions, respectively). The theoretical fittings yield the initial and critical contact angle of $\theta_i = 35^0$, $\theta_C = 32^0$ for benzene solution and $\theta_i = 16^0$, $\theta_C = 14^0$ for cholorbenzene solution, respectively.

It is noteworthy that the present symmetric confined geometry (i.e., a spherical lens on a Si surface) in a chamber facilitates the suppression of hydrodynamic instabilities and air convections. The evaporation is constrained to occur only at the capillary edge. As a consequence it provides a better *control* over the solvent evaporation. Thus, rather than a stochastic stick-slip motion that is seen in the case of an *unbound droplet* and responsible for the formation of irregular rings, *gradient* concentric rings with remarkable *regularity* are obtained in the present studies.

Conclusion

In conclusion, we showed that *gradient* concentric ring patterns of high regularity could form spontaneously, simply by allowing a droplet to evaporate in a consecutive stick-slip motion in a confined geometry. The use of solutions with different concentrations and different solvents effectively mediated the evaporative loss of the solvent and the deposition time of the solute, thereby affecting $\lambda_{C\text{-}C}$ and h_d. A simple theoretical calculation has, for the first time, been performed to reveal the nature of the formation of *gradient* ring patterns. The studies demonstrate that dynamic self-assembly in a confined geometry may offer a new means to produce *gradient* features, as well as a simple, versatile, generalizable approach to produce yet more complex patterns. This natural, pattern-forming process could find use in the fields such as nanotechnology and optoelectronics.

Acknowledgement

References

1   R.D. Deegan, O. Bakajin, T.F. Dupont et al. Capillary flow as the cause of ring stain from dried liquid drops. *Nature* **389**, 827 (1997).

2   R.D. Deegan Pattern formation in drying drops, *Physical Review E* **61,** 475 (2000).

3   R.D. Deegan, O. Bakajin, T.F. Dupont et al. Contact line deposits in an evaporating drop. *Physical Review E* **62**, 756 (2000).

4   O. Karthaus, L. Grasjo, N. Maruyama et al. Formation of ordered mesoscopic polymer arrays by dewetting. *Chaos* **9**, 308 (1999)

5   P.G. de Gennes. Solvent evaporation of spin cast films: "crust" effects. *European. Physics Journal E* **7**, 31 (2002)

6   E. Rabani, D.R. Reichman, P.L. Geissler et al. Drying-mediated self-assembly of nanoparticles. *Nature* **426**, 271 (2003).

7   H. Yabu and M. Shimomura Preparation of self-organized mesoscale polymer patterns on a solid substrate: continuous pattern formation from a receding meniscus. *Advanced Functional Materials* **15**, 575 (2005).

8   S.Q. Xu and E. Kumacheva Ordered morphologies in polymeric films produced by replication of convection patterns. *Journal of the American Chemical Society* **124**, 1142 (2002)

9   Z. Mitov and E. Kumacheva Convection-induced patterns in phase-separating polymeric fluids. *Physical Review Letters* **81**, 3427 (1998).

10   V.X. Nguyen and K.J. Stebe Patterning of small particles by a surfactant-enhanced Maragonia-Benard Instability. *Physical Review Letters* **88**, 164501 (2002).

11   E. Adachi, A.S. Dimitrov, and K. Nagayama Stripe patterns formed on a glass surface during droplet evaporation. *Langmuir* **11**, 1057 (1995).

12   M. Nonomura, R. Kobayashi, Y. Nishiura et al. Periodic precipitation during droplet evaporation on a substrate. *Journal of Physics Japan* **72**, 2468 (2003).

13   L. Shmuylovich, A. Q. Shen, and H. A. Stone Surface morphology of drying latex films: multiple ring formation. *Langmuir* **18**, 3441 (2002).

14   Y.O. Popov Evaporative deposition patterns: spatial dimensions of the deposit. *Physical Review E* **71**, 036313 (2005).

15   B. J. Fisher Particle convection in an evaporating colloidal droplet. *Langmuir* **18**, 60 (2002).

16   Z. Q. Lin and S. Granick Patterns formed by droplet evaporation from a restricted geometry. *Journal of the American Chemical Society* **127**, 2816 (2005).

17   S. W. Hong, J Xu, J. Xia et al. Drying mediated pattern formation in a capillary-held organometallic polymer solution. *Chemistry of Materials* **17**, 6223 (2005).

18   R.H. Friend, R. W. Gymer, A. B. Holmes et al. Electroluminiscence in conjugated polymers. *Nature* **397**, 121 (1999)

19   B. J Schwartz Conjugated polymers as molecular materials: How chain conformation and film morphology influence energy transfer and interchain interaction. *Annual Review of Physical Chemistry* **54**, 141 (2003).

20   P.G. de Gennes Wetting: statics and dynamics. *Review of Mordern Physics* **57**, 827 (1985).

21   Y.O. Popov and T. A. Witten Characteristic angles in the wetting of an angular region: deposit growth. *Physical Review E* **68**, 036306 (2003).

22.   The θi of MEH-PPV benzene and chlorobenzene solutions in the sphere-on-Si geometry are determined in the same way, from both experiment and calculation, yielding $\theta i = 35°$ and $16°$, respectively.

23.   Since X is experimentally measurable, ai (eq. (2-3)) and VLiq (eq. (2-4)) can be calculated given that θi is known. Similarly, ac and ΔV are calculated by substituting θC so that VLiqNew (eq. (2-5)) can be obtained. Equating eq. (2-4) and (2-5), the Xnew is thus yielded by iterative calculation until a best fit with experimental data is reached.

24. $$Q = \frac{A - B}{4\sqrt{(a-r)(H+r-a)}} \quad , \quad \text{where} \quad A = (r-a)(11aH - 10a^2 - H^2 + 8ar + Hr + 2r^2) \quad \text{and}$$

$$B = (H - 4a)^2 \sqrt{(a-r)(H+r-a)} \arctan\left[\frac{\sqrt{a-r}}{\sqrt{H+r-a}}\right]$$

CHAPTER 3. EVAPORATION-INDUCED SELF-ASSEMBLY OF NANOPARTICLES FROM A SPHERE-ON-FLAT GEOMETRY

Modified from a paper published in *Angewandte Chemie International Edition* **46**, 1860 (2007)

Jun Xu, Jianfeng Xia, and Zhiqun Lin*,

Introduction

Self-assembly of nanoscale materials to form ordered structures promises new opportunities for developing miniaturized electronic, optoelectronic, and magnetic devices.[1-4] In this regard, several elegant methods based on self-assembly have emerged,[5-8] for example, self-directed self-assembly,[5] and electrostatic self-assembly.[8] Self-assembly of nanoparticles by irreversible solvent evaporation has been recognized as an extremely simple route to intriguing structures.[9-12] However, these dissipative structures are often randomly organized without controlled regularity. Herein, we show a simple, one-step technique to produce concentric rings and spokes comprising quantum dots or gold nanoparticles with high fidelity and regularity by allowing a drop of a nanoparticle solution to evaporate in a sphere-on-flat geometry. The rings and spokes are nanometers high, submicrons to a few microns wide, and millimeters long. This technique, which dispenses with the need for lithography and external fields, is fast, cheap and robust. As such, it represents a powerful strategy for creating highly structured, multifunctional materials and devices.

Quantum dots (QDs) are highly emissive, spherical, inorganic nanoparticles a few nanometers in diameter. They provide a functional platform for a new class of materials for use in light emitting diodes (LEDs),[13] photovoltaic cells,[14] and biosensors.[15] Because of the

quantum-confined nature of QDs such as CdSe, the variation of particle size provides continuous and predictable changes in fluorescence emission. Passivating the vacancies and trap sites on the CdSe surface with higher-band-gap materials, such as ZnS, produces CdSe/ZnS core/shell QDs that have strong photoluminescence.[16] Two CdSe/ZnS core/shell QDs (4.4 and 5.5 nm in diameter, *D*) were used as the first nonvolatile solutes in our experiments. The surface of CdSe/ZnS was passivated with a monolayer of tri-n-octylphosphine oxide (TOPO) to impart solubility to the host environment and retain the spectroscopic properties of the materials by preventing them from aggregating. A drop of CdSe/ZnS in toluene was loaded in a confined geometry consisting of a spherical silica lens in contact with an Si substrate (i.e., sphere-on-flat geometry; see Experimental Section),[17-2`] which led to the formation of a capillary bridge of the solution as illustrated in Figure 3-1 a. In situ optical microscopy (OM) revealed two main types of pattern formations, namely, concentric rings and spokes, which depend on whether fingering instabilities of thin film of the evaporating front took place or not.

Results and Discussion

The formation of ringlike deposits in an evaporating drop that contains nonvolatile solutes on a single surface is known as the "coffee-ring" phenomenon.[9, 10, 22, 23] Maximum evaporative loss of the solvent at the perimeter triggers the jamming of the solutes and creates a local roughness (i.e., the contact line is pinned). This action leads to the transportation of solutes to the edge, thus forming a coffee-ring stain.[9, 10, 22, 23] The repeated "stick-slip" motions of the contact line produce concentric rings governed by the competition between the capillary force and the pinning force.[18] However, stochastic rings (irregular multirings) are generally formed on a single surface.[22, 23] In contrast, highly ordered concentric rings composed of 5.5 nm CdSe/ZnS QDs over a distance of hundreds of micrometers were created by drying a toluene solution of QDs (*c*=0.25 mg mL^{-1}) in a sphere-on-flat geometry (Figure 3-

1 b,c). This pattern is a direct consequence of the controlled, repetitive pinning and depinning cycles of the contact line (Figure 3-1 b), which resembles our recent findings on the self-assembly of polymeric materials.[17, 18, 24] According to in situ OM observation, it took about 7 s for a ring to deposit (stick); a 0.5 s "slip" followed. Thus, the solution front speed was estimated to be: $v=9$ μm s^{-1} (slip over a distance of 4.7 μm in 0.5 s). Locally, the concentric rings appeared as parallel stripes. The center-to-center distance between the adjacent rings, λ_{c-c}, and the width of the ring, w, were 4.7 μm and 2.2 μm, respectively, as determined by fast Fourier transformation of AFM and SEM images. The average height of the rings measured by AFM was 13.2 nm. The observations of QD rings with remarkable regularity highlight the significance of using a sphere-on-Si geometry, which is extremely easy to implement, to guide solvent evaporation and control capillary flow in a drying drop.

Figures 3-1 d and e show that an array of periodic rings of QDs was also obtained at lower solution concentrations ($c=0.15$ mg mL^{-1} in Figure 1 d and 0.05 mg mL^{-1} in Figure 3-1 e). The ring patterns in Figures 1 c-e reveal a noteworthy influence of the concentration on the resulting dimension of the QDs. For the 5.5 nm QD toluene solution, the ring width, w, decreased from 2.2 μm at $c=0.25$ mg mL^{-1} (Figure 1 c) to 1.5 μm at $c=0.15$ mg mL^{-1} (Figure 1 d), and to 630 nm at $c=0.05$ mg mL^{-1} (Figure 1 e). It should be noted that these submicron-wide rings (630 nm) were, for the first time, obtained by solvent evaporation in a sphere-on-flat geometry.[17, 18] A similar trend was seen in λ_{c-c}, which decreased from 4.7 μm at $c=0.25$ mg mL^{-1} to 4.0 μm at $c=0.15$ mg mL^{-1}, and to 2.9 μm at $c=0.05$ mg mL^{-1} (Figure 1 c-e). The average height of rings, h, was 6.9 nm and 5.5 nm at $c=0.15$ and 0.05 mg mL^{-1}, respectively. A larger value of h implies a longer pinning time of QDs at the three-phase contact line, which, in turn, causes a larger w and a greater evaporation volume loss of toluene during pinning.[18] As a result, there is a larger pull on the contact line to a new position. Thus, a larger λ_{c-c} was observed at a higher concentration of the solution.[18, 23, 25] It is noteworthy that constant values of λ_{c-c} and w were observed at a given concentration. This

consistency can be attributed to the uniform h of QDs deposited on the substrates, which suggests a constant pinning time. Thus, the evaporative loss of solvent was steady and led to the formation of concentric rings with constant λ_{c-c} and w.
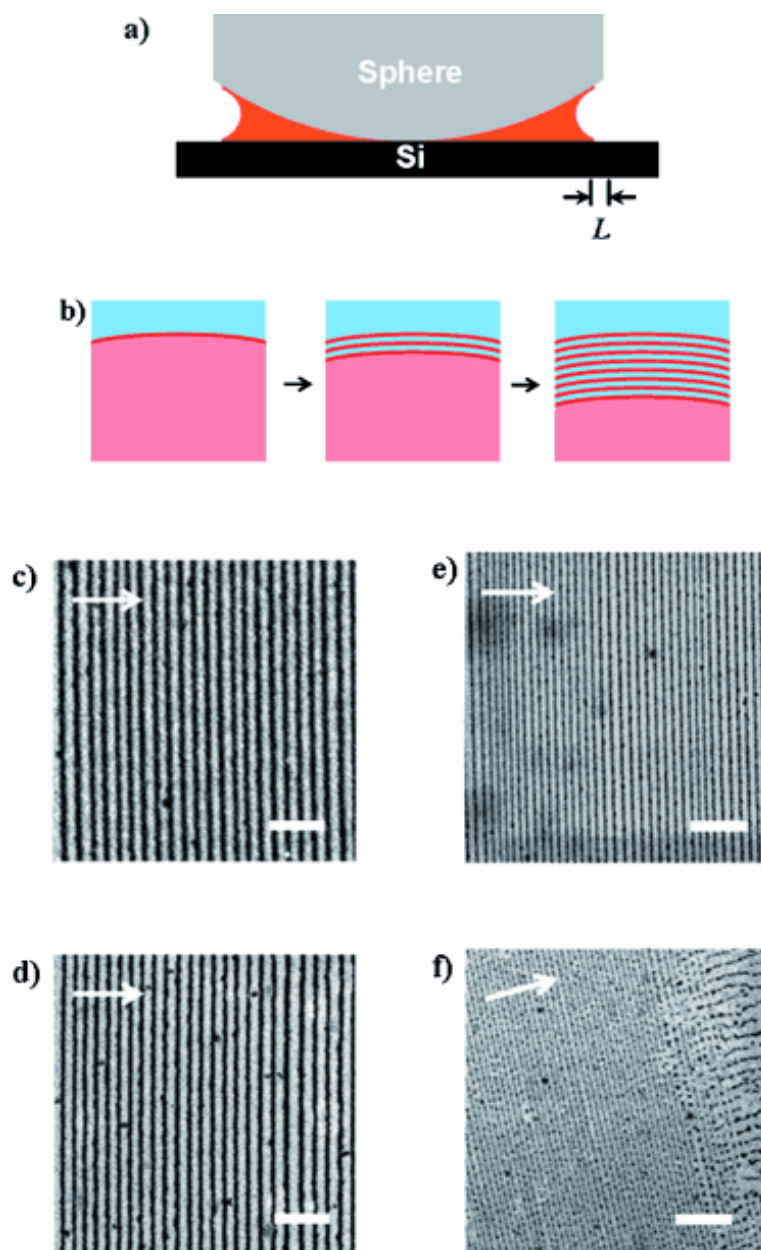
Figure 3-1. a) Sphere-on-flat geometry in which a drop of nanoparticle solution is constrained, thus bridging the gap between the spherical lens and Si substrate. b) Stepwise

representation of the formation of concentric rings, which propagate from the capillary edge of the drop towards the center of the sphere/Si contact. c-f) SEM images of concentric rings produced by evaporation-induced self-assembly of 5.5-nm CdSe/ZnS QDs formed by drying 0.25 mg mL^{-1} (c), 0.15 mg mL^{-1} (d), and 0.05 mg mL^{-1} (e and f) toluene solutions. A transition from rings to wirelike structures (c=0.05 mg mL^{-1}) is shown on the right side of panel (f). The scale bar is 20 μm in (c-e) and 30 μm in (f). The white arrow on the upper left marks the direction of the movement of the solution front.

Note that at a late stage of drying, all three 5.5-nm CdSe/ZnS QD toluene solutions (c=0.25, 0.15, and 0.05 mg mL^{-1}) in which the solution front was very close to the center of the sphere/Si contact, exhibited a transition from concentric rings to radially aligned wirelike patterns (see top right in Figure 1 f). This change can be rationalized as follows: the velocity of the displacement of the meniscus, v (i.e., the solution front in Figure 3-1 a), in a capillary bridge is inversely proportional to the distance from the capillary entrance to the meniscus, L (i.e., $v \approx 1/L$);[26] v decreases as the meniscus moves inward as a result of an increase in L (Figure 1 a). It has been numerically demonstrated that the formation of fingering instability in an evaporating film is dictated by v: a faster v stabilizes the front, whereas a slower v leads to the development of fingering instabilities at a propagating front.[27] In this study, as the solution front retracted, the evaporation rate of the solvent decreased, which caused a reduction in v. As a consequence, the concentration and the viscosity of the solution at the meniscus decreased, which led to instabilities.[27]

A fluorescence microscopic image of concentric rings obtained from self-assembling 5.5-nm CdSe/ZnS QDs after toluene evaporation (c=0.15 mg mL^{-1}) is shown in Figure 3-2 as an inset. The fluorescence intensity (Figure 3-2) oscillates almost evenly over a 50 μm scanning distance (arrow in the inset), thus signifying that the rings have uniform height and width. A periodic spacing between rings is also clearly evident. The ability to deposit

fluorescent nanoparticles with well-defined dimensions in the concentric-ring mode presented herein may open a very simple route to manipulating linear micron-to-submicron wires of semiconductors into a ring structure for use in ring resonator lasers.[28]
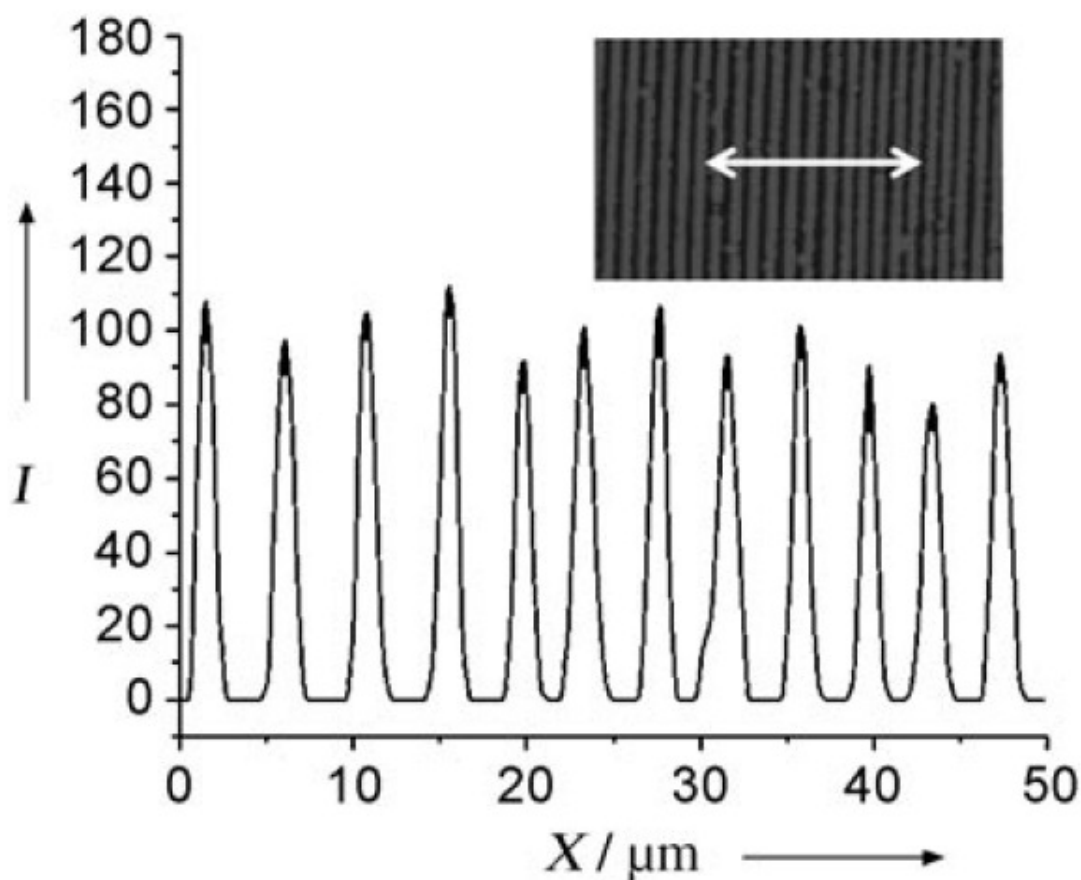
Figure 3-2. Scan of fluorescence intensity along the arrow indicated in the fluorescence microscopic image (inset, converted into gray scale) of CdSe/ZnS rings. The rings were produced by self-assembly of 5.5-nm CdSe/ZnS QDs after toluene evaporation from a 0.15 mg mL^{-1} solution.

It should be noted that a film with chaotic structures was observed from a control sample in which the QD toluene solution (V=12 μL, c=0.25 mg mL^{-1}, D=5.5 nm) was allowed to evaporate on a silicon substrate with or without a cover for preventing possible

convections (see Supporting Information). This observation justified the necessity of employing the sphere-on-flat configuration to control the evaporation process and associated capillary flow. In a second control experiment, an extra amount of coordinating ligand, TOPO, was added to the QD solutions. Irregular, discontinuing patterns were seen (see Supporting Information). Therefore, to obtain well-ordered rings, the excessive TOPO was removed to leave only TOPO-covered nanoparticles that were used in the experiments.

Instead of concentric rings as seen parallel to the three-phase contact line at the early stage of the solvent evaporation when the 5.5-nm CdSe/ZnS QDs were used (Figures 1 and 2), spokes were produced exclusively throughout the entire drying process when a smaller CdSe/ZnS QD (D=4.4 nm) was used. The speed of the solution front, which moved in a continuous manner, was v=1 μm s^{-1} during the formation of spokes, as evaluated by in situ OM observation. The dynamic formation of spokes is attributed to the fingering instabilities of the evaporating front,[6, 7, 27, 29-31] as illustrated in Figure 3-3 a. At an early stage of the drying process, the fingers form at the three-phase contact line (first panel in Figure 3-3 a). They serve as nucleation sites and grow into stripes locally that orient normal to the evaporating front by transporting the QDs from the surrounding solution (second panel in Figure 3-3 a) as they propagate inward. This process results in spoke patterns (last panel in Figure 3-3 a).[7] The process is analogous to the molecular combing of DNA chains, in which DNA chains are aligned perpendicular to the contact line of a drying drop.[32] Figure 3-3 b shows a typical fluorescence microscopic image of a dried film comprising 4.4-nm CdSe/ZnS QDs. Each stripe in the spoke was 22 nm high, 1.8 μm wide, and millimeters long. The distance between adjacent stripes, λ_f, was 5 μm. The movement of the solution front with 4.4-nm QDs (v=1 μm s^{-1}) was much slower than that with 5.5-nm QDs (v=9 μm s^{-1} per slip) at the same concentration (c=0.25 mg mL^{-1}). The smaller v facilitated the formation of fingering instability at the solution front.[27] Thus, spokes were formed with 4.4-nm QDs, while rings were produced with 5.5-nm QDs.
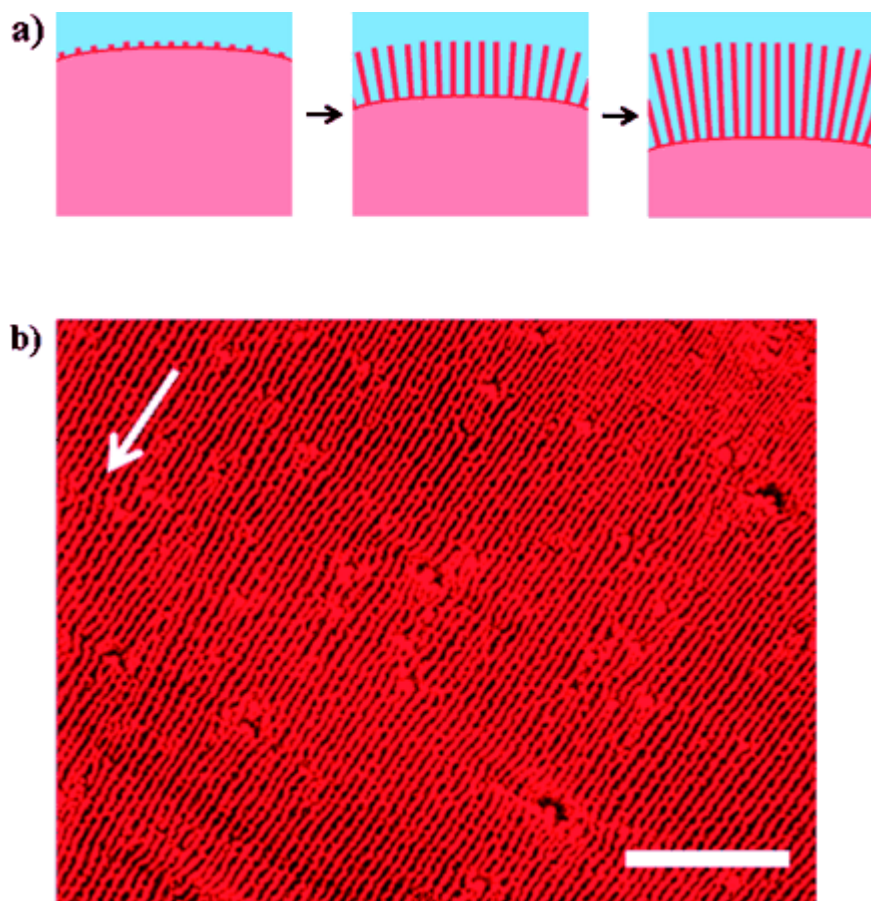
Figure 3-3. a) Formation of spoke patterns upon evaporation from the capillary bridge in the sphere-on-flat geometry. b) Optical micrograph showing the spokes formed by drying 4.4-nm CdSe/ZnS toluene solution (c=0.25 mg mL^{-1}). The scale bar is 100 μm. The arrow on the upper left indicates the direction of the movement of the solution front.

To further demonstrate that a wide variety of nanoparticles can be used to produce regular patterns in the sphere-on-flat geometry, CdTe nanorods (7 nm in diameter and 20 nm in length) and Au nanoparticles (6 nm in diameter) were also employed (see Experimental Section). Concentric ring patterns consisting of CdTe nanorods and Au nanoparticles (see Supporting Information) were observed. We note that the CdTe nanorods and Au nanoparticles were larger than the CdSe/ZnS QDs. Larger surface roughness and a stronger pinning force are expected with larger nanoparticles. Therefore, rather than spokes, the

concentric rings dominate exclusively in CdTe and Au nanoparticles despite the fact that the nanoparticles used in our studies (CdSe/ZnS, CdTe, and Au) were all passivated with the same ligand, TOPO.

Conclusion

In summary, we have demonstrated that constrained evaporation (i.e., drying in a confined, axial symmetric geometry to provide control over the solvent evaporation and the associated capillary flow) can be utilized as a simple, cheap, and robust strategy for self-assembling various nanoparticles with easily tailored optical and electronic properties into spatially ordered, two-dimensional patterns of a single layer or several layers of particle thickness on the micrometer-to-submicron scale. These self-organized patterns of functional nanoscale materials over large areas offer a tremendous potential for applications in optoelectronic devices, LEDs, solar cells, and biosensors.

Experimental

Materials: Two kinds of TOPO-functionalized CdSe/ZnS core/shell QDs[16] were prepared in accordance with previous reports.[33] The diameters of the QDs were 4.4 and 5.5 nm as determined by TEM, which correspond to the growth of two-to-three atomic layers of ZnS, provided that the original CdSe are 3.0 and 4.0 nm in diameter. The 4.4-nm QDs were orange-emitting with the maximum emission, λ_{max}, at 598 nm. The 5.5-nm QDs were red-emitting with λ_{max} at 632 nm. The QDs were purified twice by using antisolvent precipitation from the reaction mixture in chloroform, thus removing excessive TOPO ligand. They were subsequently vacuum-dried and dissolved in toluene to make a stock solution (1 mg mL^{-1}). Finally, QD toluene solutions at different concentrations (0.25, 0.15, and 0.05 mg mL^{-1} for the 5.5-nm QDs) were prepared by diluting the filtered stock solution (syringe filter with 200 nm pore size). TOPO-covered CdTe short nanorods (7 nm in diameter

and 20 nm in length; Supporting Information) and TOPO-covered Au nanoparticles (6 nm in diameter) were also synthesized and purified in accordance with previous reports.[33, 34]

Pattern formation in the sphere-on-flat geometry: A drop of a solution of nanoparticles in toluene (12 μL; CdSe/ZnS QDs, CdTe nanorods or Au nanoparticles) was loaded in a small gap between a spherical silica lens and a SiO_2-coated Si wafer (thermally coated 300 nm thick SiO_2 on Si). The sphere and Si wafer were firmly fixed at the top and bottom, respectively, of a sample holder inside a sealed chamber. The temperature inside the chamber was rigorously monitored and was constant during the experiment. The two surfaces (sphere and Si wafer) were brought into contact, thus forming a capillary bridge of the solution.[17, 18] The diameter and radius of curvature of the sphere were 1 cm and 2 cm, respectively. In such sphere-on-flat geometry, evaporation occurred only at the capillary edge. It took approximately 30 min for the evaporation to be complete. Finally, the two surfaces were separated and the patterns on the Si wafer were examined.

Characterization: In situ optical microscopy (Olympus BX51) was performed in reflective mode under bright light. AFM imaging of patterns on an Si surface was obtained by using a scanning force microscope (Digital Instruments Dimension 3100) in tapping mode. SEM studies were performed on a Hitachi S-4000 field-emission scanning electron microscope operating at 10 kV accelerating voltage. TEM studies were performed on a JEOL 1200EX scanning/transmission electron microscope operating at 80 kV.

Supporting Information
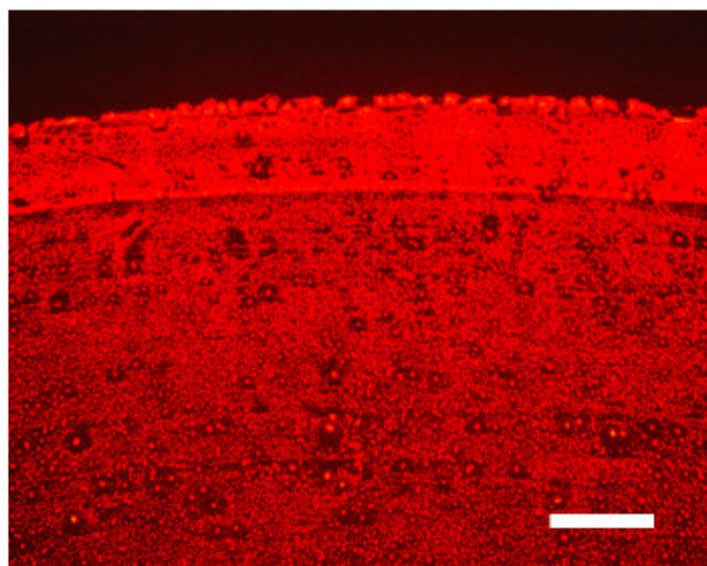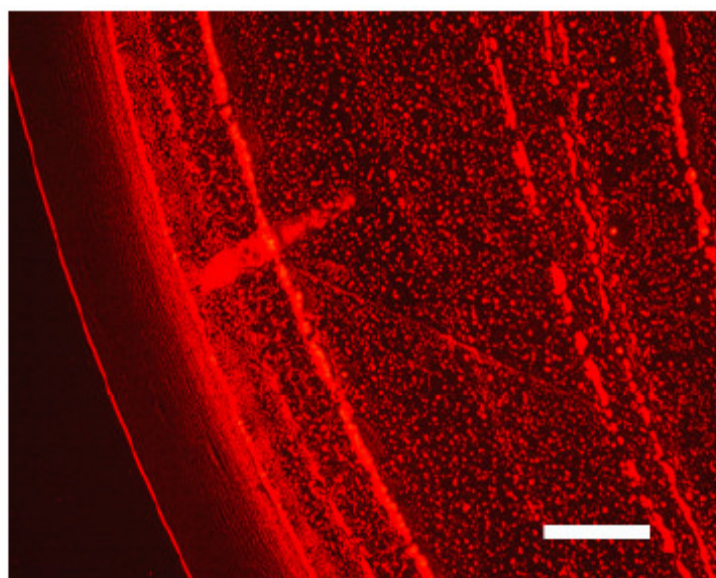
Figure 3-4. Optical micrographs of control experiments: a film formed by allowing the 0.25 mg ml^{-1} CdSe/ZnS toluene solution (D = 5.5 nm) to evaporate on a *single surface*(i.e., a Si substrate only) with a cover **(a)** and without a cover **(b)**. Scale bar = 100 μm.
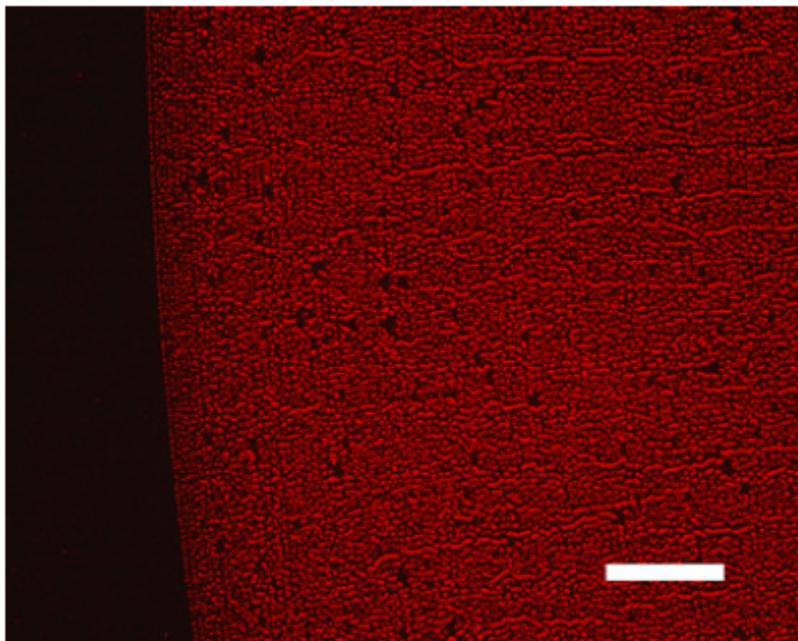
Figure 3-5. Optical micrograph of a drying film obtained from 0.1 mg ml^{-1} TOPO functionalized CdSe/ZnS toluene solution (D = 5.5 nm) mixed with excessive 0.8 mg ml^{-1} TOPO, allowed to evaporate in the sphere-on-Si geometry. Scale bar = 100 μm.
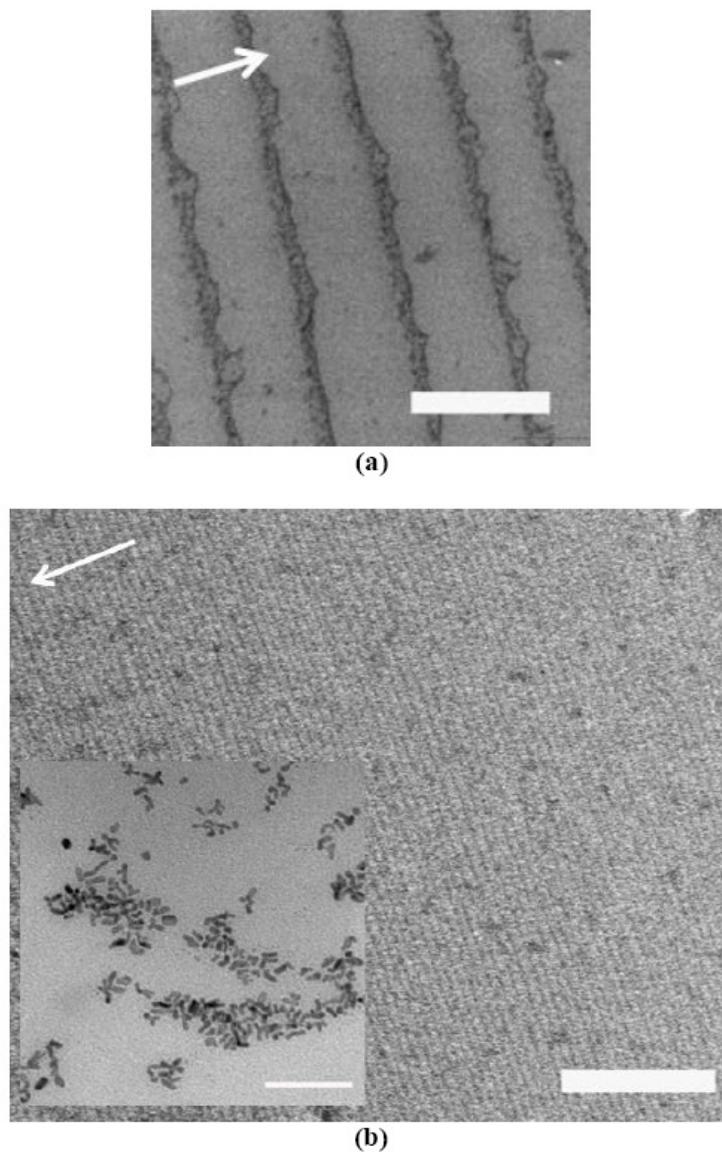
Figure 3-6. SEM images of ring patterns produced from the drying of the 0.5 mg ml^{-1} CdTe nanaorod toluene solution in the sphere-on-flat geometry. λ_{C-C} = 4 μm, w = 1.5 μm, and h = 29.2 nm. **(a)** stripes appearance locally, **(b)** a large view of the rings (*Inset:* TEM image of the CdTe nanorods prepared by drop-casting the CdTe toluene solution on Cu grid (i.e., on single surface). Scale bar = 100 nm). The scale bars are 5 μm in (a) and 50 μm in (b). The arrow denotes the direction of the motion of the solution front.
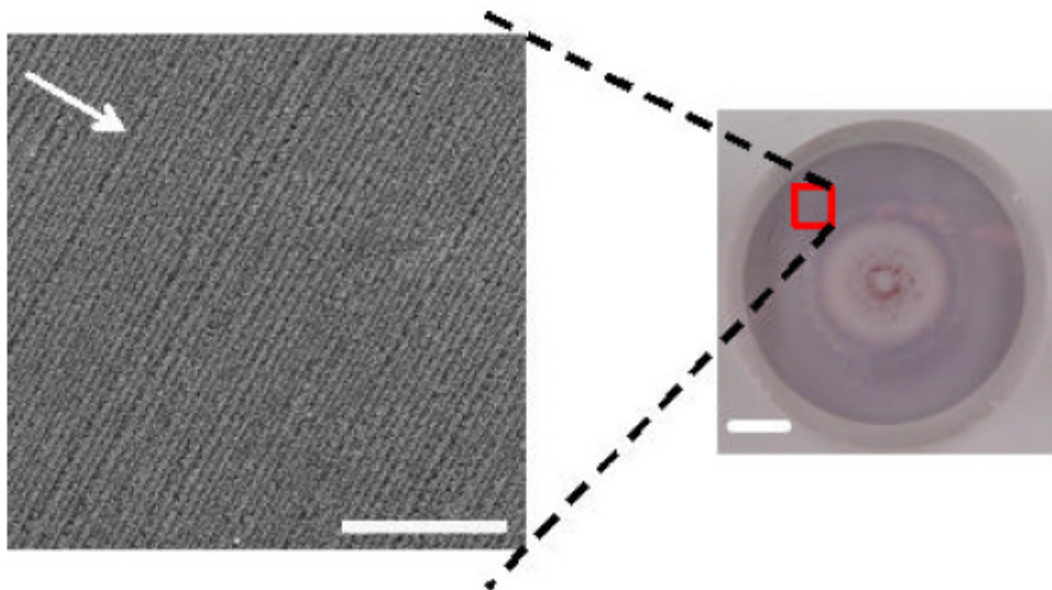
Figure 3-7. *Right:* Digital image of entire concentric ring patterns of Au nanoparticles on the spherical lens formed by the deposition of nanoparticles from the 0.5 mg ml-1 toluene solution in the sphere-on-Si geometry. Scale bar = 2 mm. λ_{C-C} = 2.5 μm, w = 1 μm, h = 55 nm. *Left:* The close-up of the red squared region marked on the right panel. Scale bar = 50 μm. The arrow indicates the direction of the motion of the solution front.

Acknowledgement

References

1. G. M. Whitesides, B. Grzybowski, Self-assembly at all scales. *Science* **295**, 2418-2421 (2002).

2. T. Thurn-Albrecht, J. Schotter, C. A. Kastle, N. Emley, T. Shibauchi, L. Krusin-Elbaum, K. Guarini, B. C. T. , M. T. Tuominen, T. P. Russell, Ultrahigh-density nanowire arrays grown in self-assembled diblock copolymer templates. *Science* **290**, 2126-2129 (2000).

3. V. V. Tsukruk, H. Ko, S. Peleshanko, Nanotube surface arrays: Weaving, bending, and assembling on patterned silicon. *Physical Review Letters* **92**, 065502 (2004).

4. H. Ko, V. V. Tsukruk, Liquid-crystalline processing of highly oriented carbon nanotube arrays for thin-film transistors. *Nano Letters* **6**, 1443 (2006).

5. Y. Lin, A. Boker, J. He, K. Sill, H. Xiang, C. Abetz, X. Li, J. Wang, T. Emrick, S. Long, Q. Wang, A. Balazs, T. P. Russell, Self-directed self-assembly of nanoparticle/copolymer mixtures. *Nature* **434**, 55-59 (2005).

6. M. Gleiche, L. F. Chi, H. Fuchs, Nanoscopic channel lattices with controlled anisotropic wetting. *Nature* **403**, 173-175 (2000).

7. J. Huang, F. Kim, A. R. Tao, S. Connor, P. D. Yang, Spontaneous formation of nanoparticle stripe patterns through dewetting. *Nature Materials* **4**, 896-900 (2005).

8. A. M. Kalsin, M. Fialkowski, M. Paszewski, S. K. Smoukov, K. J. M. Bishop, B. A. Grzybowski, Electrostatic self-assembly of binary nanoparticle crystals with a diamond-like lattice. *Science* **312**, 420-424 (2006).

9. R. D. Deegan, O. Bakajin, T. F. Dupont, G. Huber, S. R. Nagel, T. A. Witten, Capillary flow as the cause of ring stain from dried liquid drops. *Nature* **389**, 827-829 (1997).

10. R. D. Deegan, O. Bakajin, T. F. Dupont, G. Huber, S. R. Nagel, T. A. Witten, Contact line deposits in an evaporating drop. *Physical Review E* **62**, 756-765 (2000).

11. E. Rabani, D. R. Reichman, P. L. Geissler, L. E. Brus, Drying-mediated self-assembly of nanoparticles. *Nature* **426**, 271-274 (2003).

12. T. P. Bigioni, X. M. Lin, T. T. Nguyen, E. I. Corwin, T. A. Witten, H. M. Jaeger, Kinetically driven self assembly of highly ordered nanoparticle monolayers. *Nature Materials* **5**, 265-270 (2006).

13. V. L. Colvin, M. C. Schlamp, A. P. Alivisatos, Light-emitting diodes made from cadmium selenide nanocrystals and a semiconducting polymer. *Nature* **370**, 354-357 (1994).

14. W. U. Huynh, J. J. Dittmer, A. P. Alivisatos, Hybrid nanorod-polymer solar cells. *Science* **295**, 2425-2427 (2002).

15. I. L. Medintz, H. T. Uyeda, E. R. Goldman, H. Mattoussi, Quantum dot bioconjugates for imaging, labelling and sensing. *Nature Materials* **4**, 435-446 (2005).

16. J. Xu, J. Xia, J. Wang, J. Shinar, Z. Q. Lin, Quantum dots confined in nanoporous alumina membranes. *Applied Physics Letters* **89**, 133110 (2006).

17. S. W. Hong, J. Xu, J. Xia, Z. Q. Lin, F. Qiu, Y. L. Yang, Drying mediated pattern formation in a capillary-held oganometallic polymer solution. *Chemistry of Materials* **17**, 6223-6226 (2005).

18. J. Xu, J. Xia, S. W. Hong, Z. Q. Lin, F. Qiu, Y. L. Yang, Self-assembly of gradient concentric rings via solvent evaporation from a capillary bridge. *Physical Review Letters* **96**, 066104 (2006).

19. S. W. Hong, J. Xu, Z. Q. Lin, Template-assisted formation of gradient concentric gold rings. *Nano Letters* **6**, 2949 (2006).

20. S. W. Hong, S. Giri, V. S. Y. Lin, Z. Q. Lin, Simple route to gradient concentric metal and metal oxide rings. *Chemistry of Materials* **18**, 5164 (2006).

21. S. W. Hong, J. Xia, Z. Q. Lin, Spontaneous formation of mesoscale polymer patterns in an evaporating bound solution Advanced Materials **19**(10), 1413 (2007).

22. E. Adachi, A. S. Dimitrov, K. Nagayama, Stripe patterns formed on a glass surface during droplet evaporation. *Langmuir* **11**, 1057-1060 (1995).

23. L. Shmuylovich, A. Q. Shen, H. A. Stone, Surface morphology of drying latex films: multiple ring formation. *Langmuir* **18**, 3441-3445 (2002).

24. Z. Q. Lin, S. Granick, Patterns formed by droplet evaporation from a restricted geometry. *Journal of the American Chemical Society* **127**, 2816-2817 (2005).

25. N. D. Denkov, D. Velev, P. A. Kralchevsky, I. B. Ivanov, H. Yoshimura, K. Nagayamat, Mechanism of formation of two-dimensional crystals from latex particles on substrates. *Langmuir* **8**, 3183-3190 (1992).

26.   N. V. Churaev, *Liquid and Vapor Flows in Porous Bodies. Surface Phenomena*, Vol. 13, Gordon and Breach, University of Salford, 2000.

27.   A. V. Lyushnin, A. A. Golovin, L. M. Pismen, Fingering instability of thin evaporating liquid films. *Physical Review E* **65**, 021602 (2002).

28.   P. J. Pauzauskie, D. J. Sirbuly, P. D. Yang, Semiconductor nanowire ring resonator laser. *Physical Review Letters* **96**, 143903 (2006).

29.   A. M. Cazabat, F. Heslot, S. M. Troian, P. Carles, Fingering instability of thin spreading film driven by temperature gradient. *Nature* **346**, 824-826 (1990).

30.   O. Karthaus, L. Grasjo, N. Maruyama, M. Shimomura, Formation of ordered mesoscopic polymer arrays by dewetting. *Chaos* **9**, 308-314 (1999).

31.   I. Leizerson, S. G. Lipson, A. V. Lyushnin, Langmuir **20**, 291 (2004).

32.   X. Michalet, R. Ekong, F. Fougerousse, S. Rousseaux, C. Schurra, N. Hornigold, M. van Slegtenhorst, J. Wolfe, S. Povey, J. S. Beckmann, A. Bensimon, Dynamic molecular combing: stretching the whole human genome for high-resolution studies. *Science* **277**, 1518-1523 (1997).

33.   X. Peng, L. Manna, W. D. Yang, J. Wickham, E. Scher, C. Kadavanich, A. P. Alivisatos, Shape control of CdSe nanocrystals. *Nature* **404**, 59-61 (2000).

34.   M. Green, P. O'Brian, A simple one phase preparation of originically capped gold nanocrystals. *Chemical Communications*, 183-184 (2000).

CHAPTER 4. QUANTUM DOTS CONFINED IN NANOPOROUS ALUMINA MEMBRANES

Jun Xu, Jianfeng Xia, Jun Wang, Joseph Shinar and Zhiqun Lin*,

Abstract

CdSe/ZnS core/shell quantum dots (QDs) were filled into porous alumina membranes (PAMs) by dip coating. The deposition of QDs induced changes in the refractive index of the PAMs. The amount of absorbed QDs was quantified by fitting the reflection and transmission spectra observed experimentally with one side open and freestanding (i.e., with two sides open) PAMs employed, respectively. The fluorescence of the QDs was found to be retained within the cylindrical nanopores of the PAMs.

Introduction

Porous alumina membrane (PAM) fabricated by two-step anodic oxidation of aluminum (Al) consists of highly ordered hexagonal arrays of straight, cylindrical nanopores.[1] Although PAM was extensively used as a template to synthesize one-dimensional nanostructures with functional electronic characteristics, e.g. nanowires,[2] it has only recently been employed to control optical properties of colloid particles[3] and conjugated polymers[4] and to detect biomolecular binding[5] by monitoring the absorption, emission and reflectivity spectra. The large surface area of the PAM associated with the nanoporous structure facilitates a substantial change in refractive index upon the deposition of the molecules.

Quantum dots (QDs) are highly emissive, spherical nanoparticles with a few nanometers in diameter. They provide a functional platform for a class of materials for use in light emitting diodes (LEDs),[6] photovoltaic cells,[7] and bio-sensors.[8] Due to the quantum-confined nature of QDs such as cadmium selenide (CdSe), the variation of particle size provides continuous and predictable changes in fluorescence emission. By passivating most of the vacancies and trap sites on the CdSe surface with a higher band gap material such as zinc sulfide (ZnS), the resulting CdSe/ZnS core/shell QD possesses a stronger photoluminescence (PL), which is particularly important for use in biological applications.[8] Precise control over the dispersion and lateral distribution of the QDs within nanoscopic porous media provides a unique route to manipulate the optical and/or electronic properties of QDs in a very simple and controllable manner for the applications related to light emitting, optoelectronic, and sensor devices. To date, a few elegant studies have been demonstrated to disperse QDs, rather than fabricate one-dimensional nanowires of the QDs, in diblock copolymer templates via capillary force assisted deposition[9] or electrophoretic depostion.[10] However, the amount of QDs within diblock copolymer templates was not readily obtained.

Here, we study the optical properties of CdSe/ZnS core/shell QDs by directly depositing them in the host material, PAM through dip-coating. The amount of deposited QDs is quantified by modeling the change in reflection and transmission spectra of the PAMs when one side is open and when it is freestanding (i.e., both sides are open). Filling the PAM with QDs modulates the dielectric environment of the PAM, which in turn causes shifts in spectra; the fluorescence of the QDs in PAM is retained. Such directed deposition of QDs within an array of well-ordered PAM nanopores would offer a significant advance in

controlling the lateral distribution and spacing of QDs, and thus open up an avenue to manipulate optoelectronic properties of QDs in a very simple and controllable manner and to explore the feasibility of utilizing QD/PAM nanocomposites for sensors application.

Experimental

Two types of PAMs, produced by using a two-step anodization of 99.999% pure Al foil in 0.3M oxalic acid at 42 V at 0°C for 2.5 hrs,[1] were used in the study. The first type was the one-side-open membrane obtained right after the second anodization. The remaining Al at the bottom of the membrane served as a reflective layer for reflection spectrum measurements. The second was a freestanding membrane (i.e., two-side-open) fabricated by removing the remaining Al in saturated copper chloride ($CuCl_2$) solution and performing the barrier layer removal in 5wt% phosphoric acid at 30°C for 1 hr. The PAMs were thoroughly rinsed with deionized water, acetone and alcohol, and dried.

Two tri-n-octylphosphine oxide (TOPO) functionalized core/shell CdSe/ZnS QDs were prepared according to the well-established procedure.[11] The diameters of the QDs are 4.4 nm and 5.5 nm, respectively, as determined by TEM (data not shown), corresponding to the growth of two to three atomic layers of ZnS[12], given the original CdSe diameters of 3.0 nm and 4.0 nm, respectively. The 4.4 nm QDs are orange emitting with maximum emission, λ_{max}, at 598 nm.; the 5.5 nm QDs are red emitting with λ_{max} at 632 nm.

The deposition of QDs was driven by the capillary force.[9] The PAMs were dipped into 0.5 mg/ml QD chloroform solutions for several seconds and slowly withdrawn normal to the solution surface, and then dried in air for several minutes so that the QDs were trapped

within the cylindrical nanopores of the PAMs. Finally, the PAMs were immersed into fresh chloroform for ten times to exhaustively rinse off the possible QDs at the PAM surface, and the washed QD-loaded PAMs were dried in air prior to the subsequent characterizations of optical properties.

Results and Discussion

Figures 4-1a and 4-1b show surface and cross-sectional scanning electron microscopy (SEM) images of a freestanding blank (i.e., unfilled with QDs) PAM. The cross-sectional SEM image confirms a hexagonal array of nanoscopic porous structures with a high aspect ratio. The cylindrical nanopores are 60 nm in diameter, and the center-to-center distance, $\lambda_{C\text{-}C}$, between two adjacent nanopores is 110 nm. The porosity, p, of the PAMs is ~ 27% as determined by

$$p = \frac{2\pi}{\sqrt{3}}(\frac{r}{\lambda_{C-C}})^2 \qquad (4\text{-}1)$$

where the r is the radius of the nanopores. This geometry provides over 2 orders of magnitude larger surface areas for depositions of QDs than does a single solid substrate.[5] The lateral dimension of the PAMs used in the studies is ~ 1 x 1 cm^2.
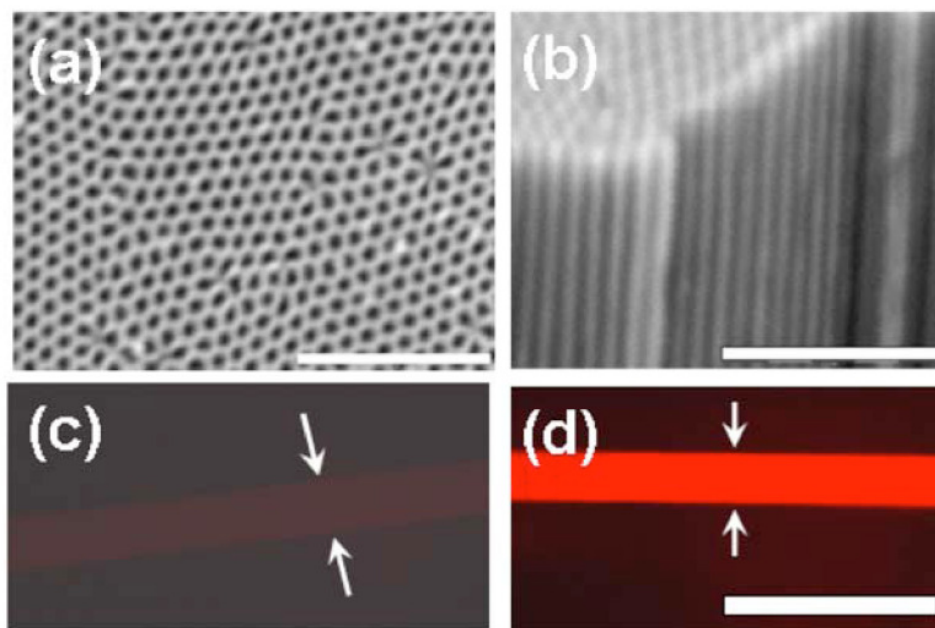
Figure 4-1. (color online). (a)-(b) SEM images of porous alumina membrane (PAM; unfilled with QDs) fabricated by a two-step electrochemical anodization process. (a) Topology, (b) Cross section. (c)-(d) Fluorescence images of the 13.22 µm thick PAM before (c) and after (d) filled with red emitting CdSe/ZnS QDs (side view). The fluorescence intensity of image (d) is 20 folds higher than image (c) under the same light intensity and exposure time. The scale bars are 1 µm in (a) and (b), 50 µm in (d), respectively.

The transmission spectra (solid curves) of freestanding PAMs before and after the deposition of CdSe/ZnS core/shell QDs with different sizes (diameter, D = 4.4nm in (a) and 5.5 nm in (b)) are shown in Figure 4-2. These spectra, measured by UV-Vis spectrometer, exhibit characteristic spectral maxima and minima,[5] and can be mathematically described using the transfer matrix formalism,[5, 13] given appropriate refractive indices and incident angle (90°, i.e., normal to the membrane surface). The reflective index is a function of the membrane thickness and porosity. The excellent agreement between the simulated spectra (black dashed curves) and measured spectra (black solid curves) of the blank PAMs for the

peak positions (Figure 4-2a and Figure 4-2b) yield the thicknesses of freestanding PAMs, which are 8.88 µm and 13.22 µm, respectively, using the known refractive indices and taking the porosity of blank PAM as 27% with the film thickness as the only adjustable parameter.[5] The fluorescence images of the 13.22 µm thick PAM before and after filled with red emitting CdSe/ZnS QDs are shown in Figure 4-1(c) and 4-1(d). The fluorescence intensity of the PAM after the deposition of QDs is 20 folds higher than a blank counterpart under the same light intensity and exposure time. Moreover, the uniform intensity along the depth of the membrane is clearly evident (Figure 4-1(d)). Taken together, QDs were filled into the cylindrical nanopores of the PAM.
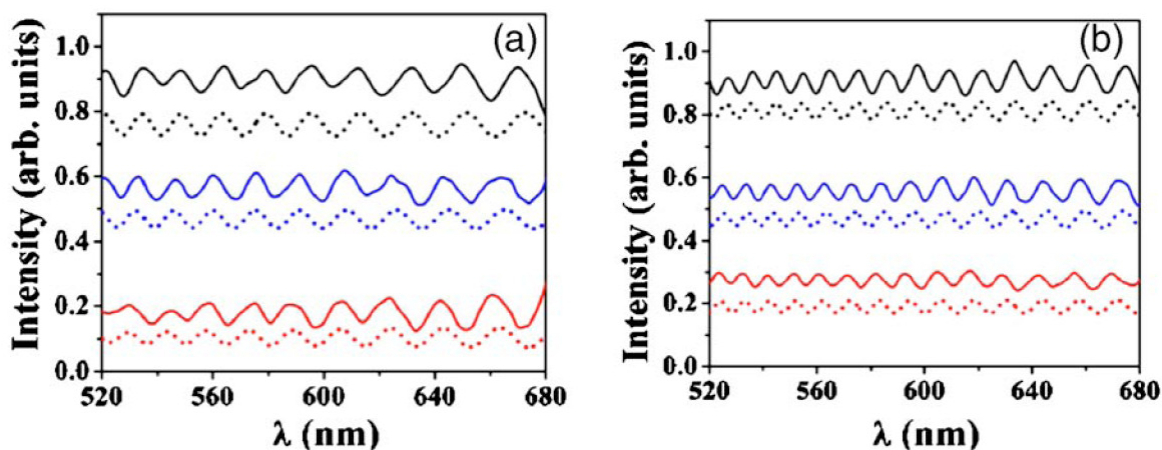
Figure 4-2. (color online). Transmission UV-Vis spectra of the freestanding PAMs with 27% porosity deposited with (a) 4.4 nm CdSe/ZnS QDs, (b) 5.5 nm CdSe/ZnS QDs. The thicknesses of the PAM in (a) and (b) are 8.88 µm and 13.22 µm, respectively. Black, blue, and red solid curves (from top to bottom) are the experimental spectra of the PAMs before the deposition, after the deposition, and their spectra difference, respectively. The corresponding dashed curves are the calculated spectra (i.e., the theoretical fittings).

Upon the deposition of the QDs, the refractive index of the membrane changed. The effective refractive index of the QD-filled cylindrical nanopore of the PAM, n_{eff_QD}, can be described by the Maxwell-Garnett (MG) effective medium theory.[5, 14] The general relation that correlates the effective dielectric function of QDs in the nanopore, ε_{eff_QD} with the dielectric functions of the QDs, ε_{QD} and the air, ε_{air} is given by

$$\frac{\varepsilon_{eff\_QD} - \varepsilon_{air}}{\varepsilon_{eff\_QD} + 2\varepsilon_{air}} = f \frac{\varepsilon_{QD} - \varepsilon_{air}}{\varepsilon_{QD} + 2\varepsilon_{air}} \qquad (4\text{-}2)$$

where f is the volume fraction of the QDs in the nanopore.[14, 15] Since the refractive indices, n and absorption coefficients, k of CdSe and ZnS as a function of wavelength are known,[16] the corresponding dielectric function ε_{QD} can be calculated based on the relation of $\varepsilon = (n + ik)^2$. Here it should be noted that the refractive index of QDs is obtained as follows.[17] The QDs are considered as spherical particles with a CdSe core and two coating layers (i. e., ZnS and TOPO). The volume ratios of CdSe to ZnS in the core/shell structure are 4/6 for red emitting (D = 5.5 nm) and 3/7 for orange emitting (D = 4.4 nm) QDs, respectively. The contribution from the stabilizing ligand, TOPO, is neglected in the calculation for the following reasons. First, the number of TOPO chains covering each QD was much less than 100.[18] Therefore, only a very thin layer of organic compound covered the surface of the QDs. Secondly, the refractive index of TOPO is close to that of air and much smaller than those of inorganic compounds (i.e., CdSe and ZnS). Thus, the average refractive index of QDs is calculated from the volume ratio of CdSe and ZnS. The effective refractive index of the membrane, n_{eff_PAM} after the loading of QDs can be written as

$$\frac{\varepsilon_{eff\_PAM} - \varepsilon_{Al_2O_3}}{\varepsilon_{eff\_PAM} + 2\varepsilon_{Al_2O_3}} = p \frac{\varepsilon_{QD/air} - \varepsilon_{Al_2O_3}}{\varepsilon_{QD/air} + 2\varepsilon_{Al_2O_3}} \qquad (4\text{-}3)$$

where $\varepsilon_{QD/air} = \varepsilon_{eff\_QD}$ in eq (4-2), ε_{Al2O3} is the dielectric function of insulating alumina, and p is porosity of blank PAM ($p = 27\%$). Similar to the calculation of ε_{QD} in the above, the ε_{Al2O3} is obtained given the known n and k of alumina.[19] Subsequently, the n_{eff_PAM} obtained from $\varepsilon_{eff\_PAM} = (n_{eff\_PAM} + ik_{eff\_PAM})^2$ is substituted into the transfer matrix formalism[5,13] with the adjustable f (i.e., the volume percentage of QDs deposited in the nanopores of the PAMs). The iterative calculations by combining eqs (4-2) and (4-3) are performed until best fits (blue dashed curves in Figure 4-2) with experimental data (blue solid curves) are reached so that the values of f are attained.

Upon the deposition of the QDs, the transmission spectra blue shifted relative to the blank PAMs (Figure 4-2). By fitting the experimental spectra (i.e., blue solid curves in Figure 4-2), the uptake of QDs within the cylindrical nanopores achieved by dip-coating was determined to be $f = 3\%$ for orange emitting QDs in the 8.8 µm thick PAM, and $f = 3.5\%$ for red emitting QDs in the 13.22 µm thick PAM. Thus, it is clear that the QDs only covered a very small volume of the nanopores.

Red-shifts of the reflection spectra were observed upon the depositions of the QDs when one-side-open PAMs were employed (solid curves in Fig 4-3). This phase difference is well known to be induced by the change of refractive index of the medium in the reflectivity measurments.[5] The angle of incidence of the UV-Vis to the membrane surface was 22.5° in the study. A 10 nm solid Al_2O_3 barrier layer known to be formed during anodization was included in the calculation of the reflection spectra.[5] Similar to the calculations of the transmission spectra, the thickness of the PAM and the amount f of QDs in the PAM can be determined using the transfer matrix formalism, yielding that $f = 2.2\%$ in the 11.44 µm thick

PAM occupied by the orange emitting QDs (λ_{max} = 598 nm) and f = 2.8% in the 9.45 µm thick PAM occupied by the red emitting QDs (λ_{max} = 632 nm). It is noteworthy that the numbers of QDs loaded in one-side-open PAMs are smaller than those in the freestanding PAMs. This is due to the fact that it is much more difficult for QD chloroform solutions, driven by the capillary force, to reach the closed end of the one-side-open PAM. In contrast, the freestanding PAMs can be readily accessed by QDs solutions from both sides.
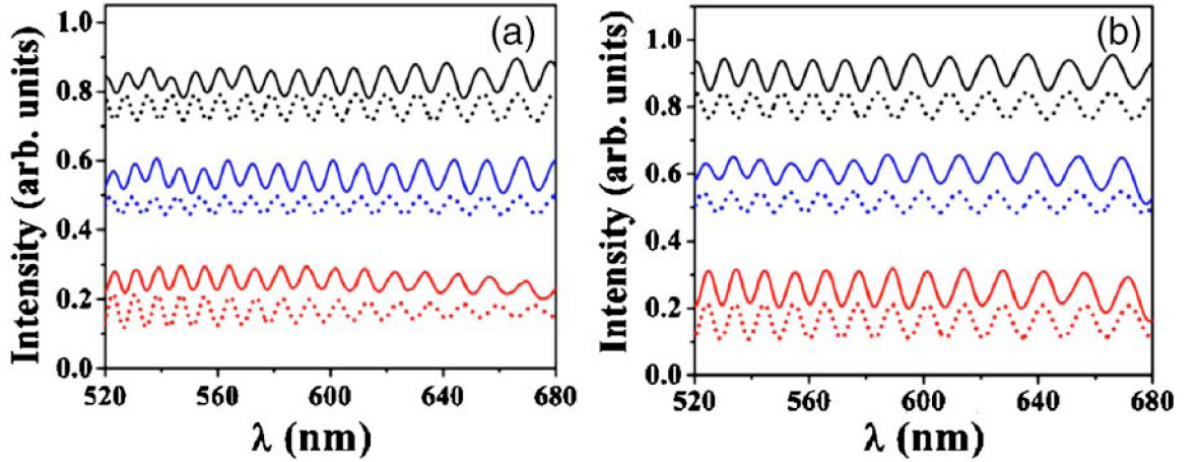
Figure 4-3. (color online). Reflection UV-Vis spectra of the freestanding PAMs with 27% porosity deposited with (a) 4.4 nm CdSe/ZnS QDs, (b) 5.5 nm CdSe/ZnS QDs. The thicknesses of the PAM in (a) and (b) are 11.44 µm and 9.45 µm, respectively. Black, blue, and red solid curves (from top to bottom) are the experimental spectra of the PAMs before the deposition, after the deposition, and their spectra difference, respectively. The corresponding dashed curves are the calculated spectra (i.e., the theoretical fittings).

After loading of the QDs within the nanopores of the PAM was confirmed, the fluorescence spectra of the PAMs before and after the deposition of the QDs were measured.

The PAM exhibited blue emissions in the 400-600 nm range with a broad peak position at 420–468 nm (dashed curves in Figure 4-4). These were attributed to the coactions of both the singly ionized oxygen vacancies and the luminescent centers transformed from oxalic impurities.[15, 20] The emission spectra of the filled PAMs showed λ_{max} at 602 nm and 632 nm, respectively. Accordingly, it is evident that the emission of the QDs was retained. The emission of the orange emitting QDs (D = 4.4nm) was slightly red shifted by ~3 nm relative to the dry-state QDs in the bulk (Figure 4-4a). This probably results from a slight aggregation of QDs within the nanopores. However, no shift was observed for red emitting QDs upon confinement (Figure 4-4b).
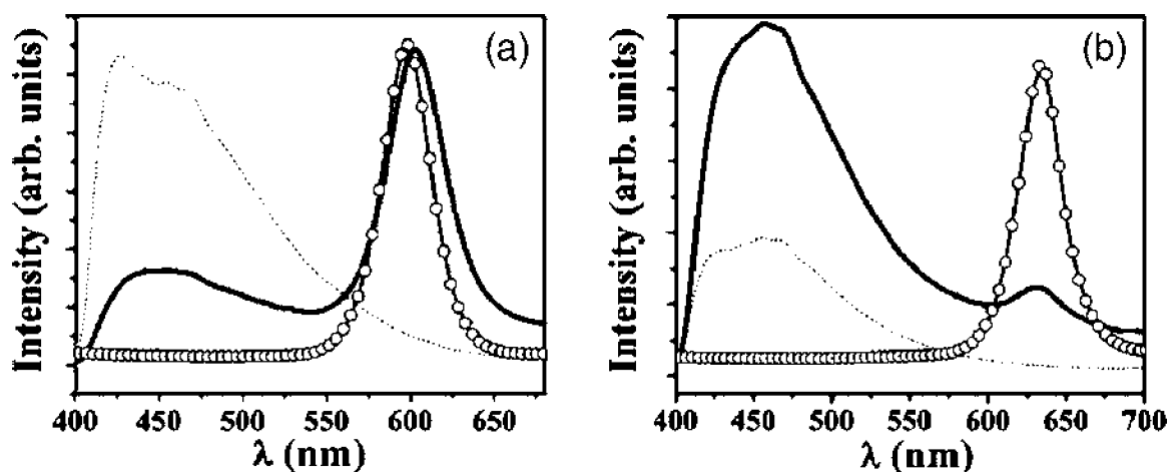
Figure 4-4. Emission spectra of freestanding PAMs before (dashed curve) and after deposited (solid curve) with (a) orange emitting (D = 4.4 nm) QDs and (b) red emitting (D = 5.5 nm) QDs. The corresponding emission spectra of QDs in dry state in bulk (i.e., without confinement) are shown in open circle curves.

Conclusion

In conclusion, we have described the optical properties of CdSe/ZnS core/shell QDs in a hexagonal array of highly ordered cylindrical nanopores of the PAMs by a simple dip-coating method. The PAM thickness and the amount of deposited QDs were determined from both transmission and reflection spectra, by modeling the changes in the UV-Vis spectra. The QD-filled PAMs were found to be highly fluorescent; their fluorescence was maintained within the cylindrical nanopores. We envision that the present study may provide some insights into optimizing nanostructured materials by spatially arranging nanoscopic elements in a well-controlled fashion for use in optoelectronic devices and biosensors.

References

1   H. Masuda and K. Fukuda, Ordered metal nanohole arrays made by a two-step replication of honeycomb structures of anodic alumina. *Science* **268**, 1466 (1995).

2   C.A. Mirkin, R.L. Letsinger, R.C. Mucic, and J. J. Storhoff, A DNA-based method for rationally assembling nanoparticles into macroscopic materials. *Nature* **382**, 607 (1996).

3   T. Hanaoka, H.P. Kormann, M. Kroll, T. Sawitowski, and G. Schmid, Three-dimensional assemblies of gold colloidal in nanoporous alumina membrane. *Euopean. Journal of Inorganic Chemistry* **807** (1998).

4   D. F. Qi, K. Kwong, K. Rademacher, M. Wolf, and J. F. Young, Optical emission of conjugated polymers adsorbed to nanoporous alumina. *Nano Letters* **3**, 1265 (2003).

5   S. Pan and L.J. Rothberg, Interferometric sensing of biomolecular binding using nanoporous aluminum oxide templates. *Nano Letters* **3**, 811 (2003).

6   V.L. Colvin, M.C. Schlamp, and A.P. Alivisatos, Light-emitting diodes made from cadmium selenide nanocrystals and a semiconducting polymer. *Nature* **370**, 354 (1994).

7   W.U. Huynh, J.J. Dittmer, and A.P. Alivisatos, Hybrid nanorod-polymer solar cells. *Science* **295**, 2425 (2002).

8   I. L. Medintz, H. T. Uyeda, E. R. Goldman, and H. Mattoussi, Quantum dot bioconjugates for imaging, labelling and sensing. *Nature Materials* **4**, 435 (2005).

9   M.J. Misner, H. Skaff, T. Emrick, and T. P. Russell, Directed deposition of nanoparticles using diblock copolymer. *Advanced Mateials* **15**, 221 (2003).

10   Q.L. Zhang, T. Xu, D. Butterfield, M. J. Misner, D. Y. Ryu, T. Emrick, and T. P. Russell, Controlled placement of CdSe nanoparticles in diblock copolymer templates by electrophoretic deposition. *Nano Letters* **5**, 357 (2005).

11   X. Peng, L. Manna, W.D. Yang, J. Wickham, E. Scher, C. Kadavanich, and A. P. Alivisatos, Shape control of CdSe nanocrystals. *Nature* **404**, 59 (2000).

12   M.A. Hines and P. Guyot-Sionnest, Synthesis and characterization of strongly luminescing ZnS-capped CdSe nanocrystals *Journal of Physical Chemistry B* **100**, 468 (1996).

13   P. Yeh, *Optical Waves in Layered Media*. (Wiley-Interscience, 1988).

14   C. A. Jr. Foss, G. L. Hornyak, J. A. Stockert, and C. R. Martin, Template-synthesized nanoscopic gold particles-optical-spectra and the effectsof particle-size and shape. *Journal of Physical Chemistry* **98**, 2963 (1994); C. A. Jr. Foss, M. J. Tierney, and C. R. Martin Template synthesis of infrared-transparent metal microcylinders-comparison of optical-properties with the predictions of effective medium theory. *Journal of Physical Chemistry* **96,** 9001 (1992).

15   J. Hohlbein, U. Rehn, and R. B. Wehrspohn, In-situ optical characterisation of porous alumina. *Physical |State of Solids (a)* **201**, 803 (2004).

16   E. D. Palik, *Handbook of Optical Constants of Solids*. (Academic Press, INC., 1985 and 1991).

17   C. F. Bohren and D. R. Huffman, *Absorption and Scattering of Light by Small Particles*. (Wiely-Interscience, 1998).

18   G. Kalyuzhny and R. W. Murray, Ligand Effects on Optical Properties of CdSe Nanocrystals. *Jorunal of Physical Chemistry B* **109**, 7012 (2005).

19   L. J. Harris, *Optical Society of America* **45**, 27 (1955).

20   W. L. Xu, M. J. Zheng, S. Wu, and W. Z. Shen Effects of high-temperature annealing on structural and optical properties of highly ordered porous alumina membranes. *Applied Physics Letter.* **85**, 4364 (2004).

CHAPTER 5. ORGANIC-INORGANIC NANOCOMPOSITES VIA DIRECTLY GRAFTING CONJUGATED POLYMERS ONTO QUANTUM DOTS

Jun Xu, Jun Wang, Mike Mitchell, Prasun Mukherjee, Malika Jeffries-EL, Jacob W. Petrich, and Zhiqun Lin*

Abstract

Nanocomposites of poly(3-hexylthiophene)−cadmium selenide (P3HT−CdSe) were synthesized by *directly* grafting vinyl terminated P3HT onto [(4-bromophenyl)methyl]dicotylphosphine oxide (DOPO-Br)-functionalized CdSe quantum dot (QD) surfaces via a mild palladium-catalyzed Heck coupling, *thereby dispensing with the need for ligand exchange chemistry. The resulting P3HT−CdSe nanocomposites possess a well-defined interface, thus significantly promoting the dispersion of CdSe within the P3HT matrix and facilitating the electronic interaction between these two components*. The photophysical properties of nanocomposites were found to differ from the conventional composites in which P3HT and CdSe QDs were physically mixed. Solid-state emission spectra of nanocomposites suggested the charge transfer from P3HT to CdSe QDs, while the energy transfer from 3.5-nm CdSe QD to P3HT was implicated in the P3HT/CdSe composites. A faster decay in lifetime further confirmed the occurrence of charge transfer in P3HT−CdSe nanocomposites.

Introduction

Due to their semiconductor-like optical and electronic properties, conjugated polymers (CPs) have been extensively researched for two decades. The optoelectronic properties of CPs depend heavily on the physical conformation of the polymer chains.[1-3] The most widely studied CP is regioregular poly(3-hexylthiophene) (*rr* P3HT), consisting of a rather rigid backbone with pendant hexyl side chains that allow solubilization.[4-7] Quantum dots (QDs) are highly emissive, spherical nanoparticles with a few nanometers in diameter.[8-11] For QDs such as cadmium selenide (CdSe),[8, 12] the variation of particle size provides continuous and predictable changes in fluorescence emission due to their quantum-confined nature. An appropriate surface passivation with a monolayer of coordinating organic ligands is crucial to ensure the solubility and miscibility of QDs with the host environment, and to retain the spectroscopic properties of the materials by preventing QDs from aggregation.[13, 14] Ligand exchange permits derivatization with a broad range of functional groups. However, it suffers from incomplete surface coverage although a study on nearly quantitatively exchange has been reported recently.[15] As a consequence, the fluorescence emission is quenched due to aggregations of QDs,[16] or oscillates due to adsorption and desorption of surface ligand.[17]

Composites of quantum dots/conjugate polymers (CP/QD) are of interest from the standpoint of increased performance relative to either of the non-hybrid counterparts with many applications envisioned in the areas of photovoltaic cells[18-21] and LEDs.[14, 22-24] They inherit decent mechanical strength from CPs and good photostability and high conductivity from QDs. The CP/QD composites are widely prepared by mixing these two components or by constructing a CP/QD bilayer (only a small faction of excitons, i.e., the bound electron-hole pairs, are able to diffuse to the interface where they are ionized) or CP/QD alternating multilayer both physically or chemically. Thus, it is difficult to control the detailed morphology and dispersion of QDs within CPs. The interface between CP and QD, accomplished by stripping ligand from QDs during film processing, is not well controlled,

thereby reducing the efficient electronic interactions between them. The effective charge transfer, profoundly influenced by the quality of the interface, is crucial for CP/QD composite for use in photovoltaic cells.[25-27] This implies that a bicontinuous and nanoscopic phase-separated mixture of CP/QD is favorable for charge generation and transport, which is currently difficult to realize by using a conventional blending approach.[28-30] On the other hand, for use in LED, it is important to stabilize QDs in an appropriate host with retention of the fluorescence emission. However, possible nanoparticle aggregation in composites often limits the energy transfer pathway and leads to self-quenching of the fluorescence of QDs.

In this context, the ability to chemically tether QD with CP (i.e., preparing CP−QD nanocomposites with well-controlled interfaces) provides a means of achieving uniform dispersion of nanoparticles and maximizing the interfacial area, which carries advantages over cases where nanoparticle aggregation dominates. To date only a few elegant studies have centered on the direct integration of QDs into oligomeric CPs (including branched conjugated oligomeric dendrons[31]) via ligand exchange with insulated surfactants,[15, 20, 21, 31, 32] electrostatic interaction, or direct growth from the QDs' surface[13, 14] to achieve a more controlled interface on a molecular scale and morphology. The length of the conjugated oligomers (trimer, tetramer, or pentamer) was shorter than the conjugation length of corresponding CPs. To further manipulate the photophysics of the nanocomposites by controlling the chain conformation of CPs in the surrounding environment, it is of importance to graft longer chain CPs on the QD surface.

To this end, here we report the preparation of CP−QD nanocomposites based on a rational design in which QDs were tailored with relatively long chain CPs (i.e., the chain length was longer than the conjugation length of CP). Nanocomposites of poly(3-hexylthiophene)−cadmium selenide (P3HT−CdSe) were synthesized by *directly* grafting relatively long chain, vinyl terminated P3HT onto [(4-bromophenyl)methyl]dicotylphosphine oxide (DOPO-Br)-functionalized CdSe QD surfaces via a mild palladium-catalyzed Heck

coupling (i.e., a "grafting onto" method) as outlined in Scheme 1, *thereby dispensing with the need for ligand exchange chemistry*. The resulting P3HT−CdSe nanocomposites possess a well-defined interface, *thus significantly promoting the dispersion of CdSe within the P3HT matrix and facilitating the electronic interaction between these two components*. The photophysical properties of nanocomposites were found to differ from the conventional composites in which P3HT and CdSe QDs were physically mixed. Solid-state emission spectra of nanocomposites suggested the charge transfer from P3HT to CdSe QDs, while the energy transfer from CdSe QD to P3HT was implicated in the P3HT/CdSe composites. A faster decay in lifetime further confirmed the occurrence of charge transfer in P3HT−CdSe nanocomposites.

Experimental

All chemicals, including hexadecylamine (HDA), hexylphosphoric acid (HPA), cadmium acetate $(Cd(OAc)_2)$, trioctylphosphine (TOP), tri-t-butylphosphine, Tris(dibenzylideneacetone)dipalladium(0) $(Pd_2(dba)_3)$, and N-methyldicyclohexylamine were purchased from Aldrich and used as received. THF was used freshly from distillation.

Synthesis of (DOPO-Br)-functionalized CdSe: The [(4-bromophenyl)methyl]dioctylphosphine oxide (DOPO-Br)-functionalized CdSe was synthesized based on a ligand-exchange-free procedure.[13, 14] Briefly, 50 mg $Cd(OAc)_2$, 160 mg HPA, 0.93 g HDA, and 1.5 g [(4-bromophenyl)methyl]dioctylphosphine oxide (DOPO-Br) were degassed at 120 °C and heated to 270 °C under Ar. Then, 1.2 ml Se-TOP stock solution, made by dissolving 0.4 g Se in 8 g TOP, was injected swiftly. The size of CdSe QDs was readily controlled by altering the growth time. The final product was dissolved in chloroform and precipitated twice by adding minimum amount of methanol.

Synthesis of P3HT−CdSe nanocomposites: The regioregular P3HT (*rr* P3HT) was synthesized via a quasi-living polymerization.[5, 33-35] 1 mg $Pd_2(dba)_3$, 10 mg vinyl terminated

P3HT, and 20mg (DOPO-Br)-functionalized CdSe QDs was loaded in a reaction vial. The vial was vacuumed and refilled with Ar. Then, 0.08 ml N-methyldicycylohexylamine, 0.06 ml tri-t-butylphosphine THF solution at concentration of 100mg/ml, and 0.5 ml THF were loaded in sequence. The reaction mixture was kept stirring under Ar environment in a 50 °C oil bath for 20 h. The final product, i.e., P3HT−CdSe nanocomposites, was diluted 20 times and precipitated with minimal amount of methanol.
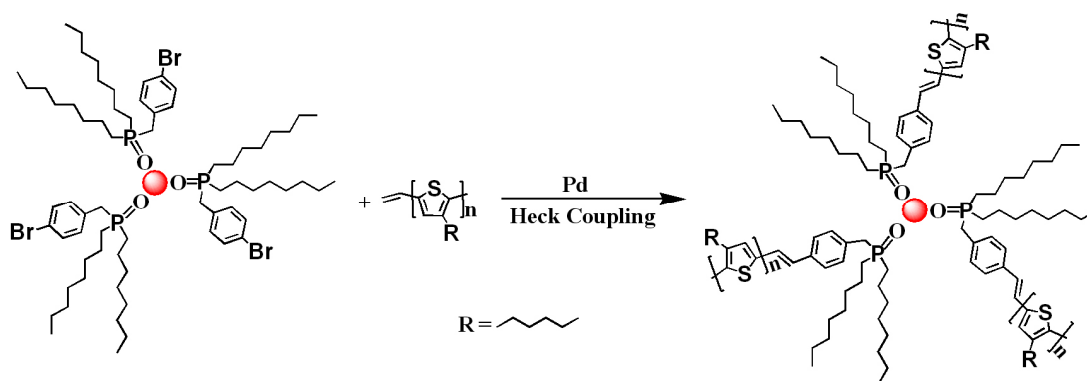
Scheme 5-1. Grafting vinyl terminated P3HT onto [(4-bromophenyl)methyl]dicotylphosphine oxide (DOPO-Br) functionalized CdSe QDs.

Characterizations: The diameter of CdSe QD was determined by TEM measurements (JEOL 1200EX scanning/transmission electron microscope (STEM); operated at 80 kV). The absorption spectra were recorded with a home-made UV-vis spectrometer. The emission spectra were taken with a Nikon Eclipse TE2000-E microscope coupled with an optical insights hyperspectral unit and a Cascade 512B camera (Roger Scientific). The regioregularity of P3HT was determined by ^{1}H-NMR (Varian VXR-300). The absolute molecular weight and polydispersity index of *rr* P3HT were measured by MALDI-TOF (Thermo Bioanalysis Dynamo Mass Analyzer). The coupling of vinyl terminated P3HT with DOPO-Br capped CdSe QDs was verified by ^{1}H-NMR and ^{31}P-NMR (Varian VXR-400)

spectroscopies. The grafting density of P3HT chains on the CdSe surface was determined by thermogravimetry analysis (TGA; TA Instrument TGA Q 50). The fluorescence lifetimes were measured using time-correlated single-photon counting (TCSPC)) methodology.[14] The full-width–at-half-maximum (FWHM) of the instrument response function was ≤ 100 ps. All decays were collected by exciting the sample with vertical polarization. The fluorescence emission was collected with a perpendicular orientation of the emission polarizer with respect to the excitation polarization. This arrangement eliminated possible interference from scattered light in solid state fluorescence measurements.

Results and Discussion

The [(4-bromophenyl)methyl]dicotylphosphine oxide (DOPO-Br)-functionalized CdSe was synthesized based on a ligand-exchange-free procedure (see Experimental).[13, 14] The diameter of CdSe QD (orange-emitting) was 3.5 ± 0.4 nm, as estimated from TEM imaging. Figure 5-1 shows the absorption and emission spectra of (DOPO-Br)-functionalized CdSe. The emission of CdSe QD in dry state was slightly red-shifted by 3 nm ($\lambda_{em,\,CdSe}$ = 593 nm) as compared to that in chloroform solution. This probably resulted from a slight aggregation of QDs in dry state.
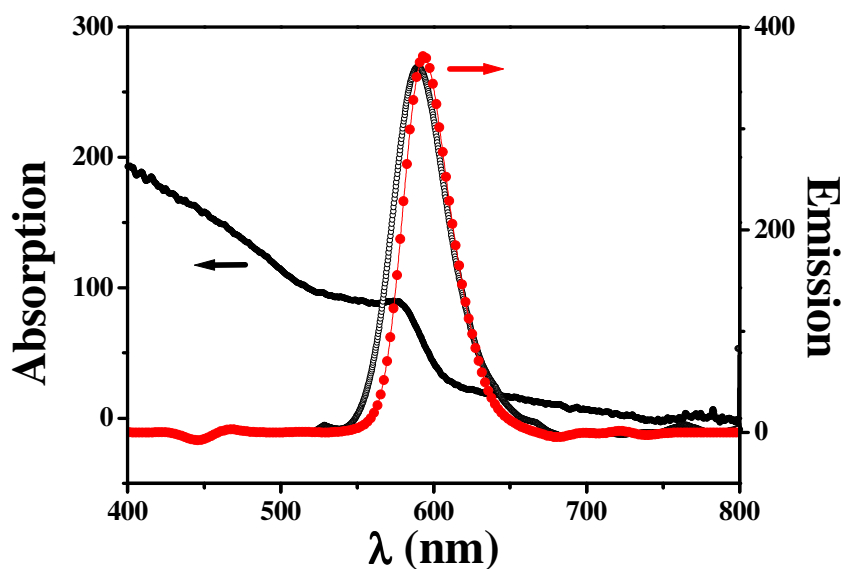
Figure 5-1. Absorption and emission spectra of (DOPO-Br)-functionalized CdSe QD (Diameter, D = 3.5 nm). The absorption spectrum was obtained from the CdSe chloroform solution. The emission spectrum of QDs red-shifted upon drying (red solid circles) from the chloroform solution (open circles).

Chemically attaching end-functionalized polymers onto functionalized nanoparticles has been a common approach to modify nanoparticles (NPs), such as Au NP.[36, 37] The key is to first synthesize both NPs and polymers with compatible functional groups, which allow them to react with each other under relatively mild condition without sacrificing the stability and photophysical properties of each component. In the present study, the regioregular P3HT (*rr* P3HT) was synthesized via a quasi-living polymerization.[5, 33-35] One of its end was functionalized with the vinyl group using a modified Grignard metathasis reaction.[4] The regioregularity was greater than 94% as determined by ^{1}H-NMR.[4, 5] The absolute molecular weight and polydispersity index of *rr* P3HT were 2,404 and 1.12, respectively, as measured by MALDI-TOF. This corresponds to 14 repeat units (i.e., 10.4 nm long given that the length of a thiophene unit is 0.74 nm). It is relatively longer than the effective conjugation length which is approximately 9-10 thiophene units,[38, 39] thereby maximizaing the possibility

associated with the interchain interaction that occurs when the molecular weight of P3HT is high.

The absorption and emission spectra of *rr* P3HT are shown in Figure 5-2. For the P3HT THF solution, the absorption and emission maxima were at 450 nm and 572 nm, respectively. A red-shifted to 510 nm and 730 nm ($\lambda_{em, P3HT}$ = 730 nm), respectively was observed upon drying.[39] The emission spectrum of the dried film was acquired from a sample sealed in an Ar filled vial to prevent photo degradation.[39] The vibronic structures of P3HT are clearly evident (i.e., 0-0 emission peak at 670 nm and 0-1 emission peak at 730 nm).[40] Subsequently, P3HT−CdSe nanocomposites were obtained by a mild palladium-catalyzed Heck coupling. of vinyl terminated *rr* P3HT chains with DOPO-Br-functionalized CdSe QDs (i.e., a "graft onto" method; Scheme 1) (see Experimental Methods).
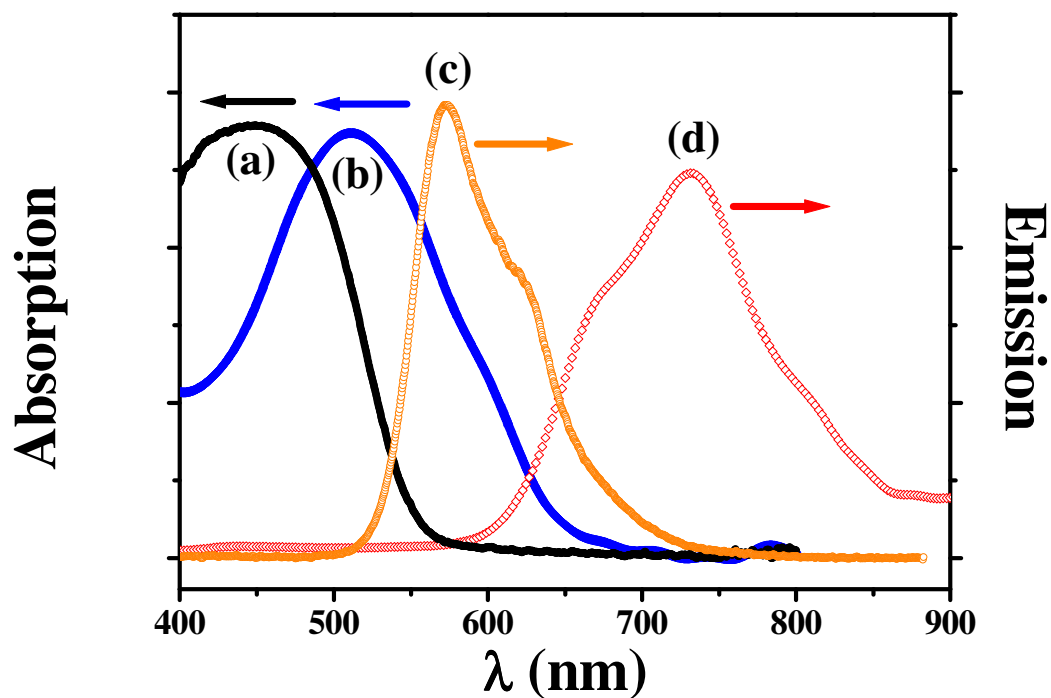

Figure 5-2. Absorption and emission spectra of vinyl terminated P3HT in THF solution in (a) and (c), respectively, and in dry film in (b) and (d), respectively.

We note that coating CdSe surface with higher band gap materials, such as zinc sulfide (ZnS) prevents the surface quenching of excitons in the emissive CdSe core by passivating most of vacancies and trap sites on the CdSe surface, and thus increases the quantum yield and photostability of the QDs. However, the ZnS shell also increases the distance between the CdSe core and the ligand attached onto it, thereby decreasing energy or charge transfer efficiency in the CP−QD nanocomposites. On the other hand, the performance of photovoltaic cells based on the CP/QD composites is limited by the hole mobility in the CP.[41] Compared to other CPs, the regioregular (*rr*) P3HT possesses excellent environmental stability, fast hole mobility (0.1 cm^2/V-s in field-effect transistors) and tailorable electrochemical properties.[7, 42] Taken together, CdSe and *rr* P3HT were chosen as model QD and CP to prepare the P3HT−CdSe nanocomposites.

The success of coupling of vinyl terminated P3HT with DOPO-Br capped CdSe QDs was confirmed by ^{1}H-NMR and ^{31}P-NMR spectroscopies. The two proton signals from free vinyl end group on P3HT at 5.1 ppm and 5.5 ppm disappeared after coupling (see Supporting Information, Figure S1). Furthermore, the ^{31}P signal from DOPO-Br shifted from 47 ppm to 50 ppm after it was bonded to the CdSe surface (i.e., forming (DOPO-Br)-CdSe). It further shifted by 17 ppm to 67 ppm after (DOPO-Br)-CdSe coupled with vinyl terminated P3HT, suggesting that P3HT was grafted onto the DOPO-Br capped CdSe (see Supporting Information, Figure S2). The "grafting onto" method was simple to perform. Thus, rather than oligomer or oligomeric dendron, relatively high molecular weight CP, was chemically anchored to QDs. More importantly, the absence of ligand-exchange chemistry in the present synthesis allowed the inherent fluorescence of the P3HT-tailored CdSe QDs to be maintained.

The grafting density of P3HT chains on the CdSe surface was determined by thermogravimetry analysis (TGA) (see Supporting Information, Figure 5-8). The molecular weight of the 3.5-nm CdSe QDs was estimated to be 113,000 g/mol.[43] The mass loss between

400°C and 500 °C was attributed exclusively to the decomposition of P3HT, while the combined mass loss due to partial decomposition of P3HT and the decomposition of unreacted DOPO-Br was found at temperature below 400 °C. Thus, the CdSe QD was grafted with 22 P3HT chains (i.e., 22 P3HT molecules per CdSe QD).

Figure 5-3 shows the TEM images of P3HT/CdSe composites and P3HT−CdSe nanocomposites prepared by physically mixing vinyl terminated P3HT and DOPO-Br functionalized CdSe (i.e., without adding catalyst, $Pd_2(dba)_3$) and by Heck coupling of these two functionalized components (Scheme 1), respectively. The P3HT/CdSe composites exhibited a significant phase separation as evidenced in Figure 5-3a. In sharp contrast, the CdSe QDs were well dispersed in P3HT−CdSe nanocomposites (Figure 5-3b). It is noteworthy that, as compared with other polymer-coated nanoparticles (e.g., nanocomposite of polystyrene-*b*-poly(ethylene oxide) and Au nanoparticles[37]), no clear P3HT coating at the periphery of the QDs can be imaged. This may be due to that the electron density of CdSe is relatively low as compared with other noble metals, e.g., Au, and P3HT had high regioregularity (i.e., behaves like a rigid rod) which makes it difficult for the P3HT chains to collapse at the surface of CdSe core into a dense shell layer, as in the case of flexible homopolymer.[44]
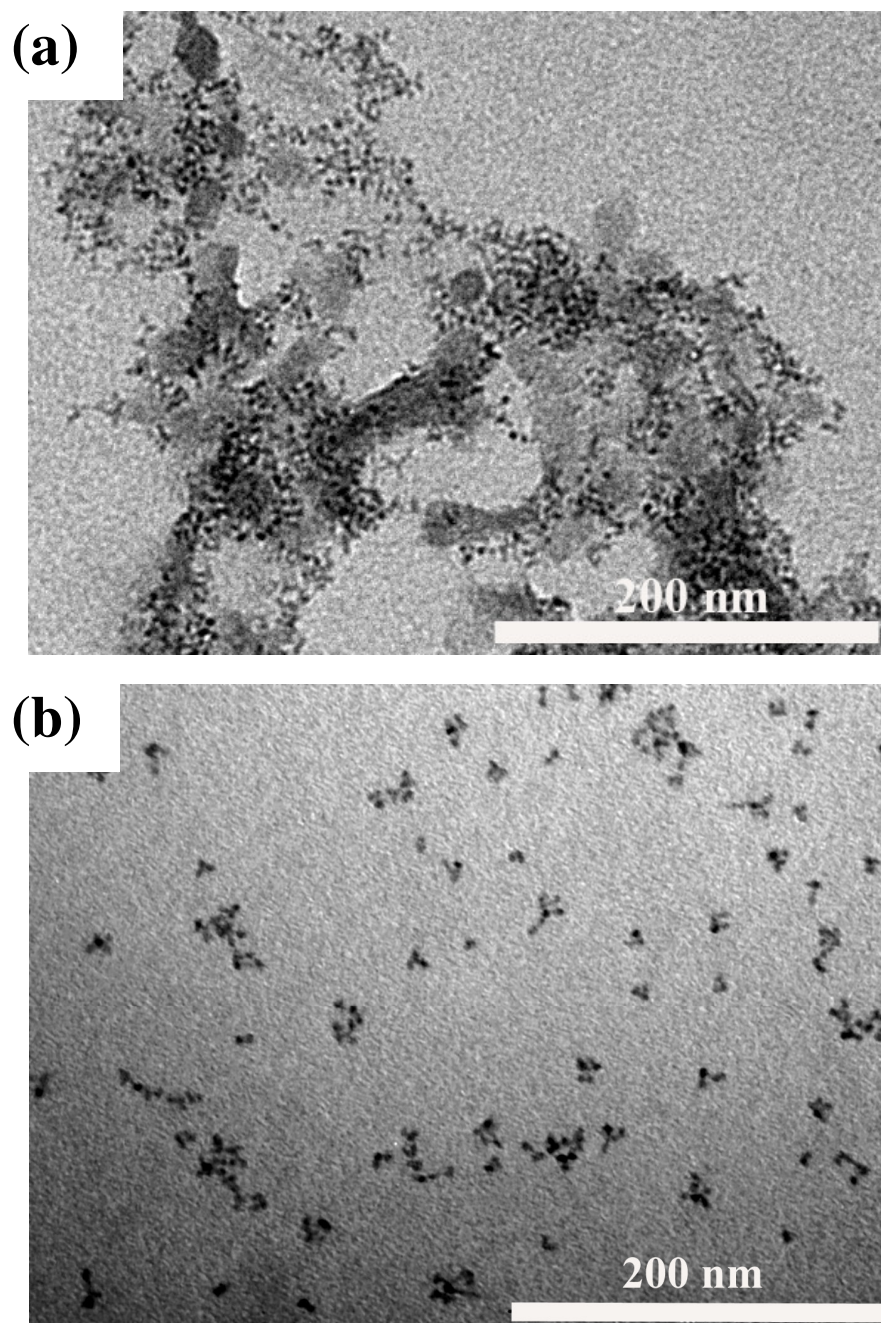
Figure 5-3. TEM images of (a) the composites of (DOPO-Br)-functionalized CdSe and vinyl terminated P3HT prepared by physically mixing these two components, and (b) the nanocomposites of P3HT−CdSe prepared by grafting vinyl terminated P3HT onto (DOPO-Br)-functionalized CdSe.

In order to explore the difference on photophysical properties between nanocomposites (chemically anchoring) and composite (physical mixing), a composite of P3HT/CdSe was prepared to serve as a control. Figure 4a shows the absorption spectra of the P3HT/CdSe composite and the P3HT−CdSe nanocomposites in THF. The absorbance resembled a superposition of the two components with no other apparent features present. The P3HT/CdSe composite was prepared in such a way that its absorption spectrum was delicately tuned to match that of the P3HT−CdSe nanocomposites. Thus, the number of P3HT chains per CdSe QD in the P3HT/CdSe composites can be roughly estimated based on the TGA results of the P3HT−CdSe nanocomposites (Figure 5-8): the approximate ratio of P3HT to CdSe is 22:1. It is worth noting that the TEM image of the P3HT/CdSe composites in Figure 3a was actually taken from the sample prepared by casting the abovementioned P3HT/CdSe THF solution onto carbon-coated TEM copper grids. For the P3HT/CdSe composite in THF solution, two peaks at 432 nm and 550 nm were seen, corresponding to the P3HT and CdSe absorption, respectively (Figure 5-4a). The absorption of P3HT in the composite blue-shifted to 432 nm from 450 nm in the vinyl terminated P3HT THF solution (Figure 5-2). This may be due to the overlap of the absorption spectrum of P3HT (Figure 5-2) with the broad absorption band of CdSe below 550 nm (Figure 5-1). Relative to the spectrum of the P3HT/CdSe composites in which the absorption maximum of CdSe was at 550 nm, the absorption of CdSe upon grafting with P3HT (i.e., P3HT−CdSe nanocomposites) was red-shifted (Figure 4a). This can be attributed to the changes in the dielectric environment (i.e., placing CdSe QDs in intimate contact with P3HT) that perturb the energy of the quantum-confined exciton of CdSe.[45]
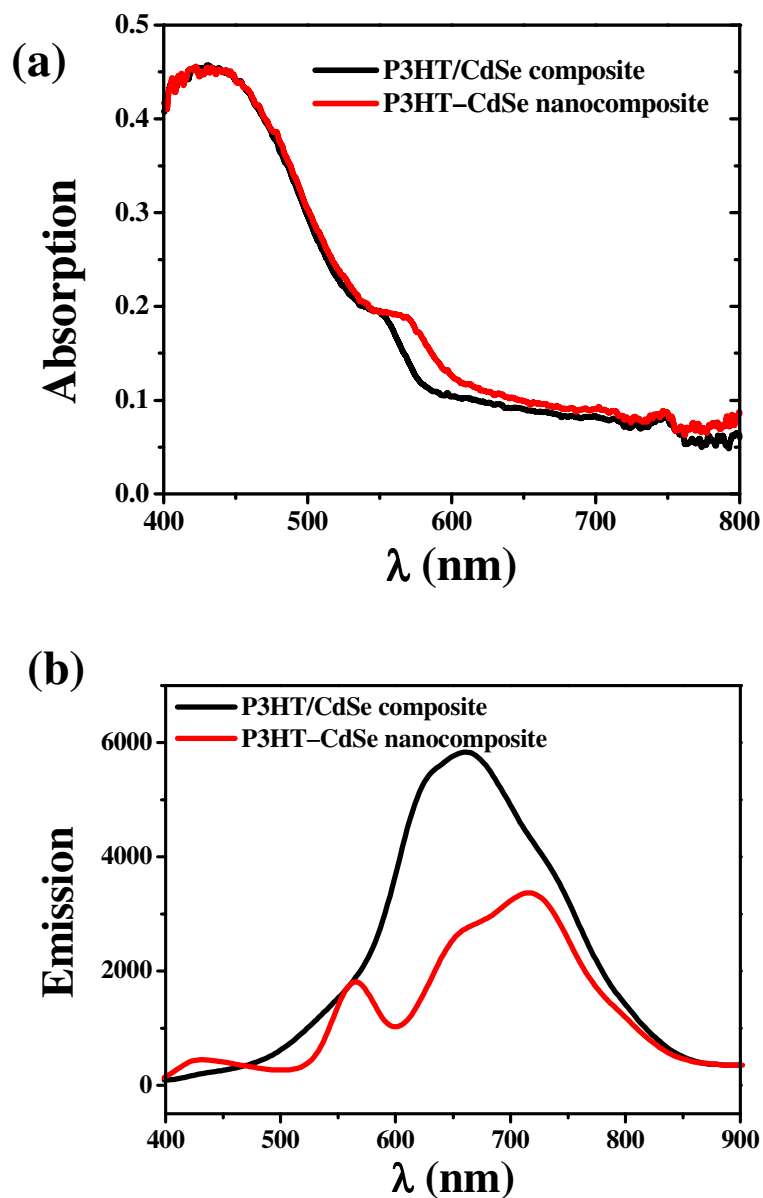
Figure 5-4. (a) Absorption spectra of the composites of (DOPO-Br)-functionalized CdSe and vinyl terminated P3HT (black curve) and the nanocomposites of P3HT−CdSe (red curve) in THF. (b) Corresponding emission spectra in dry state.

In solid state the emission spectrum of CdSe QD ($\lambda_{em,\,CdSe}$ = 593 nm) overlapped the absorption spectrum of P3HT (Figure 5-1 and 5-2b), thus upon excitation, the energy transfer

from excited CdSe QD to P3HT may be expected in which the quenching of CdSe emission would be accompanied by a complementary growth of emission of P3HT at longer wavelength.[46] The P3HT/CdSe composites exhibited emission maximum at 670 nm, and the emission of CdSe QDs was completely suppressed, indicating the energy transfer from excited CdSe QDs to P3HT. The emission maximum of P3HT in the composite blue-shifted to 670 nm (Figure 5-4b) as compared to the vinyl terminated P3HT in dry state in which $\lambda_{em,}$ $_{P3HT}$ = 730 nm (Figure 5-2d). This may be attributed to the presence of CdSe QDs in the composite that disrupted P3HT crystalline order and, thus, suppressed the P3HT interchain excitation.[47] The formation of exciplex between holes on P3HT and electrons on CdSe QDs[47] may also account for the blueshift of emission peak to 670 nm.

For the P3HT−CdSe nanocomposites, however, the charge transfer from P3HT to CdSe dominated (Figure 5-4b). Placing P3HT in intimate contact with CdSe provided a direct electronic interaction between them. The electrons formed upon excitation of P3HT can be directly injected onto the CdSe surface to passivate the surface trap sites.[48] Due to a good quality surface passivation of the CdSe QD, represented as the high emission intensity, there were limited amount of trap sites on the CdSe surface. Thus, the vacant trap sites could easily be passivated by electrons from P3HT, thereby enhancing the radiative recombination probability within CdSe QDs.[18, 48] It is interesting to note that the emission maximum of CdSe in the nanocomposites was at 565 nm (Figure 5-4b) as opposed to 590 nm in CdSe THF solution (Figure 5-1). This may be due to uneven passivation of QD surface via the charge transfer from P3HT. The 3.5-nm CdSe QDs had a size distribution of +/- 0.3 nm. The smaller QDs had less surface/volume ratio, they possessed less vacant surface trap sites, which in turn were easily filled by electrons injected from excited P3HT. As a consequence, the emission of smaller QDs was enhanced the most, which caused the emission peak to blue-shift to 565 nm.

Time-resolved photoluminescence (PL) measurements (i.e., ultrafast emission dynamics), monitored at the wavelength above 550 nm, was performed to give additional information on the charge transfer dynamics in the P3HT−CdSe nanocomposites by measuring the fluorescence lifetimes using time-correlated single-photon counting (TCSPC)) methodology (Figure 5-5).[14] The apparatus for the TCSPC measurements was described in details elsewhere.[49, 50] The solid-state dynamic process took place on the picosecond timescale and involved diffusion of the electronic excitations from P3HT to CdSe.[51] The measurements revealed that the luminescence of the P3HT−CdSe nanocomposites had a lifetime of 160 ps, while it was 240 ps in the pure homopolymer, *rr* P3HT (Figure 5-5). The faster PL decay of the P3HT−CdSe nanocomposites than that of P3HT can be attributed to the improved interfacial contact between P3HT and CdSe in the nanocomposites, where it is easy for the exciton to find the interface and dissociate, representing as a rapid charge transfer from P3HT to CdSe.[52, 53] This is consistent with the static PL measurement (red curve in Figure 4). It is important to note that the lifetime of the P3HT/CdSe composites in solid state was 490 ps, which is longer than that of P3HT (i.e., 240 ps). This supported the energy transfer mechanism hypothesized in the static PL measurement of the P3HT/CdSe composites (black curve in Figure 4). The insulating ligand (i.e., (DOPO-Br) on the CdSe surface hindered the charge transfer between P3HT and CdSe, leading to the energy transfer dominant in the P3HT/CdSe composites.
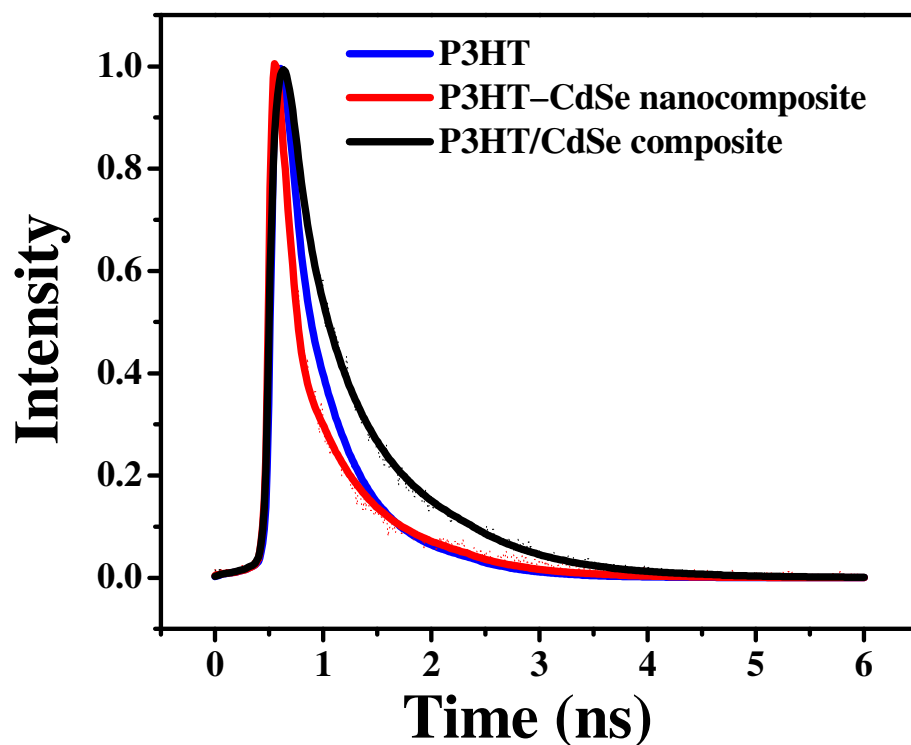
Figure 5-5. Normalized time-resolved photoluminescence decays of the P3HT (blue), the P3HT/CdSe composites (black), and the P3HT−CdSe nanocomposites (red), respectively, monitored at $\lambda_{exc} = $ 410 nm and $\lambda_{em} \geq$ 550 nm. The curve fitting yielded the average lifetime of P3HT, P3HT/CdSe, and P3HT−CdSe of 240 ps, 490 ps, and 160 ps, respectively.

Conclusion

In summary, placing CPs in intimate contact with QDs (i.e., preparing CP−QD nanocomposites) provided a means of achieving uniform dispersion of QDs and maximizing the interfacial area of P3HT and CdSe, thereby facilitating efficient electronic interaction between them. Rather than oligomeric CP, a relatively long chain CP, vinyl-terminated highly regioregular P3HT (14 thiophene units) was chemically tethered to the [(4-bromophenyl)methyl]dicotylphosphine oxide (DOPO-Br)-functionalized CdSe QD surface via a mild palladium-catalyzed Heck coupling (i.e., a "grafting onto" route to P3HT−CdSe nanocomposites; there is no need for ligand exchange chemistry). The "grafting onto"

method was simple to perform. The success of the coupling was confirmed by the ^{1}H-NMR and ^{31}P-NMR spectroscopies. The number of P3HT bound to each CdSe QD was estimated by TGA. The photophysical properties of nanocomposites were found to differ from the conventional composites in which P3HT and CdSe QDs were physically mixed. Solid-state emission spectra of nanocomposites suggested the charge transfer from P3HT to 3.5-nm CdSe QDs, while the energy transfer from 3.5-nm CdSe QD to P3HT was implicated in the P3HT/CdSe composites. A faster decay in lifetime further confirmed the occurrence of charge transfer in the nanocomposites. We envision that the P3HT−CdSe nanocomposites can be utilized for constructing one-layer of solar cell to explore the possible optoelectronic device application. This work is currently under investigation.

Acknowledgement
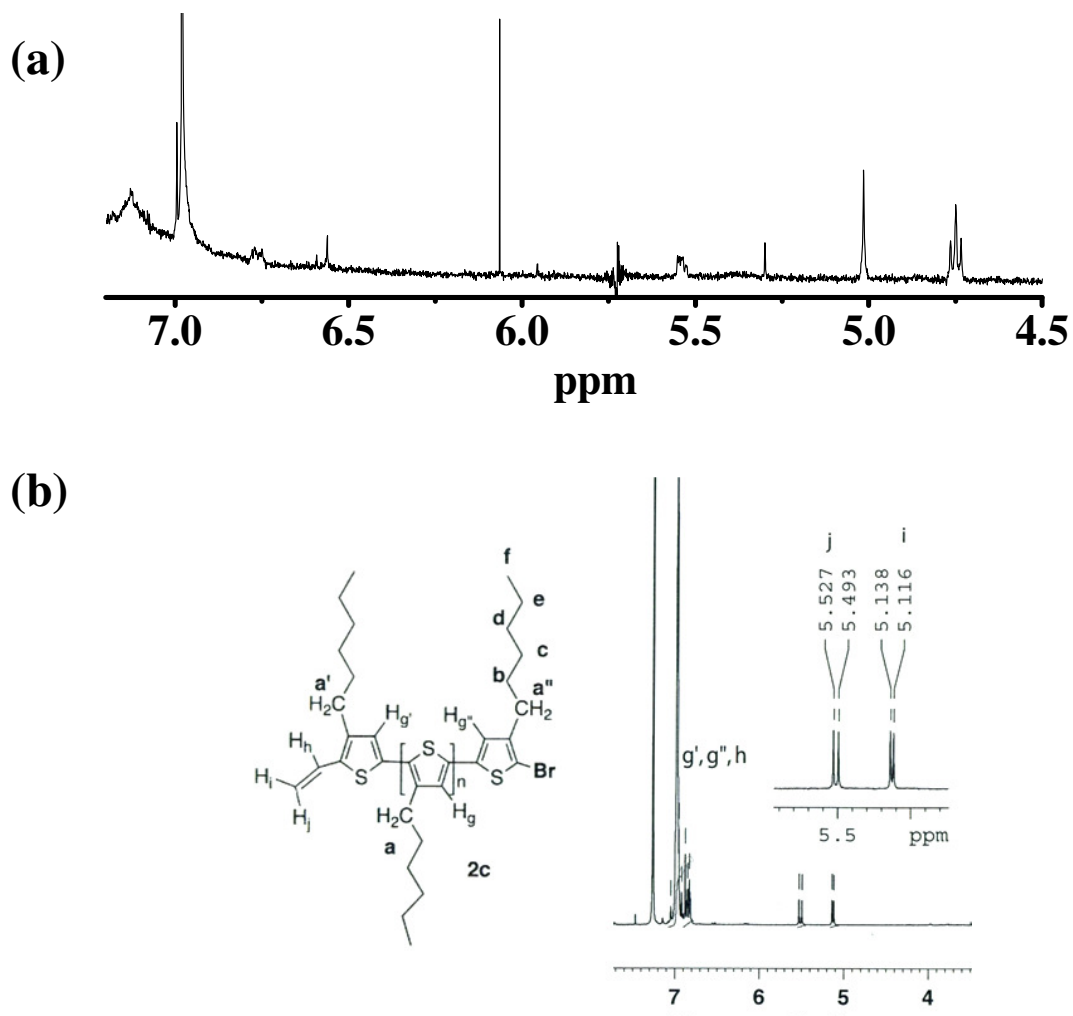
Supporting Information

(a)

(b)

Figure 5-6. ^{1}H-NMR spectra of (a) P3HT–CdSe nanocomposites and (b) P3HT homopolymer. The proton signals from the end-vinyl group at 5.1 and 5.5 ppm disappeared after P3HT was grafted onto CdSe QDs.
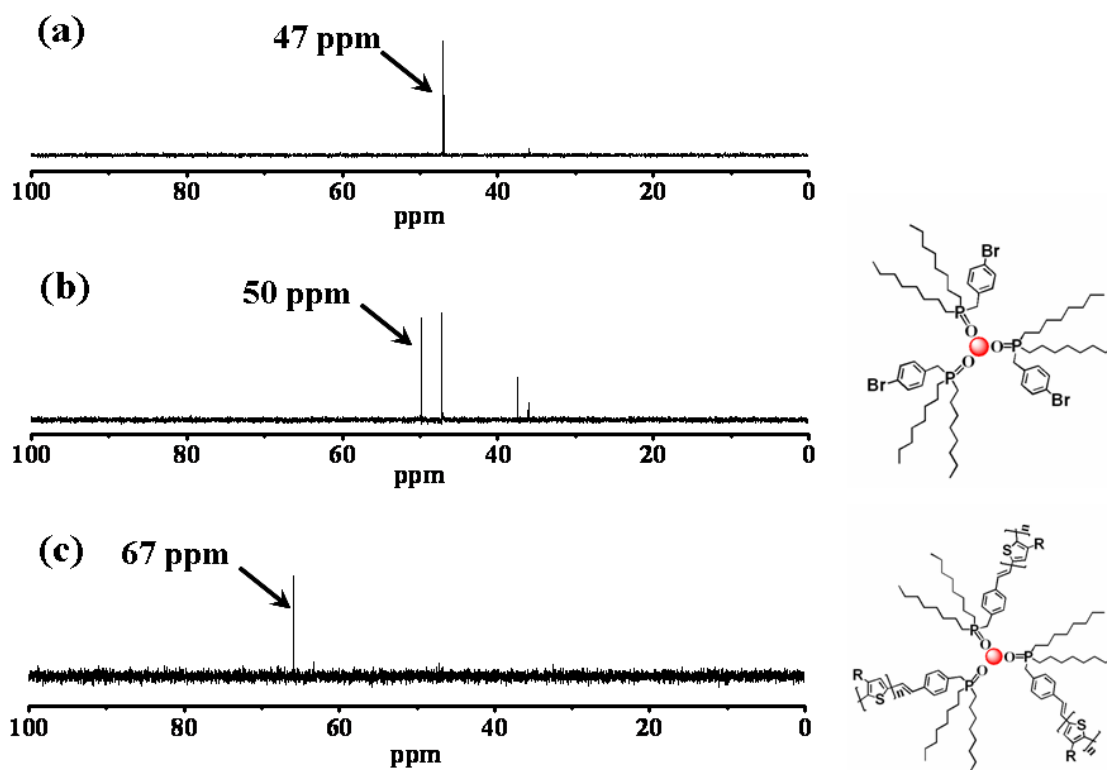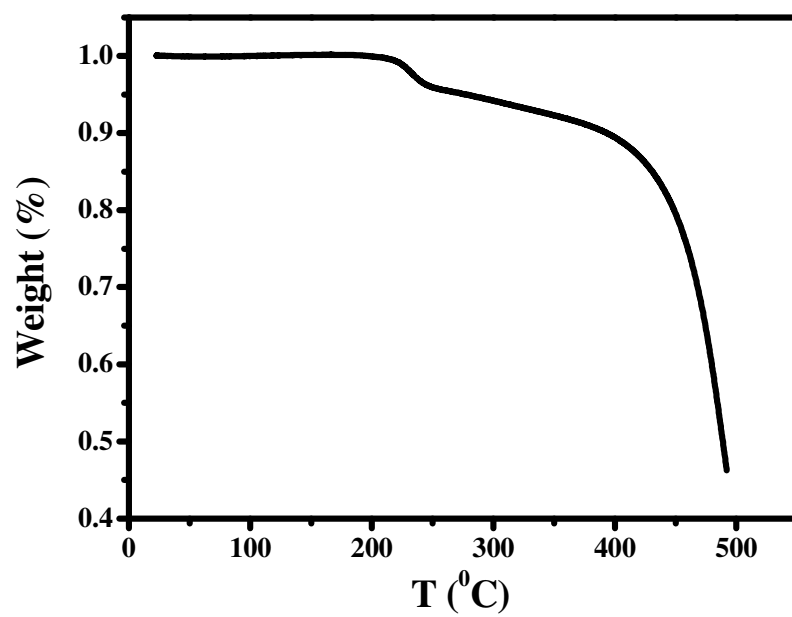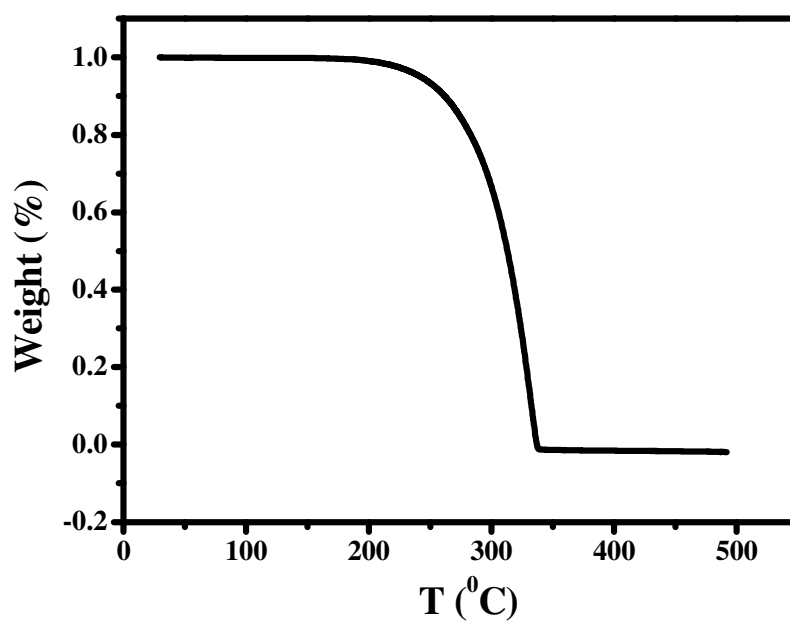
Figure 5-7. ^{31}P-NMR spectra of (a) [(4-bromophenyl)methyl]dicotylphosphine oxide (DOPO-Br), (b) DOPO-Br functionalized CdSe QDs, and (c) CdSe grafted with P3HT via Heck coupling (i.e., P3HT−CdSe nanocomposites).
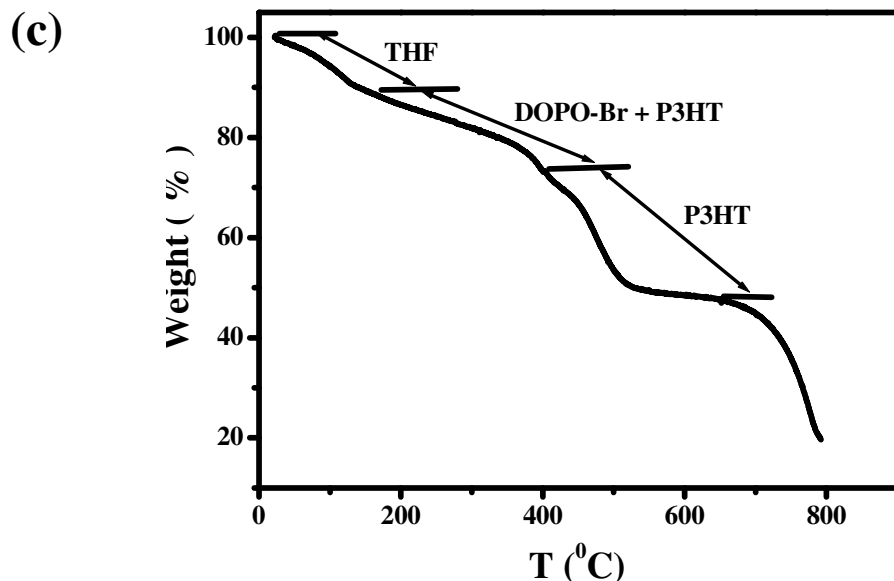
(a)

(b)

Figure 5-8. Thermogravimetry analysis (TGA) of (a) vinyl-terminated P3HT, (b) DOPO-Br, and (c) nanocomposite of CdSe−P3HT prepared by grafting vinyl terminated P3HT onto (DOPO-Br)-functionalized CdSe. In details, the weight loss from P3HT between 400°C and 600 °C is 21%. According to TGA of pure P3HT, 90% of P3HT is lost between 400°C and 600 °C, with the remaining 10% P3HT being lost between 200°C and 400 °C, which is same to the literature report. Therefore, the total weight loss of P3HT in the nanocomposites between 200°C and 600 °C is 21% ÷ 90% = 23.3%, with 2.3% of it being lost between 200°C and 400 °C along with the loss of DOPO-Br. The residue weight above 600 °C is CdSe, which is 49 %. The molecular weight of P3HT is 2404 and the molecular weight of CdSe QD is 113,000. Therefore, the mole ratio between P3HT and CdSe is (23.3% ÷ 2404) : (49% ÷ 113000) ≈ 22 : 1.

References

1.   Schwartz, B. J., Conjugated polymers as molecular materials: How chain conformation and film morphology influence energy transfer and interchain interactions. *Annual Review of Physical Chemistry* **54**, 141 (2003).

2.   Lin, Y.-H.; Jiang, C.; Xu, J.; Lin, Z. Q.; Tsukruk, V. V., Robust, fluorescent, and nanoscale freestanding conjugated films. *Soft Matter* **3**, 432 (2007).

3.   Lin, Y.-H.; Jiang, C. Y.; Xu, J.; Lin, Z. Q.; Tsukruk, V. V., Sculptured layer-by-layer films. *Adv. Mater.*, (accepted).

4.   Jeffries-EL, M.; Sauve, G.; McCullough, R. D., In-situ end-group functionalization of regioregular poly(3-alkylthiophene) using the Grignard metathesis polymerization method. *Advanced Mateerials.* **16**, 107 (2004).

5.   Jeffries-El, M.; Sauve, G.; McCullough, R. D., Facile synthesis of end-functionalized regioregular poly(3-alkylthiophene)s via modified Grignard metathesis reaction. *Macromolecules* **38**, 10346 (2005).

6.   Iovu, M. C.; Jeffries-EL, M.; Sheina, E. E.; Cooper, J. R.; McCullough, R. D., Regioregular poly(3-alkylthiophene) conducting block copolymers *Polymer* **46**, 8582 (2005).

7.   Coakley, K. M.; Liu, Y. X.; McGehee, M. D.; Findell, K. L.; Stucky, G. D., Infiltrating semiconducting polymers into self-assembled mesoporous titania films for photovoltaic applications. *Advanced Funcitional. Materials* **13**, 301 (2003).

8.   Alivisatos, A. P., Semiconductor clusters, nanocrystals, and quantum dots. *Science* **271**, 933 (1996).

9.   Xu, J.; Xia, J. F.; Wang, J.; Shinar, J.; Lin, Z. Q., Quantum dots confined in nanoporous alumina membranes. *Applied. Physics Letters.* **89**, 133110 (2006).

10.   Xu, J.; Xia, J.; Lin, Z. Q., Evaporation-induced self-assembly of nanoparticles from a sphere-on-flat geometry. *Angewandt Chemie, Internaitonal. Edition* **46**, 1860 (2007).

11.   Zimnitsky, D.; Jiang, C.; Xu, J.; Lin, Z. Q.; Tsukruk, V. V., Substrate- and timedependent photoluminescence of auantum dots inside the ultrathin polymer LbL film. *Langmuir* **23**, 4509 (2007).

12. Peng, X. G.; Wilson, T. E.; Alivisatos, A. P.; Schultz, P. G., Synthesis and isolation of a homodimer of cadmium selenide nanocrystals *Angewandt Chemie International. Edition.* **36**, 145 (1997).

13. Skaff, H.; Sill, K.; Emrick, T., Quantum dots tailored with poly(para-phenylene vinylene). *Journal of the American Chemical Society* **113**, 22 (2004).

14. Odoi, M. Y.; Hammer, N. I.; Sill, K.; Emrick, T.; Barnes, M. D., Observation of enhanced energy transfer in individual quantum dot-oligophenylene vinylene nanostructures. *Journal of the American Chemical Society* **128**, 3506 (2006).

15. Querner, C.; Reiss, P.; Bleuse, J.; Pron, A., Chelating ligands for nanocrystals' surface functionalization. *Journal of the American Chemical Society* **126**, 11574 (2004).

16. Kalyuzhny, G.; Murray, R. W., Ligand Effects on Optical Properties of CdSe Nanocrystals. *Journal of Physical Chemistry B* 109, 7012 (2005).

17. Komoto, A.; Maenosono, S.; Yamaguchi, Y., Oscillating fluorescence in an unstable colloidal dispersion of CdSe/ZnS core/shell quantum dots. *Langmuir* **20**, 8916 (2004).

18. Greenham, N. C.; Peng, X.; Alivisatos, A. P., Charge separation and transport in conjugated-polymer/semiconductor-nanocrystal composites studied by photoluminescence quenching and photoconductivity. *Physical Review B.* **54**, 17628 (1996).

19. Huynh, W. U.; Dittmer, J. J.; Alivisatos, A. P., Hybrid nanorod-polymer solar cells. *Science* **295**, 2425 (2002).

20. Milliron, D. J.; Alivisatos, A. P.; Pitois, C.; Edder, C.; Frechet, J. M. J., Electroactive surfactant designed to mediate electron transfer between CdSe nanocrystals and organic semiconductors. *Advanced Materials* **15**, 58 (2003).

21. Milliron, D. J.; Gur, I.; Alivisatos, A. P., Hybrid organic-nanocrystal solar cells *MRS Bulletin* **30**, 41 (2005).

22. Colvin, V. L.; Schlamp, M. C.; Alivisatos, A. P., Light-emitting diodes made from cadmium selenide nanocrystals and a semiconducting polymer. *Nature* **370**, 354 (1994).

23. Coe, S.; Woo, W. K.; Bawendi, M.; Bulovis, V., Electroluminescence from single monolayers of nanocrystals in molecular organic devices. *Nature* **420**, 800 (2002).

24. Lee, J.; Sundar, V. C.; Heine, J. R.; Bawendi, M. G.; Jensen, K. F., Full color emission from II-VI semiconductor quantum dot-polymer composite. *Advanced Materials* **12**, 1102 (2000).

25. Friend, R. H.; Denton, G. J.; Halls, J. J. M.; Harrison, N. T., *Solid State Communication* **102**, 249 (1997).

26. Bozano, L.; Carter, S. A.; Scott, J. C.; Malliaras, G. G.; Brock, P. J., *Applied Physics Letters* **74**, 1132 (1999).

27. Arango, A. C.; Johnson, L. R.; Bliznyuk, V. N.; Schlesinger, Z.; Carter, S. A.; Hörhold, H. H., Efficient titanium oxide/conjugated polymer photovoltaics for solar energy conversion. *Advanced Materials* **12**, 1689 (2000).

28. Huynh, W. U.; Dittmer, J. J.; Libby, W. C.; Whiting, G. L.; Alivisatos, A. P., Controlling the morphology of nanocrystal-polymer composites for solar cells. *Advanced Functional Materials* **13**, 73 (2003).

29. Liang, Z.; Dzienis, K. L.; Xu, J.; Wang, Q., Covalent layer-by-layer assembly of conjugated polymers and CdSe nanoparticles: multilayer structure and photovoltaic properties. *Advanced Functional Materials* **16**, 542 (2006).

30. Gur, I.; Fromer, N., A.; Chen, C.-P.; Kanaras, A. G.; Alivisatos, A. P., Hybrid solar cells with prescribed nanoscale morphologies based on hyperbranched semiconductor nanocrystals. *Nano Letters* **7**, 409 (2007).

31. Advincula, R. C., Hybrid organic/inorganic nanomaterials based on polythiophene dendronized nanoparticles. *Dalton Transactions* 2778 (2006).

32. Liu, J. S.; Tanaka, T.; Sivula, K.; Alivisatos, A. P.; Frechet, J. M. J., Employing end-functional polythiophene to control the morphology of nanocrystal-polymer composites in hybrid solar cells. *Journal of the American Chemical Society* **126**, 6550 (2004).

33. Iraqi, A.; Barker, G. W., Synthesis and characterisation of telechelic regioregular head-to-tail poly(3-alkylthiophenes). *Journal of Materials Chemistry* **8**, 25 (1998).

34. Liu, J.; McCullough, R. D., End group modification of regioregular polythiophene through postpolymerization functionalization. *Macromolecules* **35**, 9882 (2002).

35.   Sheina, E. E.; Liu, J.; Iovu, M. C.; Laird, D. W.; McCullough, R. D., Chain growth mechanism for regioregular nickel-initiated cross-coupling polymerizations. *Macromolecules* **37**, 3526 (2004).

36.   Daniel, M. C.; Astruc, D., Gold nanoparticles: Assembly, supramolecular chemistry, quantum-size-related properties, and applications toward biology, catalysis, and nanotechnology. *Chemical Review* **104**, 293 (2004).

37.   Zubarev, E. R.; Xu, J.; Sayyad, A.; Gibson, J. D., Amphiphilicity-driven organization of nanoparticles into discrete assemblies. *Journal of the American Chemical Socieity* **128**, 15098 (2006).

38.   Holdcroft, S., A photochemical study of poly(3-hexylthiophene). *Macromolecules* **24**, 4834 (1991).

39.   Perepichka, I. F.; Perepichka, D. F.; Meng, H.; Wudl, F., Light-emitting polythiophenes. *Advanced Materials* **17**, 2281 (2005).

40.   Spano, F. C., Modeling disorder in polymer aggregates: the optical spectroscopy of regioregular poly(3-hexylthiophene) thin films. *Journal of Chemical Physic* **122**, 234705 (2005).

41.   Huynh, W. U.; Dittmer, J. J.; Teclemariam, N.; Milliron, D. J.; Alivisatos, A. P., Charge transport in hybrid nanorod-polymer composite photovoltaic cells. *Physical Review B.* **67**, 115326 (2003).

42.   Kim, Y.; Cook, S.; Tuladhar, S. M.; Choulis, S. A.; Nelson, J.; Durrant, J. R.; Bradley, D. D. C.; Giles, M.; Mcculloch, I.; Ha, C. S.; Ree, M., A strong regioregularity effect in self-organizing conjugated polymer films and high-efficiency polythiophene:fullerene solar cells. *Nature Materials* **5**, 197 (2006).

43.   Kuno, M.; Lee, J. K.; Dabbousi, B. O.; Mikulec, F. V.; Bawendi, M. G., The band edge luminescence of surface modified CdSe nanocrystallites: probing the luminescing state. *Journal of Chemical Physics* **106**, 9869 (1997).

44.   Wang, Y.; Teng, X.; Wang, J.; Yang, H., Solvent-free atom transfer radical polymerization in the synthesis of Fe2O3@polystyrene core-shell nanoparticles. *Nano Letters* **3**, 789 (2003).

45.   Leatherdale, C. A.; Bawendi, M. G., Observation of solvatochromism in CdSe colloidal quantum dots. *Physical Reivew B* **63**, 165315 (2001).

46. Sykora, M.; Petruska, M. A.; Alstrum-Acevedo, J.; Bezel, I.; Meyer, T. J.; Klimov, V. I., Photoinduced charge transfer between CdSe nanocrystal quantum dots and Ru-polypyridine complexes. *Journal of the American Chemical Soceity* **128**, 9984 (2006).

47. Chasteen, S. V.; Carter, S. A.; Rumbles, G., Exciton dynamics and device performance in polythiophene heterojunctions for photovoltaics. *Proc. of SPIE* **5938**, 59380J-1 (2005).

48. Hammer, N. I.; Early, K. T.; Sill, K.; Odoi, M. Y.; Emrick, T.; Barnes, M. D., Coverage-mediated suppression of blinking in solid state quantum dot conjugated organic composite nanostructures. *Journal of Physical Chemistry B* **110**, 14167 (2006).

49. Headley, L. S.; Mukherjee, P.; Anderson, J. L.; Ding, R.; Halder, M.; Armstrong, D. W.; Song, X.; Petrich, J. W., *Journal of Physical Chemistry A* **110**, 9549 (2006).

50. Chowdhury, P. K.; Halder, M.; Sanders, L.; Calhoun, T.; Anderson, J.; Armstrong, D. W.; Song, X.; Petrich, J. W., *Journal of Physical Chemistry B* **108**, 10245 (2004).

51. van Herrikhuyzen, J.; George, S. J.; Vos, M. R. J.; Sommerdijk, N. A. J. M.; Ajayaghosh, A.; Meskers, S. C. J.; Schenning, A. P. H. J., Self-assembled hybrid oligo(p-phenylenevinylene)–gold nanoparticle tapes. *Angewandt Chemie. International Edition* **46**, 1857 (2007).

52. Sun, B.; Snaith, H. J.; Dhoot, A. S.; Westenhoff, S.; Greenham, N. C., Vertically segregated hybrid blends for photovoltaic devices with improved efficiency. *Journal of Applied Physics* **97**, 014914 (2005).

53. Kang, Y. M.; Park, N. G.; Kinm, D. W., Hybrid solar cells with vertically aligned CdTe nanorods and a conjugated polymer. *Appllied Physics Letters* **86**, 113101 (2005).

CHAPTER 6. GENERAL CONCLUSIONS

Gradient concentric ring patterns of high regularity form spontaneously simply by allowing a droplet of solution containing either conjugated polymer or semiconductor nanocrystal in a consecutive stick-slip mothion in a confined geometry. Solution concentrations and solvents properties exert profound effect on λ_{C-C} and h_d. A simple theoretical calculation based on mass conservation has been performed to reveal the nature of the formation of gradient ring patterns. The studies demonstrate that dynamic self-assembly in a confined geometry may offer a new means to produce *gradient* features, as well as a simple, versatile, generalizable approach to produce yet more complex patterns. Furthermore, spokes of nanocrystals form as a result of fingering instabilities of an evaporating front, thereby expanding the versitility of the pattern-forming process. Such constrained evaporation can be utilized as a simple, cheap, and robust strategy for self-assembling various materials with easily tailored optical and electronic properties into spatially ordered, two-dimensional patterns. These self-organized patterns of functional nanoscale materials over large areas offer a tremendous potential for applications in optoelectronic devices, LEDs, solar cells, and biosensors.

Spherical nanocrystals (i.e. CdSe/ZnS core/shell QDs) were placed in a hexagonal array of highly ordered cylindrical nanopores of PAMs by a simple dip-coating method and vacuum suction process, respectively. The fluorescence of CdSe/ZnS QD was retained after being filled inside PAMs and the filling contents were obtained via transmission UV-vis measurements.

A relatively long chain CP, vinyl-terminated highly regioregular P3HT (14 thiophene units) was chemically tethered to the [(4-bromophenyl)methyl]dicotylphosphine oxide (DOPO-Br)-functionalized CdSe QD surface via a mild palladium-catalyzed Heck coupling (i.e., a "grafting onto" route to P3HT–CdSe nanocomposites; there is no need for ligand

exchange chemistry). The success of the coupling was confirmed by the ^{1}H-NMR and ^{31}P-NMR spectroscopies. The number of P3HT bound to each CdSe QD was estimated by TGA. The photophysical properties of nanocomposites were found to differ from the conventional composites in which P3HT and CdSe QDs were physically mixed. Solid-state emission spectra of nanocomposites suggested the charge transfer from P3HT to 3.5-nm CdSe QDs, while the energy transfer from 3.5-nm CdSe QD to P3HT was implicated in the P3HT/CdSe composites. A faster decay in lifetime further confirmed the occurrence of charge transfer in the nanocomposites.

ACKNOLDEGMENT